Spatially resolved spectroscopy across HD 189733A using exoplanet transits

Martin Gustavsson

Lund Observatory
Lund University

2017-EXA117

Degree project of 60 higher education credits (for a degree of Master)
May 2017

Supervisor: Dainis Dravins

Lund Observatory
Box 43
SE-221 00 Lund
Sweden

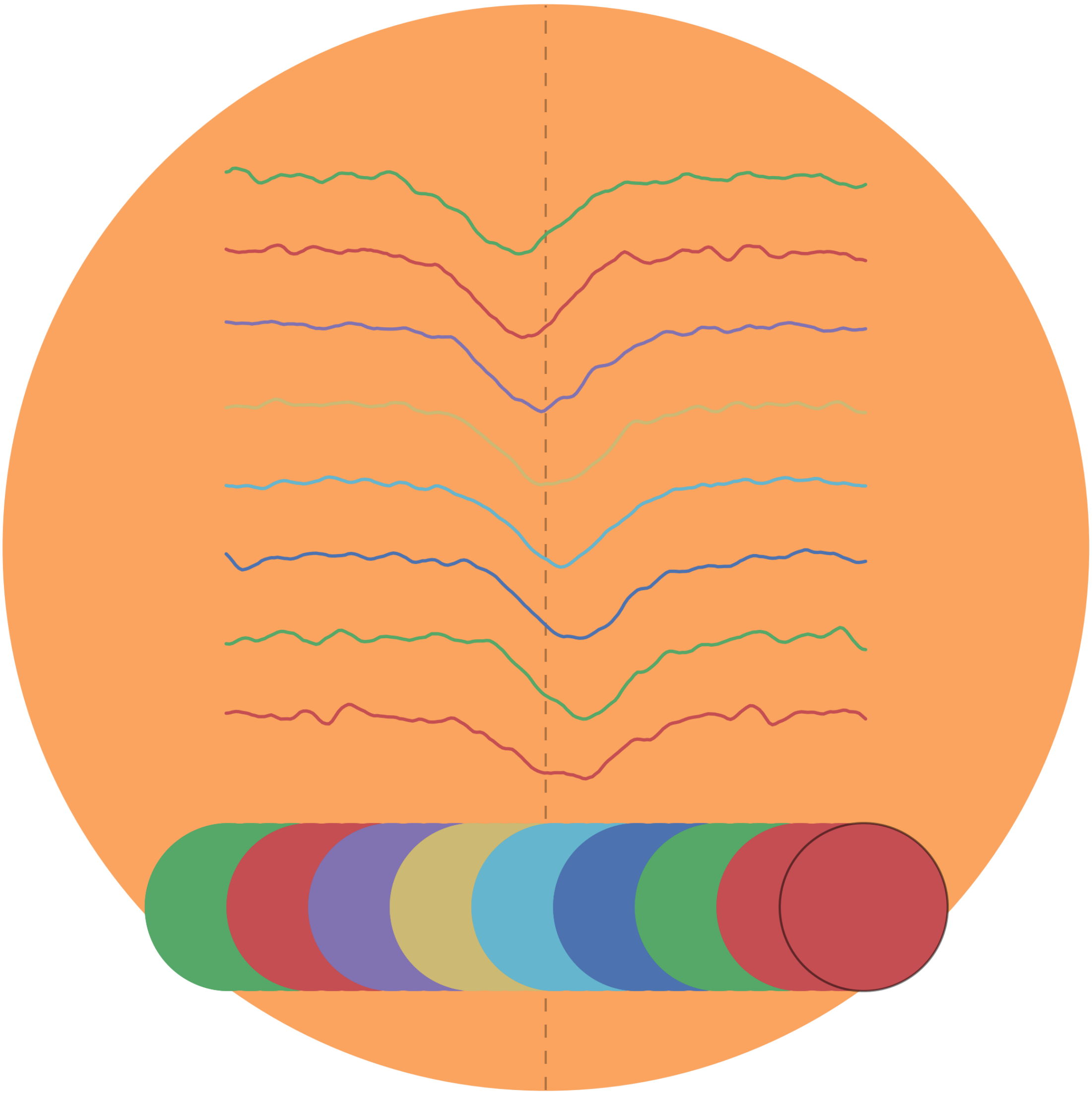

Abstract

For testing three-dimensional (3D) hydrodynamic models of stellar atmospheres, spectroscopy across spatially resolved stellar surfaces with high spectral resolution is desired. 3D models predict center-to-limb changes in asymmetries, shapes, strengths and wavelength positions of spectral line profiles, reflecting the hydrodynamics of the stellar atmosphere. However, except for a few supergiants and the Sun, current telescopes are not yet capable of resolving in detail any stellar surface. It is instead possible to exploit transiting exoplanets as probes of the atmospheres of their host stars. The spectra of the stellar surface portions covered by the planet during transit can be obtained by subtracting in-transit spectra from the stellar spectrum outside transit. Transiting planets typically cover only a small percentage of the stellar surface, requiring exceedingly high signal-to-noise ratios of the original spectra, obtainable by averaging numerous similar photospheric spectral lines. We apply this method to the $m_V = 7.7$ mag, K1 V star HD 189733A (‘*Alopex*’); its transiting planet covers ~ 2.5 % of the surface of its host star and is the deepest known transit among the brighter systems. Archival data from the ESO HARPS spectrometer are used to reconstruct spatially resolved representative profiles of photospheric Fe I lines, with the aim of comparing these to analogous synthetic line profiles computed from a 3D hydrodynamic model.

Acknowledgements

Thank you, Dainis, for your supervision and support—academic and personal—and for providing the opportunity to work at the frontiers of astronomy.

Till mamma och pappa

Populärvetenskaplig beskrivning

När vi blickar upp mot natthimlen (och om vi har tur) ser vi stjärnor. Några förefaller stora och ljusstarka, andra små och ljussvaga. Dock ser vi dem bara som ljusa punkter, även när vi tittar genom stora teleskop. Vi kan alltså inte direkt urskilja ytorna på dessa avlägsna solar och tvingas utröna deras egenskaper från det samlade stjärnljuset. Undantaget är vår egen stjärna, solen, vars yta är lätt att observera och vars egenskaper därför kunnat undersökas i detalj.

Vi vet att solens yttre atmosfär sjuder av aktivitet från gaser som genom värmerörelser skiktas i storskaliga hastighetsmönster som bildar grynliknande geometriska strukturer, s.k. granuler. En typisk granul är ca 1 000 km i utsträckning. Kring dess mitt stiger heta gaser uppåt för att sedan sjunka ner i omringande, mörkare fåror. Vi kan mäta hur snabbt dessa gaser rör sig eftersom de genom Dopplereffekten förskjuter våglängderna av det ljus som de utsänder.

I en stjärnas spektrum – det som erhålls när man med t.ex. ett prisma delat upp ljuset i olika våglängder – återfinns s.k. absorptionslinjer. Dessa uppstår därför att olika grundämnen i stjärnatmosfären absorberar vid vissa våglängder som är unika för varje ämne. Dessa våglängder är samma som vi kan mäta på jorden, och möjliggör därför bl.a. igenkännandet av grundämnena i solen och i andra stjärnor.

Vi kan se effekter från värmerörelser i solatmosfären i form av vissa förändringar i absorptionslinjernas utseende och liknande effekter måste finnas i andra stjärnor. Om man inte kan uttolka dessa, kan det leda till systematiska fel i bestämningen av t.ex. stjärnornas kemiska sammansättning och även försvåra letandet efter planeter kring dessa. För en god förståelse krävs tredimensionella modeller av stjärnatmosfärer, som ur fysikens lagar kan beräkna den komplicerade växelverkan mellan gas och strålning som sker i en stjärnatmosfär. Riktigheten av dessa datormodeller är dock vansklig att kontrollera för andra stjärnor än solen, eftersom man ju inte kan urskilja deras ytor.

I detta projekt utnyttjas passagen av en planet över en stjärna för att ge information om strukturerna på stjärnans yta. Skillnaden mellan stjärnans spektrum då planeten skymmer en viss liten del av den, och det som observeras då planeten inte längre är framför stjärnan, ger information om den del av stjärnan som tillfälligt skymdes av planeten. Eftersom planeten är mycket mindre än stjärnan, blir effekten liten och metoden kräver därför mycket precisa observationer. Dessa blir mindre krävande om man väljer en ljusstark stjärna med en stor planet. Endast ett fåtal sådana system har hittills upptäckts och denna metod har tidigare bara kunnat tillämpas på en annan, solliknande, stjärna.

Metoden tillämpas här på en stjärna som är något mindre och svalare än solen. Stjärnans katalognummer är HD 189733A men vi kallar den *Alopex* (grekiska för räv), eftersom den befinner sig i stjärnbilden Räven. Målsättningen är att identifiera effekter från värmerörelser i stjärnans atmosfär, för att sedan testa tredimensionella datormodeller för just denna stjärntyp.

Contents

1 Introduction 1

1.1 Stellar atmospheres 1
  1.1.1 The resolved solar surface 1
1.2 Precision stellar spectroscopy 3
  1.2.1 1D models of stellar atmospheres 3
  1.2.2 Hydrodynamic models of stellar atmospheres 4
1.3 Resolving stellar surfaces 8
1.4 Exoplanet transits and the Rossiter-McLaughlin effect 9
1.5 Exoplanet transits as probes of stellar atmospheres 10
  1.5.1 HD 189733A (Alopex) 11
1.6 Project overview 12

2 Spatially resolved spectroscopy across HD 189733A 13

2.1 The observations 13
  2.1.1 The HARPS data 14
2.2 Data analysis 15
  2.2.1 Line identification 16
  2.2.2 Astrocentric correction 20
  2.2.3 Line center determination and averaging of lines 21
  2.2.4 Forming collated transit epochs 23
2.3 Line profile ratios during transit 24
  2.3.1 Line profile ratios of the representative profile from 158 Fe I lines 27
2.4 The Rossiter-McLaughlin effect 29
2.5 Reconstructing spatially resolved line profiles 31
  2.5.1 Reconstructing spatially resolved representative profiles from 158 Fe I lines 34
2.6 Effects from varying the line selection 39
  2.6.1 ‘Strictly unblended’ lines 39
  2.6.2 Representative ‘strong’ and ‘weak’ line profiles 45

3 Summary and conclusions 51

Appendix A Atlas of the Alopex spectrum 55

Appendix B ‘Cool Stars 19’ conference poster 83

1

Introduction

> *LECTURER: "Fundamentally, a star is a pretty simple structure..."*
> *VOICE FROM THE AUDIENCE: "You would look pretty simple,*
> *too, at a distance of ten parsecs."*
> — In Arthur Beer*, Vistas in Astronomy,* 1954

1.1 Stellar atmospheres

The stellar atmosphere is the outermost region of a star, which in cool main-sequence stars[1], is situated above the stellar core, radiative and convective zones. In the core of these stars, energy is being released by fusion of hydrogen to helium. This thermonuclear energy is transported outward by radiation in the radiative zone and then mainly by convection in the convective zone (spanning about 30 $\%$ of the stellar radius) until it reaches the atmosphere, where it is again transported outwards by radiation. The atmosphere is in turn divided up into the photosphere, chromosphere and corona according to their average kinetic temperature, as seen in Figure 1.1. The visible light that we see from stars originate from the photosphere, which for the Sun on the order of 100 km thick.

1.1.1 The resolved solar surface

The Sun displays a range of features on its surface, such as granulation patterns that emerge from the respective rising and falling of the hotter and cooler plasma in its atmosphere, and magnetic flux tubes that give rise to cold spots that we see as the darker sunspots. These features vary on timescales from minutes to decades, which have taken many detailed measurements over long time periods[2] to deduce, much helped by the fact that the surface features of the Sun are readily resolved.

---

[1] F-, G- and K-type dwarf stars with effective temperatures below $T_{\text{eff}} \sim 7\,000$ K.

[2] Possibly the longest running experiment in history is that of counting the number of spots on the Sun, which has been on-going since the time of Galileo (Galilei et al., 1613) and has revealed the 11-year

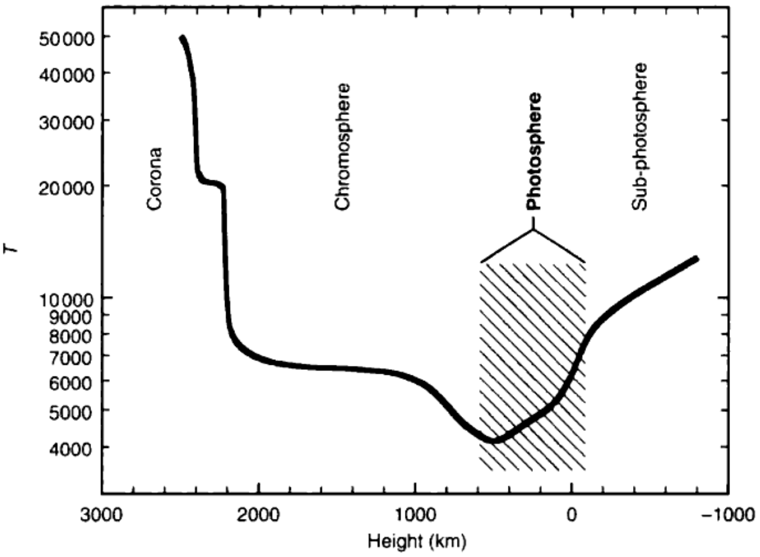

Figure 1.1: A model of the temperature distribution of the solar atmosphere. The temperature at the top of the photosphere is 4 400 K and at the bottom 6 600 K; its effective temperature is 5 772 K. The photosphere is the region where all visible light comes from. Figure from Gray (2008).

A number of phenomena can be observed on the resolved solar surface. Such a phenomenon is the gradual diminishing of brightness towards the limb of the Sun; this 'limb-darkening' is due to one unit of optical depth[3] penetrating the deepest into the photosphere at disk center, where the line of sight is perpendicular to the surface, exposing to the observer hotter and thus brighter layers, gradually penetrating less deep as the viewing angle from the center increases. In general, recording a spectrum at some resolved surface segment of the Sun produces absorption line profiles subject to the distribution of gas velocities at that particular segment. These velocities produce Doppler shifts, leading to broadening, skewing and shifting of line profiles. One readily observed outcome from these velocity fields is the solar 'limb effect' (Hunter, 1934), where spectral lines are displaced shortward when seen at disk center and less so when viewed towards the limb; this is the convective blueshift due to vertically and predominately upward moving hot gas, pronounced fully at disk center and less so at the limbs, where the vertical motions are directed perpendicular to the line of sight.

These phenomena are naturally extended to exist also on stellar surfaces. However, due to the point source nature of stars, we have not yet seen similar stellar surface features in any detail, but have instead been limited to deducing their properties from integrated starlight. Being able to precisely resolve stellar surfaces would enable the detailed study of stellar atmospheres of stars different from the Sun for the first time.

---

sunspot cycle we now know is related to solar magnetic activity.

[3] One unit of optical depth is defined as the distance over which the flux of some monochromatic light is diminished by $1/e$ due to absorption.

1.2 Precision stellar spectroscopy

The determination of fundamental stellar parameters such as effective temperature (T_{eff}), surface gravity ($\log g$) and chemical abundance (e.g., [Fe/H][4]) can be done using stellar spectroscopy, i.e., the study of light emanating from the atmospheres of stars as a function of wavelength (or frequency). Spectroscopy is arguably the most powerful tool available in deducing information not only about stars, but any astronomical object that emits or absorbs photons, and has had a profound impact on many fields ranging from stellar astrophysics to cosmology. However, stellar spectroscopy is an indirect method in that it relies upon modeling of the stellar atmosphere to determine the stellar parameters.

For stellar spectroscopy to reach higher precisions likely requires the transition from one-dimensional (1D) models of stellar atmospheres to more realistic three-dimensional (3D), hydrodynamic ones. Besides permitting a more accurate understanding and precise determination of the parameters of stars as such, absolute and precise values of abundances enable, e.g., chemical tagging of stars to locate common origins, or seeing chemical signatures in the atmospheres of host stars of otherwise undetected exoplanets. A highly accurate understanding of stellar atmospheres is also required for detecting chemical signatures in exoplanet atmospheres, as the only currently feasible way of measuring the constituents of the latter is against the segments of the stellar spectrum where the two atmospheres overlap.

1.2.1 1D models of stellar atmospheres

A common procedure when determining stellar parameters using spectroscopy is employing 1D, plane-parallel or spherically symmetric, hydrostatic models of stellar atmospheres, often assuming local thermodynamic equilibrium (LTE)[5]. Stellar properties are determined by optimizing to the observed spectrum a synthetic one obtained from the model. Although good as a first approximation, 1D models lack any realistic treatment of the hydrodynamics in the stellar atmosphere. Convection is typically treated only by an *a priori* unknown, free parameter (e.g., the ‘mixing-length’ parameter, α_{MLT}), which has to be observationally calibrated and can require different values for different observables in even the same star (e.g., Freytag et al., 2012). Furthermore, to account for the line broadening caused by convective flows, 1D models often use *ad hoc* and symmetric line broadening parameters, which historically were conjectured to represent convective micro- and macroturbulence[6] in the atmosphere. However, the movements of the convective flows are now understood to be laminar on the relevant spatial scales (e.g., Nordlund et al., 1997) and produce asymmetric line profiles (e.g., Dravins, 2008).

---

[4] The abundance, or ‘metallicity’, is given in square brackets to denote the $\log_{10}$-scale used, where a change in one order of magnitude corresponds to one ‘dex’ change in metallicity. The scale derives from the difference to the Sun in the ratio of the number density of iron to hydrogen, $\left[\text{Fe/H}\right] = \log_{10}\left(N_{\text{Fe}}/N_{\text{H}}\right)_{\star} - \log_{10}\left(N_{\text{Fe}}/N_{\text{H}}\right)_{\odot}$. Ratios using different elements are also used.

[5] The assumption of LTE means that the level populations of the absorbing species in the atmosphere are due only to collisional excitation. A ‘departure from’ LTE, or NLTE, occurs as the radiative-to-collisional excitation ratio becomes greater, which can sometimes severely affect the formation of absorption lines. Although NLTE is the norm in the atmosphere of a star (Asplund, 2005), and any model making claims of accuracy therefore needs to include it, the reason LTE still reigns supreme is because in NLTE the level population of each species needs to be treated individually, which substantially increases the computational cost. However, the most significant NLTE effect is seen for ionized species and in atmospheres where the radiative-to-collisional excitation ratios are large; the effects are therefore greater in O and B stars than in cooler stars (Gray, 2008). Besides, the systematic errors resulting from the assumption of LTE can be corrected for by later accounting for NLTE. We do not discuss the effects of NLTE further.

Calibrations to more realistic, 3D hydrodynamic models suggest that 1D models inevitably produce systematic uncertainties in the deduced stellar parameters by spectroscopic methods, typically larger than the measurement uncertainties (Asplund et al., 2000). 1D models of stellar atmospheres do work well where high precision and absolute values of any parameter is not of highest priority. In such differential measurements, systematic errors largely cancel out, e.g., when discerning large scale abundance gradients in the Milky Way. However, in any more precise analysis of stellar parameters and abundances, down to 0.01 dex, say, more realistic 3D, hydrodynamic models are most likely required.

Inversion vs. forward modeling

On an epistemological note, the application of 1D models to spectra of stars assumes that the problem is *invertible* (e.g., Allende Prieto et al., 2001); i.e., that the observed quantities can be directly inverted to reveal the physical cause(s). The appearence of a spectral absorption line is subject to a long and complex chain of events in its journey from the stellar atmosphere to the detector. The light has been scattered, absorbed and re-emitted inside a dynamically boiling and rotating mass of inhomogeneous gas, further smeared out by the fact that we must integrate the received flux over time. The nature of astronomical observations therefore dictates that the process of optimizing the model parameters of a synthetic spectrum to an observed one inevitably produces many equally likely parameter combinations with no one, unique solution. Thus, in practice, the problem is not invertible. To overcome this rather abysmal situation, however, the precise determination of stellar parameters can be approached by the reverse strategy of *forward modeling*; i.e., comparing the observables to a grid of pre-computed models from, in this case, realistic, *ab initio*, 3D hydrodynamic simulations.

1.2.2 Hydrodynamic models of stellar atmospheres

The degree of realism in 3D hydrodynamic models of stellar atmospheres is obviously higher than in their 1D counterpart. However, the computational requirements of the former are demanding and calculations for just one star can take months on a supercomputer[7]. Although the data for other stars are lacking, 3D models have been shown to agree well with observations of the resolved solar surface; apart from predicting the hydrodynamic effects mentioned in §1.1.1, solar photospheric abundances have been determined with high accuracy[8] using 3D models (Asplund et al., 2009) and these are now used as standard tabulated abundances of the Sun. Further, the timescale, topology and statistics of modeled solar granular patterns show strong agreement with observations (Stein & Nordlund, 1998), and the asymmetry and shifts of solar photospheric line profiles agree well with model predictions (Asplund et al., 2000).

---

[6] Supposed turbulence of scale smaller than one optical depth is typically what is called microturbulence, and that of larger scale macroturbulence.

[7] A non-trivial reason for the enduring success of 1D models is that they are practicable to run even on a mid-range personal computer.

To make the simulations of 3D hydrodynamic models tractable, numerous physical, mathematical and computational approximations are necessary. For cool stars, a common approach is to simulate a ‘box-in-a-star’, where only a small volume segment of some ten granules is computed as representative of the full stellar surface (e.g., Asplund, 2014). This approach has obvious limitations in that it cannot simulate phenomena larger than the size of its ‘box’, such as supergranulation or global oscillations.

3D models can now be computed for many different stellar types, ranging from white dwarfs to supergiants, and grids of 3D hydrodynamic models with a wide range of stellar parameters are available (e.g., Tremblay et al., 2013; Magic et al., 2013). As such, we presently find ourselves in a somewhat peculiar situation, wherein detailed models of many types of stars can be computed, but their observational confrontation is almost non-existent. Before they can start to be employed en masse by the astronomical community, the validity of 3D hydrodynamic model simulations and the approximations that go into them need some way to be tested observationally.

Predictions from 3D hydrodynamic models

For individual photospheric absorption lines, 3D hydrodynamic models predict shifting, skewing and broadening of their line profiles depending on where they originate on the stellar disk. These effects reflect the temperature structure and convective velocities of the gas flows in the stellar atmosphere.

---

[8] As verified by ground measurements of the abundances in CI chondrites. CI chondrites purportedly originate from the most pristine meteoroids in the Solar System. As such, they are thought to have the same abundances of the non-volatile elements, such as Fe and Mg, as the solar photosphere.

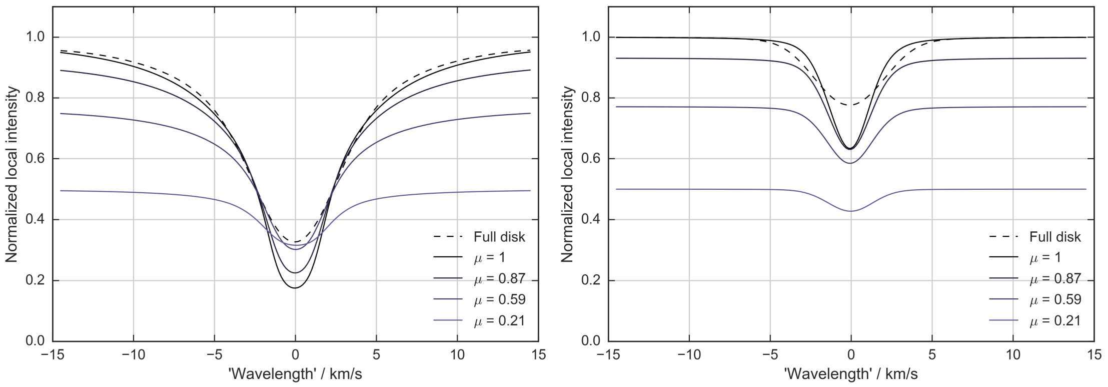

Figure 1.2: Simulated 'strong' (left) and 'weak' (right) photospheric ($\lambda = 6\ 200$ Å) Fe I absorption lines obtained as temporal and spatial averages across small segments of the disk of a $T_{\text{eff}} = 3\ 960$ K ('K8 V') star with low rotational velocity ($v \sin i = 3$ km/s). The synthetic profiles are for different $\mu = \cos\theta$, where θ is the angle between the normal to the stellar surface and the line of sight, $\mu = 1$ being disk center and $\mu = 0.21$ close to the limb. Simulation data from Dravins et al., (*in preparation*).

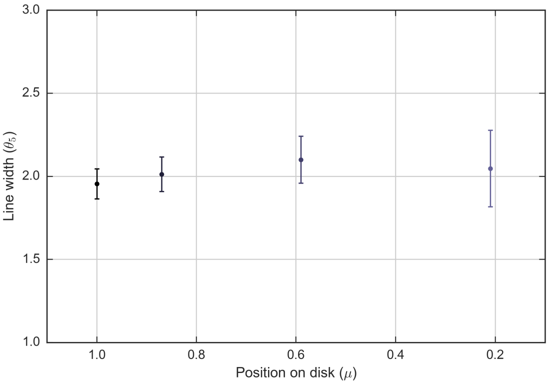

Figure 1.3: The widths of the 'weak' line profiles from the CO^{5}BOLD 3D hydrodynamic simulation shown in Figure 1.2 against position on the disk (where μ =1 is disk center). The widths are determined by fitting a Gaussian (Equation (2.4)) to the line profiles, with the uncertainties being the formal one standard deviation. Towards the limb, the line profile increasingly deviates from a Gaussian shape, reflected by the increased uncertainties.

Example predictions from a 3D hydrodynamic model, the CO^{5}BOLD model (Freytag et al., 2010), are shown in Figure 1.2[9]. Temporally and spatially averaged synthetic profiles—simulating an exoplanet transit across the equator—are computed for four different center-to-limb positions (solid curves) together with one integrated, full-disk profile (dashed curve). The spatially resolved profiles are in general narrower and deeper as they are not subject to rotational broadening. Further, the profiles broaden as they move towards the limb of the disk, reflecting that horizontal convective velocities have a larger amplitude than vertical ones. This discrepancy in velocity amplitudes is caused by the fact that the vertical height of the photosphere is smaller than the horizontal extent of granules, and follows from the conservation of mass: as the upward-flowing gas in the granule reaches the top of the photosphere, it starts moving sideways through a smaller surface area, forcing an increase of its velocity[10] (e.g., Nordlund et al., 2009). An estimate of the size of this effect is shown in Figure 1.3.

---

[9] In Figure 1.2, and throughout this thesis, we plot the line profiles on a Doppler velocity scale, which is a natural scale when measuring radial velocity effects in, e.g., stellar atmospheres. The scale for a wavelength range λ is calculated by $\lambda_{\text{Doppler}} = c\frac{\lambda-\lambda_0}{\lambda_0}$ where c is the speed of light and λ_0 a reference wavelength setting the 0-point, or rest-frame.

Taking the ratio of line profiles from different disk positions to the profile of the integrated full-disk reveals the minuscule wavelength shifts due mainly to stellar rotation, thus it shows the same anomalous radial velocity as in the Rossiter-McLaughlin effect (§1.4). Figure 1.4 shows the effect of the same simulated transiting planet as above, as it passes the stellar equator on a prograde orbit, i.e., in the same direction as the stellar rotation. These ratios are sensitive to asymmetries in the line profiles, seen as slightly different curves on the ingress and egress sides of the transit. This diminutive effect is not discernible in Figure 1.4.

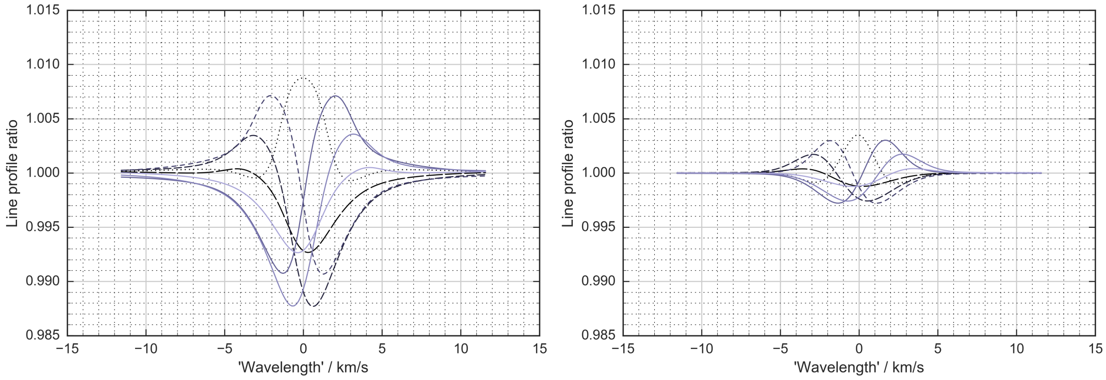

Figure 1.4: Line profile ratios between spatially resolved absorption lines and the full-disk profile at different disk positions, simulating a transit by a planet passing over the stellar disk. Curves from ingress are successively shorter-dashed until dotted at disk center and curves from disk center to egress are successively lighter in color. The amplitude is on the order of 0.5 $\%$ for the 'strong' (left) spectral line, and about half of that for the 'weak' one (right). Simulation data from Dravins et al., (*in preparation*).

Testing of 3D hydrodynamic models against different stars can to some extent be done using integrated starlight; e.g., from the radial velocity or photometric flickering of the flux, or even astrometric displacement of the photocenter, as the number of granules on the surface vary with time. However, integrated starlight by its very nature contains information obscured by several layers of degeneracy and likely cannot provide any detailed diagnostics compared to that available from spatially resolved stellar surfaces. Similarly as for the Sun, the center-to-limb hydrodynamic effects constitute an excellent testbed for 3D hydrodynamic models, but they clearly require spatially resolved stellar surfaces. Thus, detailed testing and falsification of these models will likely come only as we are able to resolve stars.

---

[10] To see this behavior, consider a fluid with mass m passing through a volume V, i.e., with density $\rho = m/V$. The surface area A_1 on the side of the volume through which the fluid is passing with velocity v_1 is subjected to the mass flow rate $\dot{m} = v_1 A_1 \rho$. If the fluid flows with the same rate $\dot{m}$ to an equally large volume with the same density, but passes through a smaller surface area A_2, it acquires the velocity v_2. Mass conservation dictates that $v_1 A_1 = v_2 A_2$ and since $A_1 > A_2$ it follows that $v_1 < v_2$.

1.3 Resolving stellar surfaces

Already the next generation of optical telescopes hold promise in resolving distant stellar surfaces. However, this endeavor requires not only immense ‘eyes’ in the form of extremely large telescopes, but also ways of overcoming the seeing imposed by the Earth’s atmosphere. Atmospheric seeing is on the order of 0.5 arcseconds (as) under the best conditions. The most straightforward (but perhaps most difficult) way to circumvent the atmosphere is to put the telescope in space, but techniques such as active and adaptive optics might enable us to reach the diffraction limited resolution[11] also on the ground.

The diffraction limited resolution of the current largest ground telescopes with 10 m apertures is about 10 mas. Most nearby stellar disks are on the order of 1 mas in angular diameter. However, some giants have angular diameters of order 100 mas; e.g., Betelgeuse extends 125 mas in the UV and have been imaged by the Hubble Space Telescope (HST; Uitenbroek et al., 1998). To date, tens of stellar disks have been resolved, including main sequence stars such as Altair (3.2 mas; Monnier et al., 2007) and Alpha Centauri A and B (8.3 and 5.8 mas, respectively; Kervella et al., 2003); these, however, using interferometric techniques. The next generation of mirror telescopes, e.g., the 39 m Extremely Large Telescope (ELT) with a diffraction limited resolution of about 3.5 mas, slated to come online in the next 10 years, will surely enable more detailed studies of resolved stellar surfaces.

In the meantime, as we shall see, a new avenue for studying stellar surfaces is opening up, namely by using transiting exoplanets as probes of their host stars. The resolution achievable by this technique is then determined by the angular size of the transiting exoplanet[12] and not the size of the telescope per se, although a larger collection area would certainly improve another limiting factor, namely the signal-to-noise ratio (S/N). The viability of this technique is determined by the properties of the planetary system, as further elaborated on in §1.5.1.

---

[11] Diffraction limited resolution is defined as

$$\theta = 1.22 \cdot \frac{\lambda}{D} \cdot 206265 \text{ as},$$

where λ is the wavelength of the light ($\lambda \approx 5\,000$ Å for optical light) and D the aperture of the telescope.

[12] A ‘transiting’ binary star could in principle also be used, but the surface area of the ‘host star’ covered by the occulting star is relatively large, which reduces the achievable resolution. What is more, both stars likely emit significantly overlapping spectra and it is not necessarily a simple task to disentangle them.

1.4 Exoplanet transits and the Rossiter-McLaughlin effect

In the fortuitous case that the inclination of the orbit of an exoplanet around its host star closely aligns with the line of sight, the passage of the planet across the stellar surface can be seen. This temporary obscuration of the starlight forms a dip in any recorded time-series of the photometric brightness of the star during the transit event, obtaining a characteristic ‘transit light curve,’ see Figure 1.5. From this light curve, a number of orbital parameters are accessible through, e.g., a Keplerian optimization scheme. In particular, the radius of the planet $\mathrm{R_p}$, its orbital inclination i and impact parameter b are obtained.

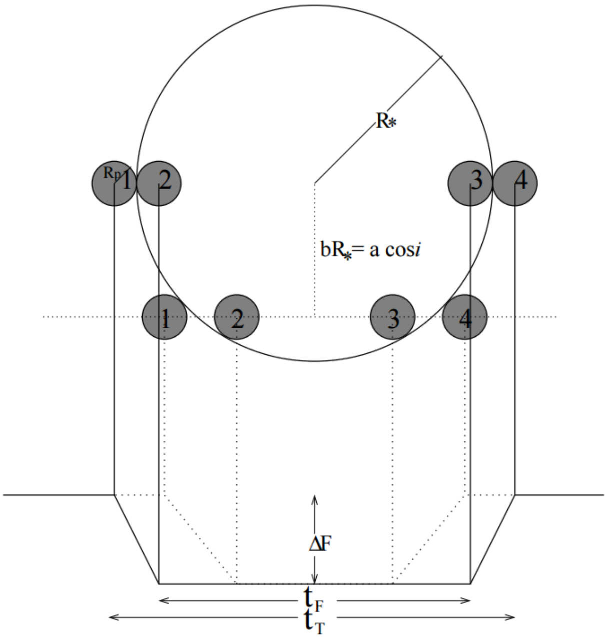

Figure 1.5: The transit light curves obtained for the two different transit geometries shown on top. The maximum obscuration of the stellar flux is marked ΔF and obtained for a period t_{F} between ingress and egress. The total transit time is t_{T}. The impact parameter b is the distance from the stellar disk center at conjunction, given as a fraction of the host star radius $\mathrm{R}_\star$. Different b or i result in different light curves. Figure from Seager & Mallén-Ornelas (2003).

If spectroscopic radial velocity measurements are taken during a transit event, additional information about the star and planet can be retrieved. The anomalous radial velocity shift of the integrated stellar spectrum seen during transit, or the Rossiter-McLaughlin (RM) effect, is such a measurement. The ‘anomaly’ comes from the fact that as the planet transits, it covers first the radial velocity contribution from one hemisphere and then, if it passes the rotational axis of the star, the other. If the star rotates such that the first hemisphere is moving towards the observer, the flux contributing to the radial velocity blueshift is diminished, leading to an increased redshift of the stellar spectrum. Conversely, as it passes over to the second hemisphere, a blueshift of the spectrum is obtained. The end result is an RM waveform such as those seen in Figure 1.6. The RM effect provides an independent measure of the stellar rotational velocity $v \sin i$, as well as the obliquity, or spin-orbit alignment, λ. Further, the direction of the orbit relative to the stellar rotational axis can be determined. The motion is called ‘prograde’ if their directions are the same and ‘retrograde’ if they are contrary.

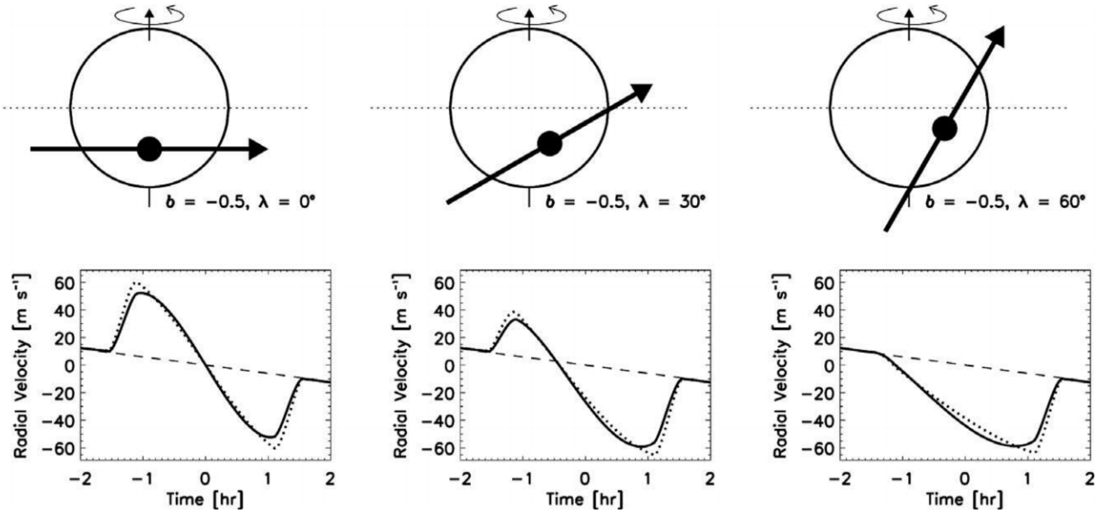

Figure 1.6: Three instances of the anomalous radial velocity shift, or Rossiter-McLaughlin (RM) effect, during transit with constant impact parameter $b = 0.5$ and three different spin-orbit obliquities, $\lambda = 0$, 30 and 60°. The RM waveforms are shown with limb-darkening (solid lines) and without (dotted lines); the dashed lines mark the barycentric orbit of the host star induced by the planet (cf., Figure 2.6). Figure from Winn (2011).

1.5 Exoplanet transits as probes of stellar atmospheres

Resolved stellar surfaces are clearly out of reach for current telescopes. However, transiting exoplanets can be exploited as probes that precisely reveal small surface segments of the stellar atmosphere as it crosses its host star. By subtracting the stellar spectrum observed during transit from that outside transit, the spectrum behind the planet is revealed. This technique can be used to resolve distant stellar atmospheres of differing types and thus has the potential to provide sharp diagnostic tools for testing 3D hydrodynamic models.

Although the method is simple in principle, it is hard in practice. Transiting exoplanets cover only about 1 $\%$ of the surfaces of F-, G- and K-type dwarf stars[13], and while the small area covered by the planet means that equally small stellar surface features can be probed, the same small percentage of the original stellar signal is all that remains after subtraction. To get a signal-to-noise ratio (S/N) of 100 of the spatially resolved surface segment, therefore, an original S/N of 10 000 is required.

---

[13] M-type dwarf stars can have planets that cover up to 10 $\%$ of the stellar disk, but are typically faint and therefore not likely targets for this method.

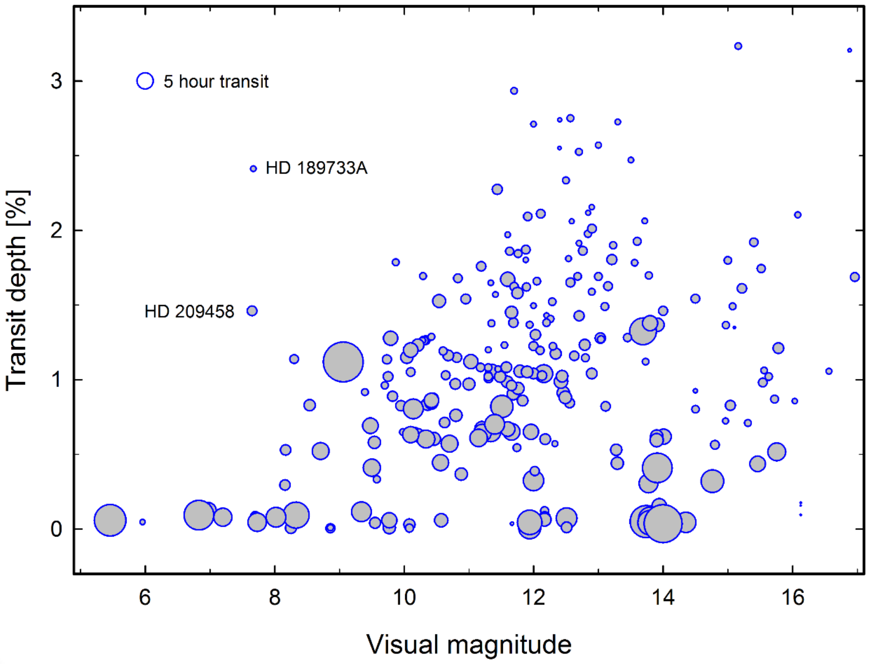

Figure 1.7: The photometric transit depth for transiting exoplanets in relation to their host star apparent visual magnitude m_V. The sizes of the circles are proportional to the transit duration. The systems HD 209458 and HD 189733A have bright host stars with deep transits and form the main candidates for spatially resolving stellar surfaces using exoplanet transits. Figure from Dravins et al. (2017).

1.5.1 HD 189733A (Alopex)

To optimally increase the S/N of the resolved stellar surface segment, bright host stars with large transiting planets are favored. To locate a target system for this method, we plot the known transiting exoplanet systems with their brightness and transit depth. In Figure 1.7, two of the more optimal systems meeting the demand for a bright host star with a large transiting planet are the $m_V \sim 7.7$ mag HD 209458 and HD 189733A[14]. Both are hosts to transiting 'Hot Jupiters': gas giants with puffed up atmospheres orbiting close to the host star. The G-dwarf star HD 209458 is transited by a planet with maximum photometric transit depth of around 1.5 %; it has been the subject of study using the same method as here (Dravins et al., 2017), much helped by its similarity to the Sun. The cooler K-dwarf star HD 189733A hosts a planet covering a maximum of about 2.5 % of the stellar surface. Hence, we select the HD 189733A system as the subject of our study, as it not only has the deepest transit among the brighter systems, but comprises an opportunity to study a stellar atmosphere of a star of different stellar type than the Sun. Henceforth, HD 189733A is referred to as Alopex[15].

---

[14] HD 189733A is the primary of a double star system, accompanied by an M-dwarf, HD 189733B, with a semi-major axis of 216 AU (Bakos et al., 2006).

[15] Alopex (gr. 'ἀλώπηξ') is an original taxonomic name for the arctic fox given by Linnaeus (1758), here relating to the namesake of its constellation *Vulpecula* (lat. 'little fox').

Besides its large apparent brightness and deep transit, there are numerous other advantages to studying Alopex. The planet Alopex b has since its discovery (Bouchy et al., 2005) been studied intensely using high-grade facilities and a lot of the data have been made freely available in online archives. The system remains an object of interest for, e.g., exoplanet atmospheric studies and is likely to be observed with future telescopes. One further advantage of Alopex is that it is comparable in effective temperature to the K-giant Arcturus (see Table 1.1), a well-studied benchmark star, which facilitates the identification of the chemical species of its spectral lines. Moreover, the availability of unblended lines is crucial for achieving the high S/N required by this method, and since the rotational velocity of Alopex, $v \sin i \sim 2.3$ km/s (Torres et al., 2012), is relatively low, the number of blended lines is minimized.

Table 1.1: Parameters of select stars pertinent to this study. HD 209458 shares many parameters with the Sun which enables straightforward line identifications. Likewise, Alopex is similar to Arcturus leading to an analogous advantage.

	Spectral type	T_{eff} / K	$\log g$ / cm/s^2	[Fe/H]
Sun	G2 V	5770	4.4	0
HD 209458	G0 V	6071 ± 20^a	4.38^a	0^a
Alopex	K1 V	4875 ± 43^b	4.53 ± 0.14^c	-0.03 ± 0.08^c
Arcturus	K0 III	4286 ± 30^d	1.66 ± 0.05^d	-0.52 ± 0.04^d

---

[a] del Burgo & Allende Prieto (2016)

[b] Boyajian et al. (2015)

[c] Torres et al. (2008)

[d] Ramírez & Allende Prieto (2011)

1.6 Project overview

The work in this thesis is prompted by the following: a) as discussed above, 3D hydrodynamic models predict the temporally and spatially averaged behavior of single photospheric spectral lines, such as broadening, shifting and skewing of the line profile, that vary across the stellar disk; b) 3D models have not been extensively tested against stars significantly different from the Sun; and c) given sufficiently high spectral resolution and S/N, the behavior of single photospheric spectral lines across stellar disks can be accessed by the means of a transiting planet, in principle resolving the stellar surface behind the planet.

The method of spatially resolved spectroscopy using exoplanet transits is feasible already with current state-of-the-art spectroscopes and has been applied to the transiting exoplanet system with the bright, solar-like (G0 V spectral type) host star HD 209458 using UVES on the VLT (Dravins et al., 2016; Dravins et al., 2017). This work applies the same method to a transiting exoplanet system with a similarly bright host star of a different spectral type, HD 189733A (Alopex) with a K1 V host star, using the HARPS spectrometer on the ESO 3.6 m telescope.

2

Spatially resolved spectroscopy across HD 189733A

In this chapter, we describe in detail the method used to spatially resolve the surface of HD 189733A (Alopex) using spectroscopy during exoplanet transits. We explained the choice of Alopex as the target of this study in §1.5.1. Below, we describe the choice of data and its acquisition (§2.1); the main analysis of the data along with a presentation of the results (§2.2–2.5); and the effects of varying some of the line selection parameters (§2.6).

2.1 The observations

To locate observational data suitable to our purposes, we set up a number of criteria for the desired data quality. We require the observations to have a S/N of around 100 or more for individual exposures and, in order to discern details of individual line profiles, a resolution of the spectrograph of order 100 000. Additionally, in order to be able to combine different observations taken at different times using the same telescope, a spectrograph with good wavelength stability is required. Further, to confine the study to the stellar photosphere we limit the wavelength region to the visual[1].

These criteria leave a number of candidate spectrometers: High Resolution Echelle Spectrometer (HIRES) and High Dispersion Spectrograph (HDS) on the 10 m Keck and 8.2 m Subaru telescopes, respectively, on Maunakea, Hawaii; Ultraviolet and Visual Echelle Spectrograph (UVES) on the 8.2 VLT on Cerro Paranal, Chile; High Resolution Spectrograph (HRS) on the 9.2 m Hobby-Eberly Telescope (HET) at the McDonald Observatory, Texas, USA; and HARPS on the ESO 3.6 m telescope at La Silla Observatory, Chile.

The archives of these instruments were searched for reduced data from observations of

---

[1] This choice also has two benefits worth mentioning; it minimizes the overlap of line profiles ('blending') and the contamination by absorption lines in the atmosphere of the Earth ('telluric lines'). The infrared region of the spectrum suffers from substantial absorption by water molecules in the atmosphere. The ultraviolet region of stellar spectra is typically rich in lines leading to significant blending, and also suffers from absorption by predominately atmospheric molecular oxygen and ozone. While there are potentially some small windows in these regions that could be exploited to probe, e.g., the stellar chromosphere, these prospects are not pursued in this study.

Alopex during a transit of Alopex b. Only the archives of UVES and HARPS yielded such data. To minimize eventual complications from handling and combining data from two different instruments, two observing runs from HARPS were finally selected for the analysis. Having at least two observing runs enable not only the combination of data, but also checking the results of the analysis against each other.

2.1.1 The HARPS data

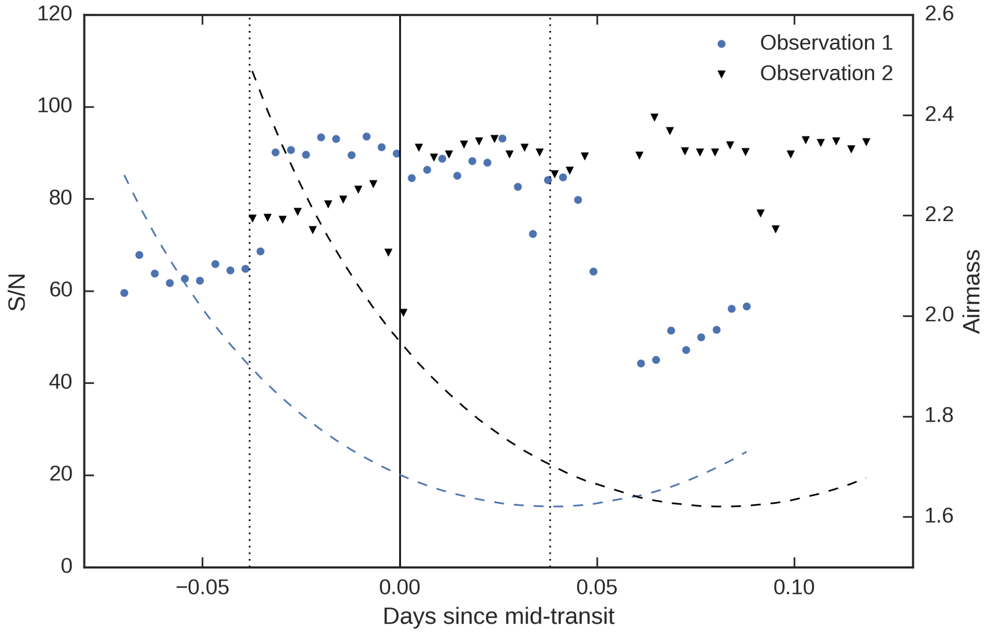

Figure 2.1: The two HARPS observing runs. The scattered points show for both observing runs the S/N of the exposures as given by the data reduction pipeline. The dashed curves show the airmass during the observing runs. The gaps are here removed exposures of the brighter star HD 190590 ($V = 6.5$) presumably used for calibration purposes.

HARPS is a high resolution ($\frac{\Delta\lambda}{\lambda} = 115\,000$) spectrograph designed for precise radial velocity detections of exoplanets; as such, it has excellent wavelength stability, enabling detection of stellar barycentric radial velocities of order 1 m/s. The light collected by the 3.6 m telescope is fiber-fed to an echelle spectrograph spanning 3 800–6 900 Å over 72 echelle orders and projected onto two charge-coupled devices (CCDs); their physical separation gives a slight gap in the center of the spectrum as seen in Figure 2.2. The nominal S/N for a 71 s exposure on an $m_V = 3.5$ mag star with an airmass of 1.1 ranges between 100 and 400 depending on the wavelength region, with higher S/N at longer wavelengths (Mayor et al., 2003).

The data used in the analysis come from two HARPS observing runs with ESO program IDs 079.C-0127(A) and 079.C-0828(A), recorded on 28 August 2007 and 19 July 2007, respectively (henceforth observation 1 and 2, respectively)[2]. Each observing run covers a different transit epoch with 20 exposures, each with 300 s exposure time, both in- and out-of-transit (observation 2 has 19 out-of-transit exposures), see Figure 2.1. Figure 2.2 shows the acquired reduced HARPS spectrum of Alopex averaged over all exposures from both observing runs with the median S/N over all exposures of each echelle order overplotted. As expected, the S/N follows the response of the CCDs and increases with wavelength.

---

[2] Data from both observing runs are available in the ESO Archive, `http://archive.eso.org/`.

The date of the start of each exposure is given by the header of the acquired FITS[3] file for that exposure. To calculate the time of mid-transit, we use

$$T_i^{\mathrm{mid}} = T_0 \pm E_i P \tag{2.1}$$

where $T_0 = 2453988.80336^{+0.000072}_{-0.000039}$ MJD is a reference mid-transit time, $P = 2.21857312^{+0.00000036}_{-0.00000076}$ d (Triaud et al., 2009) the orbital period of the planet and $E_i = 1, 2, 3, \ldots$ the transit event.

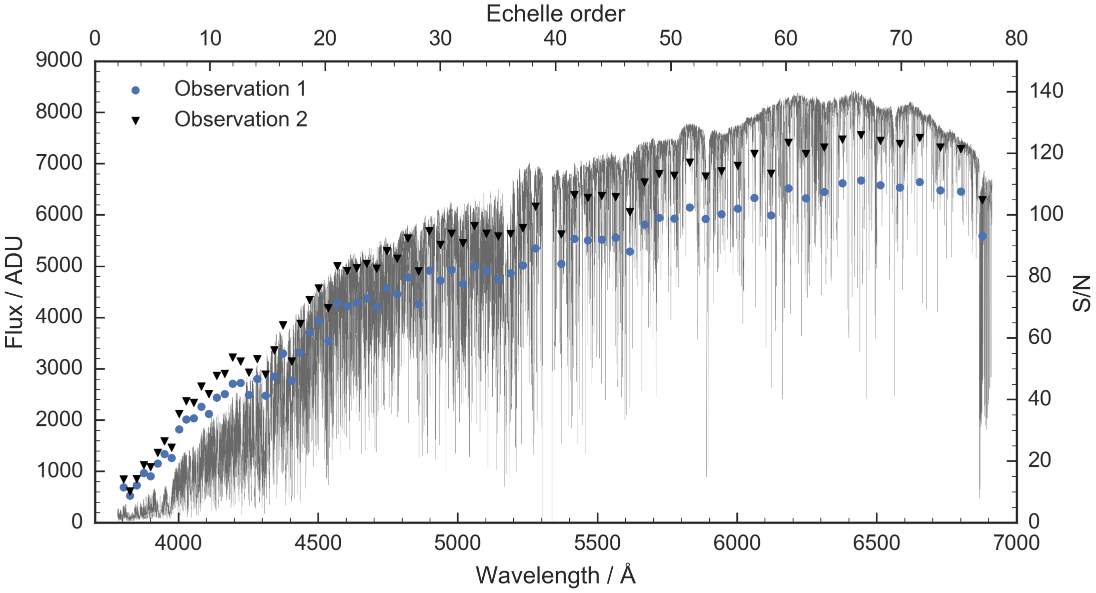

Figure 2.2: The markers show the median S/N for all exposures of the respective observing runs against wavelength and echelle order. The gray curve shows a typical raw HARPS spectrum of Alopex. The discontinuity around 5300 Å is the gap between the two CCDs. The S/N increases with wavelength and roughly follows the response of the CCDs and the blackbody-like flux curve of the star.

2.2 Data analysis

The analysis of the stellar spectrum from the small area covered by the transiting planet requires high S/N. To increase the S/N, averaging of many lines of the same chemical species can be done, as they exhibit similar behavior in the stellar atmosphere. To this end, we require a chemical species that is numerous, easy to identify and not in the atmosphere of Alopex b (or the Earth). The obvious choice is therefore Fe I[4], which exhibits a rich spectrum of lines and has been frequently measured and identified in other stars. Further, since the equilibrium temperature of Alopex b is calculated to be around 1 200 K (e.g., Arras & Bildsten, 2006), its atmosphere is not likely to have iron in absorption.

---

[3] The Flexible Image Transport System is a file format often used to store astronomical images and metadata. The metadata, such as the S/N of the exposure or the exposure time, are accessible in the human-readable ASCII header contained in every FITS file.

Assuming that the noise is random in nature, we estimate the S/N in the analyses that follow as

$$\mathrm{S/N} = \sqrt{n_{\mathrm{exp}}} \cdot \sqrt{n_{\mathrm{lines}}} \cdot \mathrm{S/N}_{\mathrm{nominal}} \tag{2.2}$$

where n_{exp} and n_{lines} are the respective number of exposures and lines, and $\mathrm{S/N}_{\mathrm{nominal}} \approx 80$ the median of the medians of the S/N of both observing runs as seen in Figure 2.1.

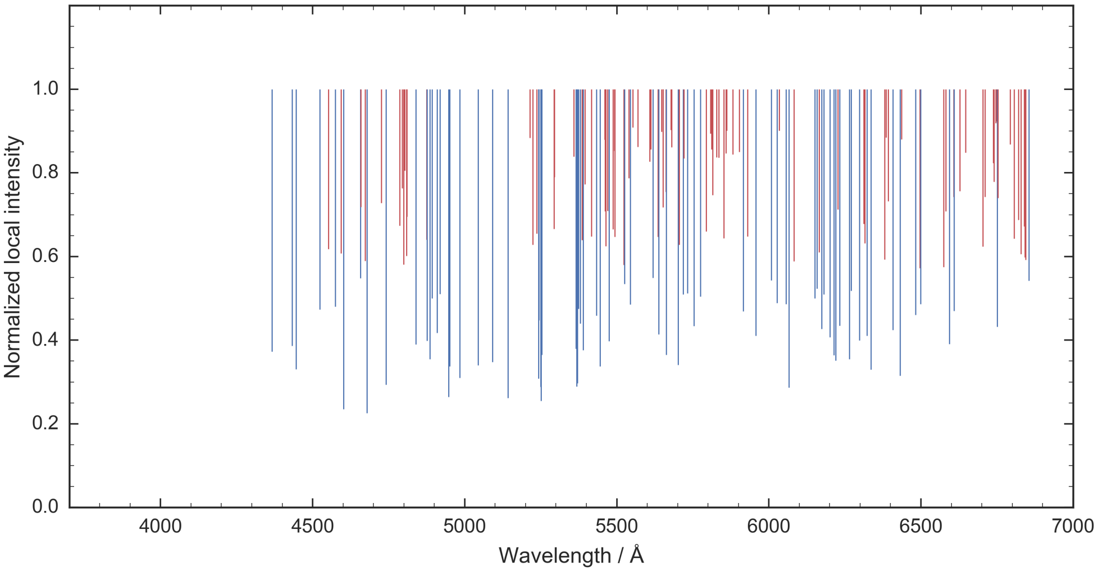

Figure 2.3: The distribution of the 158 Fe I lines in Figure 2.5 and Table 2.1. Locating unblended lines becomes increasingly difficult below wavelengths of 4 500 Å as the number of lines in the spectrum of Alopex increases substantially (see, e.g., the atlas in Appendix A). Lines with a central intensity value below and above 0.55 are marked in blue and red, respectively (the ‘strong’ and ‘weak’ lines in §2.6.2, respectively).

2.2.1 Line identification

Identifying the lines in the spectrum of Alopex is simplified by the fact that the metallicity of Alopex is not subtantially different from that of the Sun; as such, they are expected to have many spectral lines in common. Further, the metallicity and temperature of Alopex is similar to that of Arcturus, one of the few stars with extensive line identifications. Therefore, we can use as first approximation a list of unblended lines in the solar spectrum, available in the literature, and then check the found lines against the Arcturus spectrum to verify that they are not, e.g., contaminated by lines from other species or otherwise unusable. This approach is simple and has a sound empirical footing and is therefore favored to, e.g., using a synthetic spectrum from an atomic line database run through a stellar atmosphere model. An excerpt of the Alopex spectrum together with that of Arcturus is shown in Figure 2.4; an atlas over the same two spectra spanning the wavelength range of HARPS (3 800–6 900 Å) is available in Appendix A.

---

[4] The roman numeral marks the degree of ionization, where I is neutral, II singly ionized, et seq.

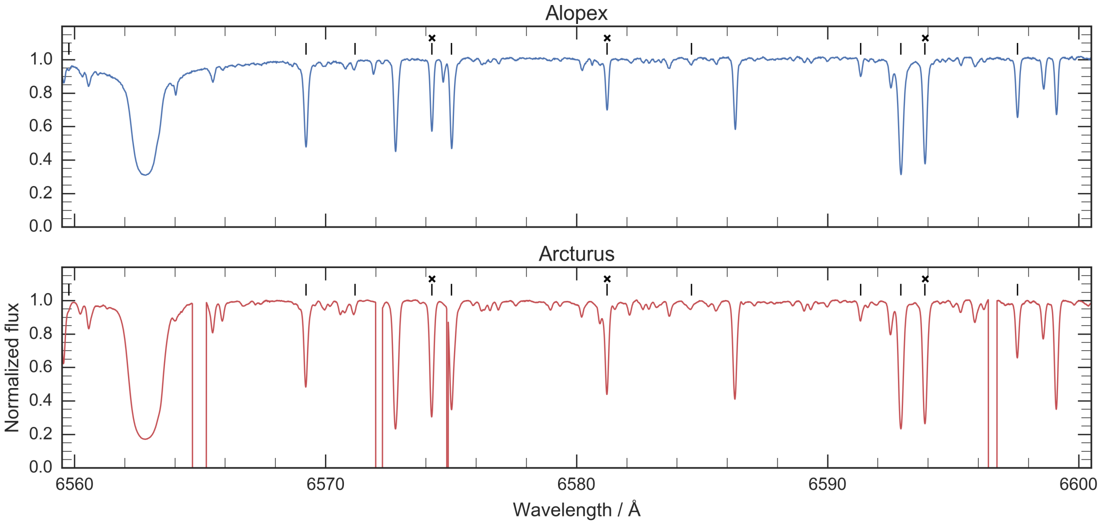

Figure 2.4: Comparison of the same parts of the Alopex and Arcturus spectra. The Arcturus spectrum is from Hinkle et al. (2000). The black lines mark Fe I lines identified in the Arcturus spectrum and black crosses mark the lines selected for this study (given in Table 2.1). Both spectra have a similar resolution of around 100 000. The discontinuities in the Arcturus spectrum are regions where the correction for telluric contamination has been inadequate and thus removed.

Fe I line list

We use a list of 402 unblended solar Fe I lines by Stenflo & Lindegren (1977) to identify prospective lines in the spectrum of Alopex. Of these solar lines, 158 are found to be reasonably unblended in the spectrum of Alopex. The data for the 158 lines are given in Table 2.1 and their distribution in wavelength is shown in Figure 2.3. Shown in Figure 2.5 is the select 158 Fe I lines and their grand average (arithmetic mean), forming a synthesized representative profile[5] with a central line intensity of 0.59 in units of the locally normalized continuum.

---

[5] 'Representative profile' is used to denote that the line profiles averaged in this way represent a Fe I line profile of a certain depth.

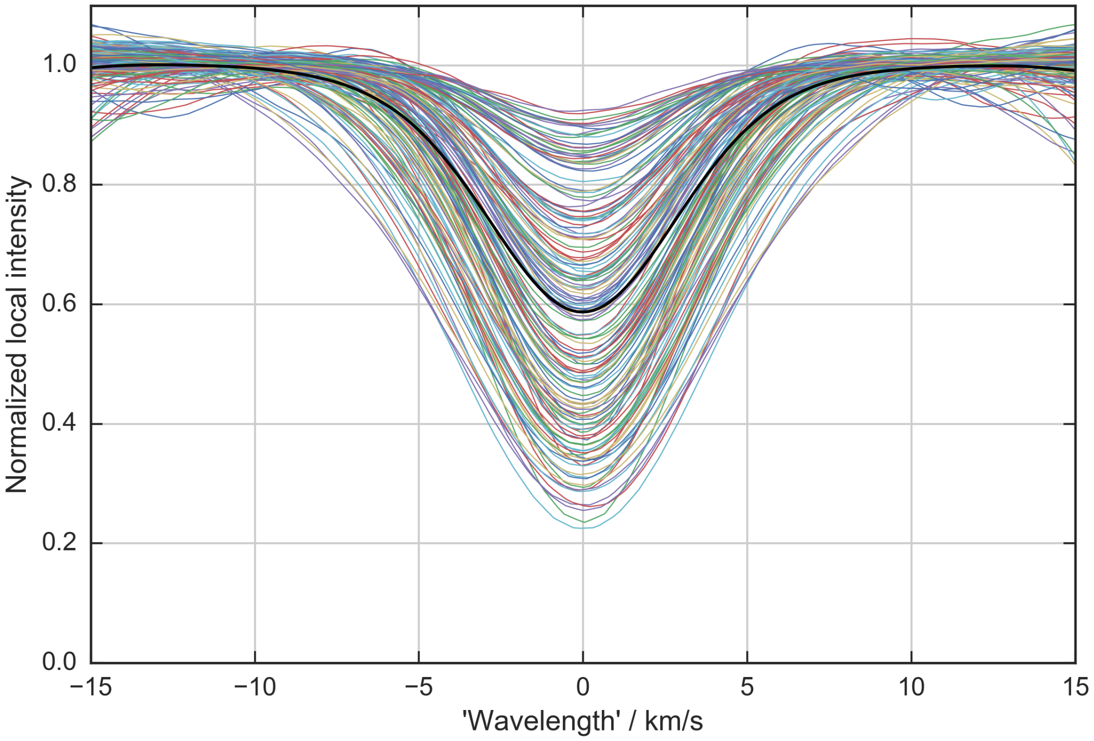

Figure 2.5: The 158 Fe I line profiles shown as the colored solid curves, averaged over all exposures from both observing runs using the procedure described in §2.2.3. The solid black curve represents the grand average of all 158 line profiles, thus forming a synthesized representative profile with central line intensity 0.59. The estimated S/N of each averaged individual line profile is about 700 and for the representative profile 9 000.

Table 2.1: The final ‘unblended’ Fe I line list containing the set of 158 lines. The wavelengths are a selection of solar Fe I lines from Stenflo & Lindegren (1977); the intensity at line center is given in units of the normalized local continuum and is obtained from the average over all exposures of the Gaussian fits to the line profiles in the HARPS spectrum of Alopex. We stress that these intensities were subject to convolution with the instrumental profile and thus do not represent ‘real’ values. The same lines are also shown in Figure 2.3.

Wavelength	Central intensity	Wavelength	Central intensity	Wavelength	Central intensity
4365.9004 Å	0.37	5432.9525 Å	0.46	6056.0114 Å	0.49
4432.5726	0.39	5445.0502	0.34	6065.4921	0.29
4445.4760	0.33	5460.8762	0.88	6082.7147	0.59
4523.4015	0.47	5461.5530	0.71	6151.6217	0.50
4551.6499	0.62	5464.2825	0.63	6157.7331	0.52
4574.2191	0.48	5470.0957	0.71	6165.3641	0.61
4593.5268	0.61	5473.9076	0.40	6173.3433	0.43
4602.0060	0.24	5487.1489	0.67	6180.2084	0.51
4657.5879	0.55	5491.8346	0.85	6200.3204	0.41
4658.2976	0.72	5493.5012	0.65	6213.4375	0.36
4672.8364	0.59	5522.4491	0.58	6219.2886	0.35
4678.8519	0.23	5525.5472	0.53	6226.7403	0.71
4726.1396	0.73	5539.2824	0.79	6232.6493	0.43
4741.5341	0.29	5543.9399	0.49	6265.1412	0.35
4785.9583	0.67	5552.6919	0.91	6270.2322	0.52
4794.3571	0.76	5568.8689	0.86	6297.8013	0.40
4799.4092	0.58	5607.6668	0.83	6311.5050	0.68
4802.5216	0.81	5611.3587	0.86	6315.8164	0.63
4808.1509	0.60	5618.6360	0.55	6322.6936	0.41
4809.9400	0.70	5635.8247	0.65	6335.3378	0.33
4839.5500	0.39	5636.6992	0.74	6380.7483	0.59
4874.3565	0.64	5638.2675	0.41	6385.7206	0.88
4875.8815	0.40	5646.6854	0.90	6392.5429	0.73
4885.4361	0.35	5651.4716	0.79	6408.0262	0.42
4892.8624	0.50	5652.3194	0.72	6430.8538	0.32
4909.3874	0.42	5661.3480	0.75	6436.4102	0.88
4918.0152	0.51	5662.5233	0.37	6481.8784	0.46
4946.3941	0.26	5677.6875	0.90	6496.4738	0.57
4950.1108	0.34	5680.2441	0.86	6498.9461	0.49
4983.2566	0.31	5701.5527	0.34	6574.2325	0.57
5044.2164	0.34	5705.4677	0.63	6581.2143	0.71
5090.7807	0.35	5717.8379	0.51	6593.8798	0.39
5141.7460	0.26	5720.8950	0.83	6608.0301	0.74
5213.8071	0.88	5731.7666	0.51	6609.1189	0.47
5223.1851	0.63	5753.1287	0.43	6627.5488	0.76
5236.2039	0.65	5775.0849	0.50	6646.9355	0.85
5242.4988	0.31	5793.9178	0.66	6703.5720	0.62
5243.7823	0.45	5807.7868	0.89	6710.3213	0.74
5250.2171	0.29	5811.9172	0.86	6737.9830	0.82
5250.6527	0.26	5814.8092	0.75	6739.5243	0.78
5253.4693	0.36	5827.8794	0.84	6745.9626	0.92
5293.9609	0.67	5835.1018	0.84	6746.9508	0.92
5294.5493	0.79	5852.2222	0.64	6750.1597	0.43
5358.1168	0.84	5858.7840	0.85	6752.7107	0.74
5365.4063	0.38	5861.1123	0.90	6793.2656	0.87
5367.4755	0.29	5881.2822	0.84	6806.8491	0.64
5369.9702	0.30	5902.4755	0.85	6820.3730	0.69
5373.7136	0.48	5916.2535	0.47	6828.5976	0.61
5379.5796	0.44	5929.6802	0.65	6839.8340	0.67
5386.3345	0.64	5956.6997	0.41	6841.3450	0.60
5389.4866	0.38	6007.9656	0.54	6843.6606	0.59
5395.2187	0.77	6027.0562	0.49	6855.1684	0.54
5417.0405	0.65	6034.0365	0.90		

2.2.2 Astrocentric correction

Before we analyze the spectra, any radial velocity (RV) noise needs to be corrected for, i.e., the star needs to be put on a static frame-of-reference, that we call the *astrocentric* frame-of-reference. There are two main sources of this RV noise, namely the Doppler shift induced by the orbiting planet[6] and the movement of the observatory relative to the target; a telescope located on the surface of the Earth is subject to the orbital velocity of the Earth around the Sun as well as the rotational velocity of the Earth itself.

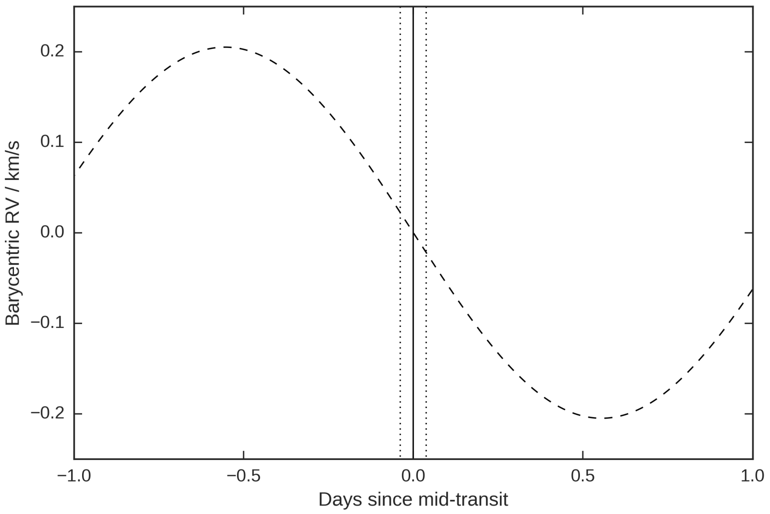

Figure 2.6: The barycentric motion of Alopex here represented by Equation (2.3). To get an astrocentric frame-of-reference, the radial velocity due to the planet is corrected for using this curve.

The HARPS spectra includes corrections such that its frame-of-reference is heliocentric, i.e., centered on the barycenter of the Solar System. To get an astrocentric frame-of-reference, we need to apply only two additional corrections: the space RV of the star and the barycentric RV induced by the planet. The former is given by the FITS header for each exposure and the latter we calculate from RV measurements of the system available in the literature. The measured RV semi-amplitude induced by Alopex b is $K = 0.205 \pm 0.006$ km/s and its orbital period $P = 2.219 \pm 0.0005$ d (Bouchy et al., 2005). Since the eccentricity of Alopex b is $e < 0.008$ (Boisse et al., 2009), i.e., its orbit is nearly-circular, we can reasonably use a sinusoidal to correct for the barycentric motion

$$\epsilon = K \sin\left(2\pi \frac{1}{P} t\right) \tag{2.3}$$

---

[6] In any system of two or more bodies, the components orbit around a common center of mass. In a planet-star system, this barycenter is close to the center of the host star and it is the projected component of this small orbit that comprises the RV signal in, e.g., detecting planets using the radial velocity method. The RV of the star around the barycenter is proportional to the mass of the planet and inversely proportional to the semi-major axis of its orbit; thus, massive planets orbiting close-in to their host star induce the largest signal.

where t is time. This correction is shown in Figure 2.6.

2.2.3 Line center determination and averaging of lines

When the HARPS spectra have been put on the astrocentric frame-of-reference, we locate the lines of interest in the spectrum of Alopex. This procedure starts by locating an interval, that we call the 'large mask', around the spectral line and then normalizing the intensity to the continuum in the large mask. To determine the line center and get a better estimate of the local continuum around the line, we fit a five-parameter Gaussian to the flux in the immediate vicinity, or what we call the 'small mask', around the line. No consideration is taken to normalizing the full spectrum to the slowly increasing slope of the continuum as seen in, e.g., Figure 2.1.

The wavelength and flux arrays are obtained from the FITS file. Elements in the original wavelength array are separated by 0.01 Å; to make any wavelength shifting in the line profile easier to handle later in the analysis, we interpolate the flux array using a spline interpolation of first order, such that the element separation is 0.003 Å[7]. We then define a large mask around the line central wavelength as given by the line list. The large mask spans 500 wavelength elements in each direction from the line center, for a total of about 3 Å, see Figure 2.7. A 'zeroth order' normalization to the local continuum is made by dividing the large mask spectrum by its largest intensity value; a 'first order' local continuum is then found by dividing the large mask spectrum by the median of the flux with values above 0.95 in intensity of the zeroth order normalization.

To find the line center of a line, we make a non-linear least squares fit of a five-parameter Gaussian[8] to a small mask in λ centered around the line list central wavelength λ_0,

$$y\left(\lambda|\boldsymbol{\theta}\right) = \theta_1 + \theta_2(\lambda - \lambda_0) - (1 - \theta_3) \cdot \exp\left[-\left(\frac{\lambda - \theta_4}{\theta_5}\right)^2\right] \tag{2.4}$$

where θ_1 is the continuum value, θ_2 the slope of the continuum, θ_3 the line intensity at line center, θ_4 the line center and θ_5 the line width. The small mask in λ is selected such that it covers the full width of the line and a small bit of the continuum surrounding the line, i.e., 140 wavelength elements or about 0.4 Å, see Figure 2.7. The parameters obtained in the fit give the final value of the local continuum and the line center. The formal uncertainty of the fit is given by the square root of the diagonal of the covariance matrix and is of the order 10^{-4} Å for most line centers, which is two orders of magnitude smaller than the significant figures given in the line list.

---

[7] The 0.01 Å separation corresponds to a Doppler shift of 0.5 and 1 km/s at 6 000 and 3 000 Å, respectively. The smaller separation of 0.003 Å similarly corresponds to around 0.15 and 0.3 km/s. This decrease in separation means that the flux array increases in length from 313 119 to 1 000 000; anything longer than this is found to increase the computational load substantially.

[8] A Gaussian function is found to fit better to the line profile than a Lorentzian one.

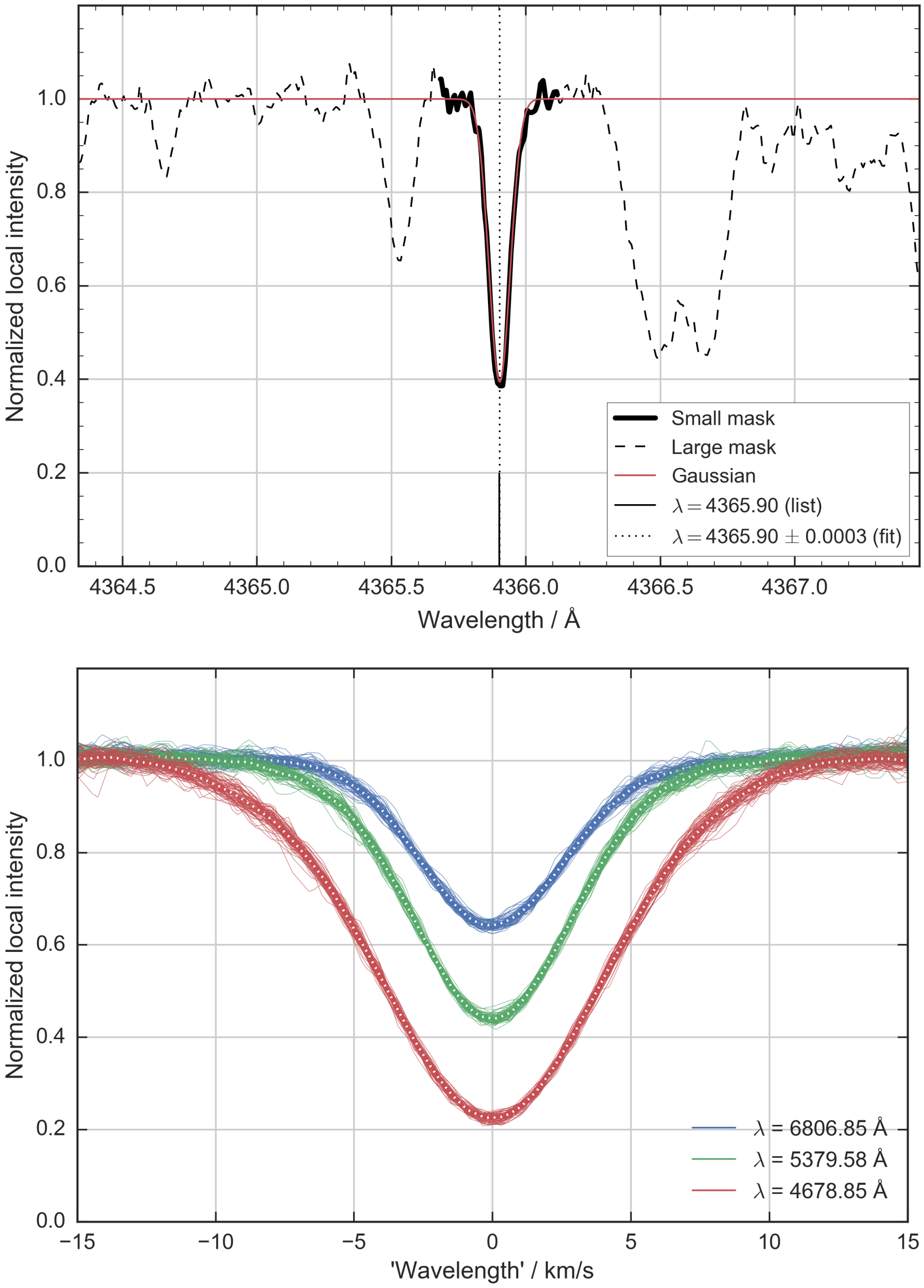

Figure 2.7: The top panel shows a zoom-in on the large mask around a line from the line list with central wavelength $\lambda = 4365.90$ Å, normalized to the local continuum. The solid red curve shows a Gaussian fitted to the small mask. The bottom panel shows three Fe I lines with different line depths, with all exposures shown as solid curves and their average as the dotted curve. The individual exposures of each line are plotted against their respective central wavelength given by the average of the Gaussian fits and are thus measured against the same rest frame. The S/N of a typical averaged profile is around 700.

2.2.4 Forming collated transit epochs

There are 20 in-transit exposures per observing run, totaling 40 available transit exposures over the transit chord, see Figure 2.8. To increase the S/N, we collate the exposures such that two exposures from each observing run, totalling four exposures, form one *transit epoch*; this increases the S/N by a factor two and gives a sequence of 10 epochs, which is enough to eludicate any effects between the ingress and egress side of the transit. The time of these epochs is taken to be the mean of the four exposure start times, shown as the colored stars in Figure 2.8.

Although collating the epochs somewhat smears out the probing area of the planet, in effect decreasing the spatial resolution, the gain in S/N is favored. Moreover, as the number of granules on the stellar surface covered by the planet varies over time, the fourfold increase of the total exposure time to 1 200 s at full overlap increases the statistical stability of any effects due to convection on the line profiles.

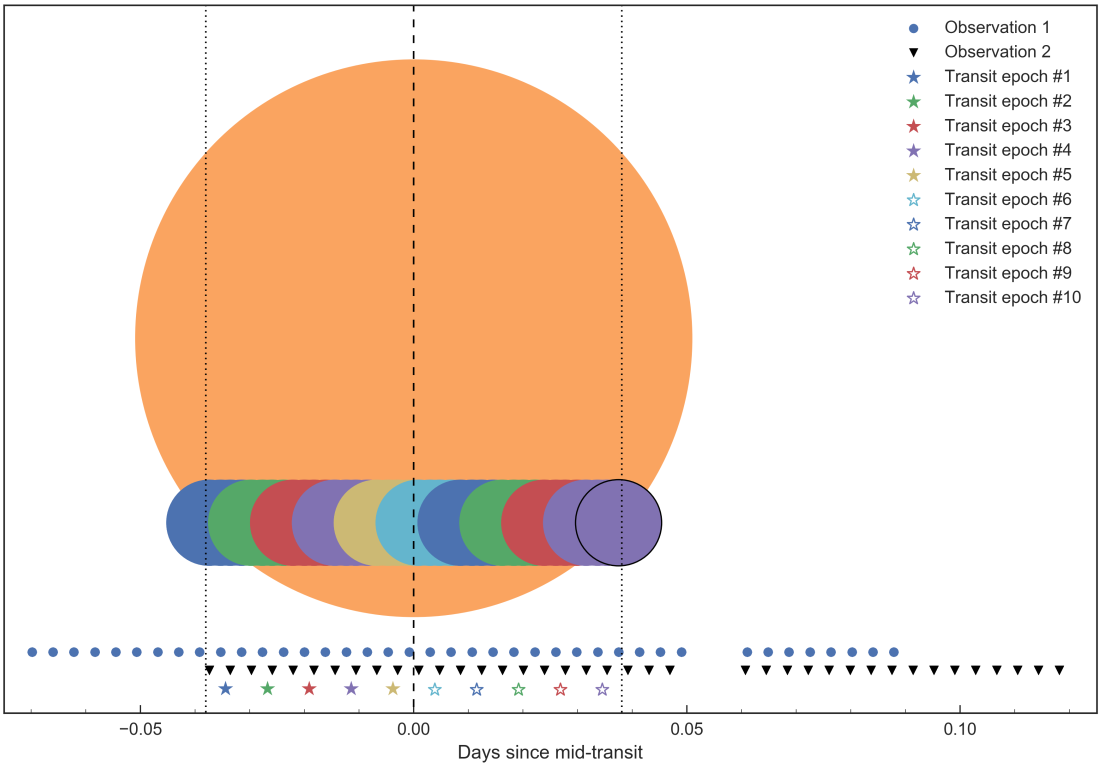

Figure 2.8: The transit geometry of Alopex and Alopex b with impact parameter $b = 0.66$ (Agol et al., 2010). The transit epochs are collated using two exposures from each observing run, forming an elongated area along the chord of the transit. It is behind these areas that the spatially resolved line profiles of the stellar spectrum are obtained. The position of mid-transit is shown as the dashed vertical line; transit ingress and egress as dotted vertical lines. The black circle shows the planet size to scale.

2.3 Line profile ratios during transit

The change in the spectrum during the different transit epochs compared to the integrated spectrum outside transit is tiny. Figure 2.9 shows the effects during different transit epochs on the representative profile obtained from averaging the 158 Fe I lines (Figure 2.5). The small size of this effect necessitates some alternative approach to measuring the shift in the line profiles during transit. One such approach is taking the ratio of the line profiles in-transit to the line profile outside transit, where the latter forms a rest-frame against which the in-transit line profiles during different transit epochs are measured.

To illustrate and quantify the approach, we take the ratio of Gaussian profiles successively shifted by 0.01 km/s, representing the in-transit profiles, over one static Gaussian profile representing the spectrum outside transit, see Figure 2.10. The amplitude of the ratio varies with line strength; for the line strength of the lines used in Figure 2.10 (similar to the representative profile in Figure 2.9), a ratio amplitude of about 0.005 corresponds to a ‘wavelength’ shift of about 0.05 km/s. This shift corresponds to the anomalous RV shift measured by the Rossiter-McLaughlin effect.

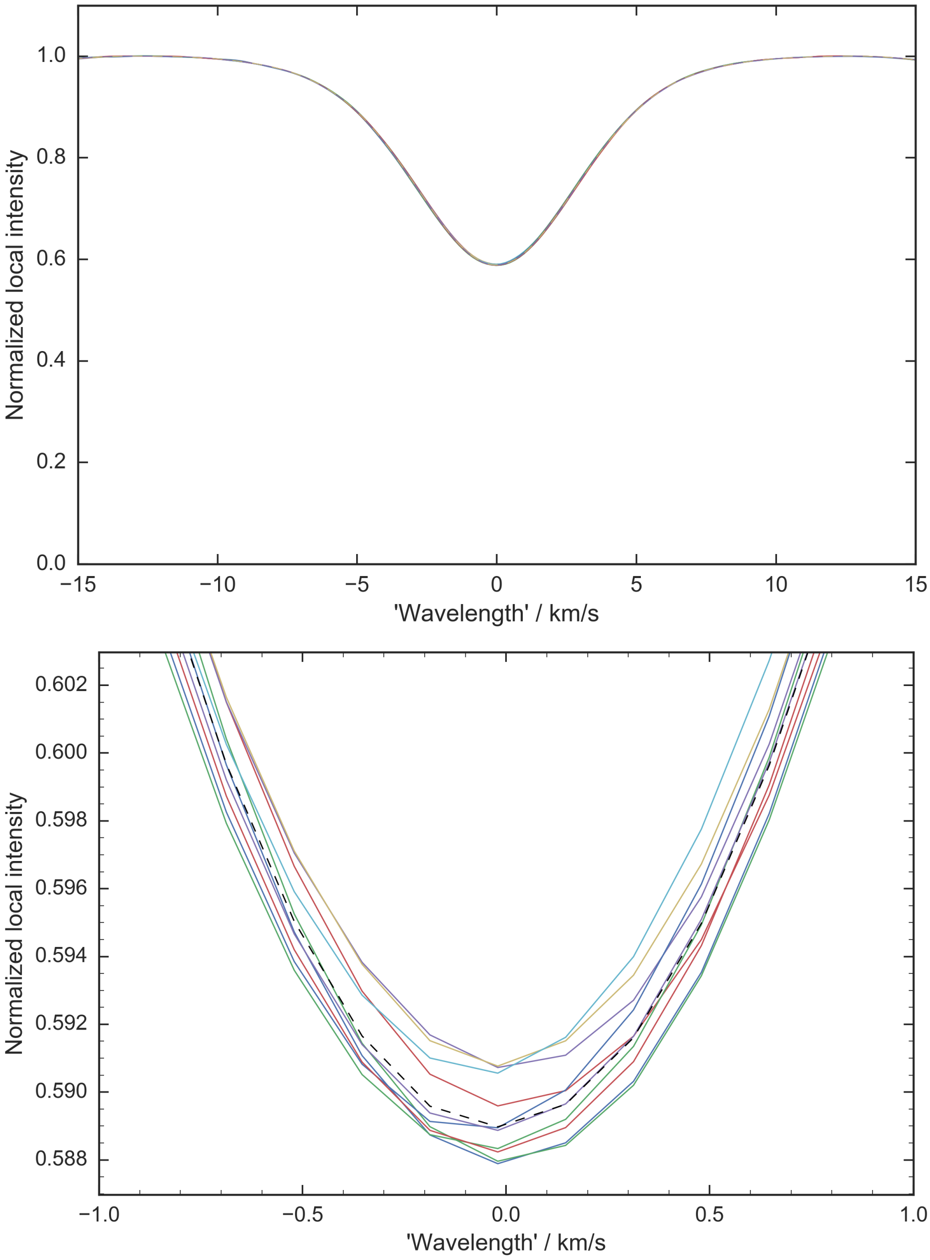

Figure 2.9: A representative profile is here shown for every transit epoch (solid colored curves, corresponding to those in Figure 2.8) and for that outside transit (dashed black curve). As seen in the top panel, the difference in the profiles during different transit epochs is minuscule and hard to appreciate on this scale. The lower panel shows a zoom-in of the bottom of the line profile; the change in intensity between the different epochs is on the order of one part per thousand.

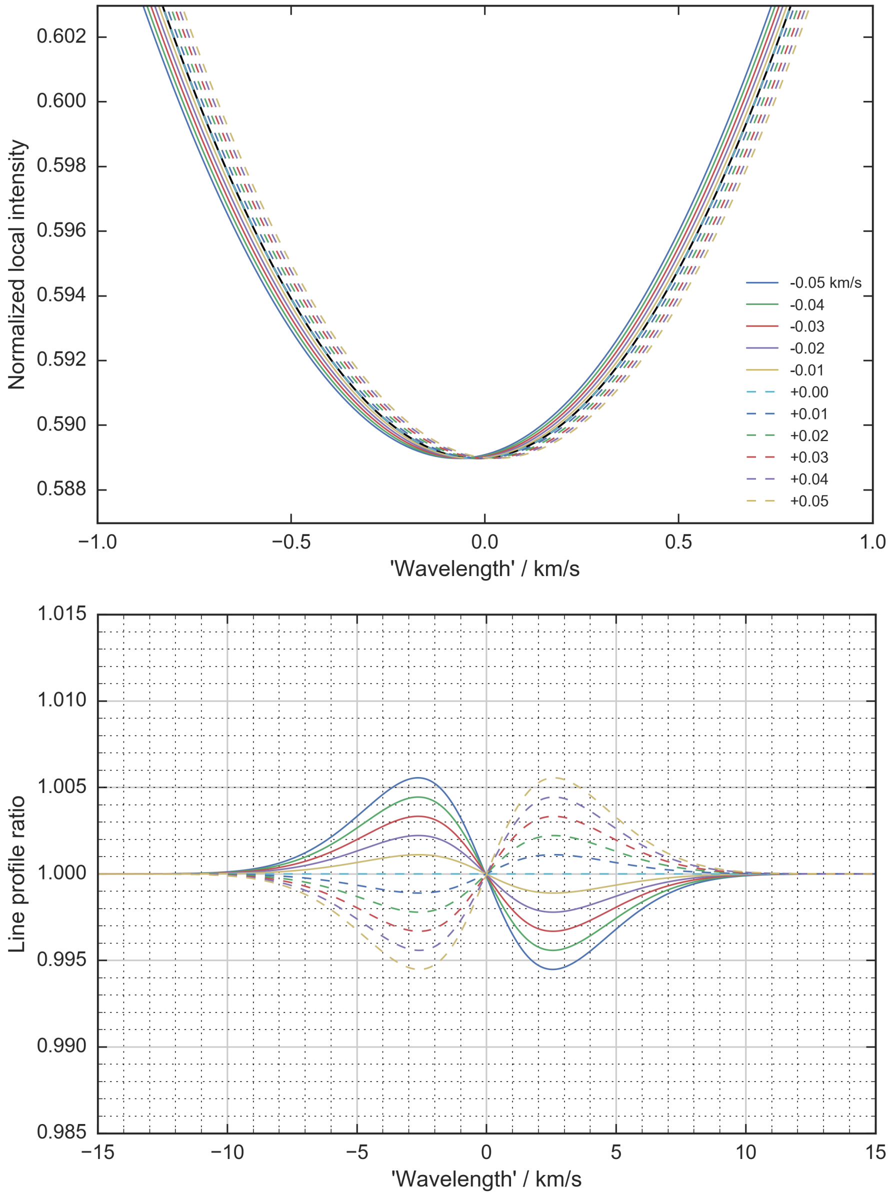

Figure 2.10: The top panel shows a zoom-in on the bottom of simulated line profiles with central line intensity 0.59 (equal to the grand average of that in Figure 2.5) represented by Gaussian functions slid across each other from -0.05 to 0.05 km/s. The bottom panel shows the resulting ratios with corresponding colors.

2.3.1 Line profile ratios of the representative profile from 158 Fe I lines

The in- to out-of-transit line profile ratios for the representative profile obtained from averaging the 158 Fe I lines (Figure 2.9) are shown in Figure 2.11. The ratio obtains a maximum amplitude of around 0.005, which for this line strength roughly corresponds to a ‘wavelength’ shift of 0.05 km/s, as calibrated above. Also shown as dashed lines are the ratios from the integrated spectrum pre- and post-transit (i.e., averaged over all pre- and post-transit exposures, respectively) against the spectrum outside transit (averaged over all exposures outside transit), which are, as expected, flat.

To better appreciate the time sequence as the planet scans across the stellar disk, we plot in Figure 2.12 the ratios at different transit epochs successively shifted downwards by a value of 0.01. Although no precise comparison is presently possible, these ratios show a similar quantitative amplitude and qualitative sequence to that predicted by 3D hydrodynamic models, shown for a star with similar parameters in Figure 1.4. We note that a basic model with a rotating, flat stellar surface would produce similar curves, as indeed Figure 2.10 also does; however, the 3D hydrodynamics affect the detailed shapes of the curves.

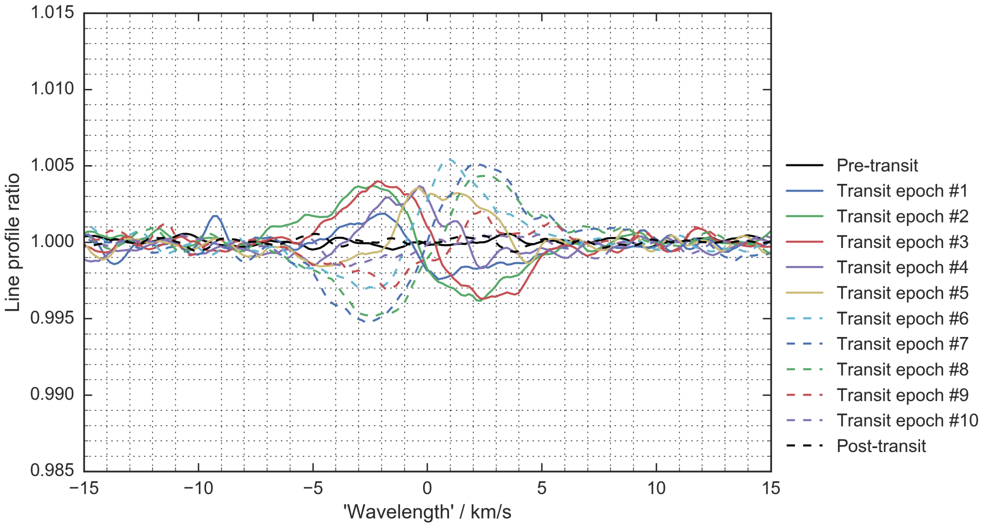

Figure 2.11: The in- to out-of-transit line profile ratios for the representative profile obtained from averaging the 158 Fe I lines. The transit epochs correspond to those in Figure 2.8. The ratio obtains a maximum amplitude of around 0.005, which for this line strength corresponds to a ‘wavelength’ shift of about 0.05 km/s; this is equivalent to the Rossiter-McLaughlin effect. The solid and dashed black curves show the ratios of the averaged profiles over exposures from pre- and post-transit to the profile averaged over all exposures outside transit, respectively; for these, in the astrocentric frame-of-reference, no wavelength shift and thus a flat ratio is expected. The same ratios shifted vertically are shown in Figure 2.12.

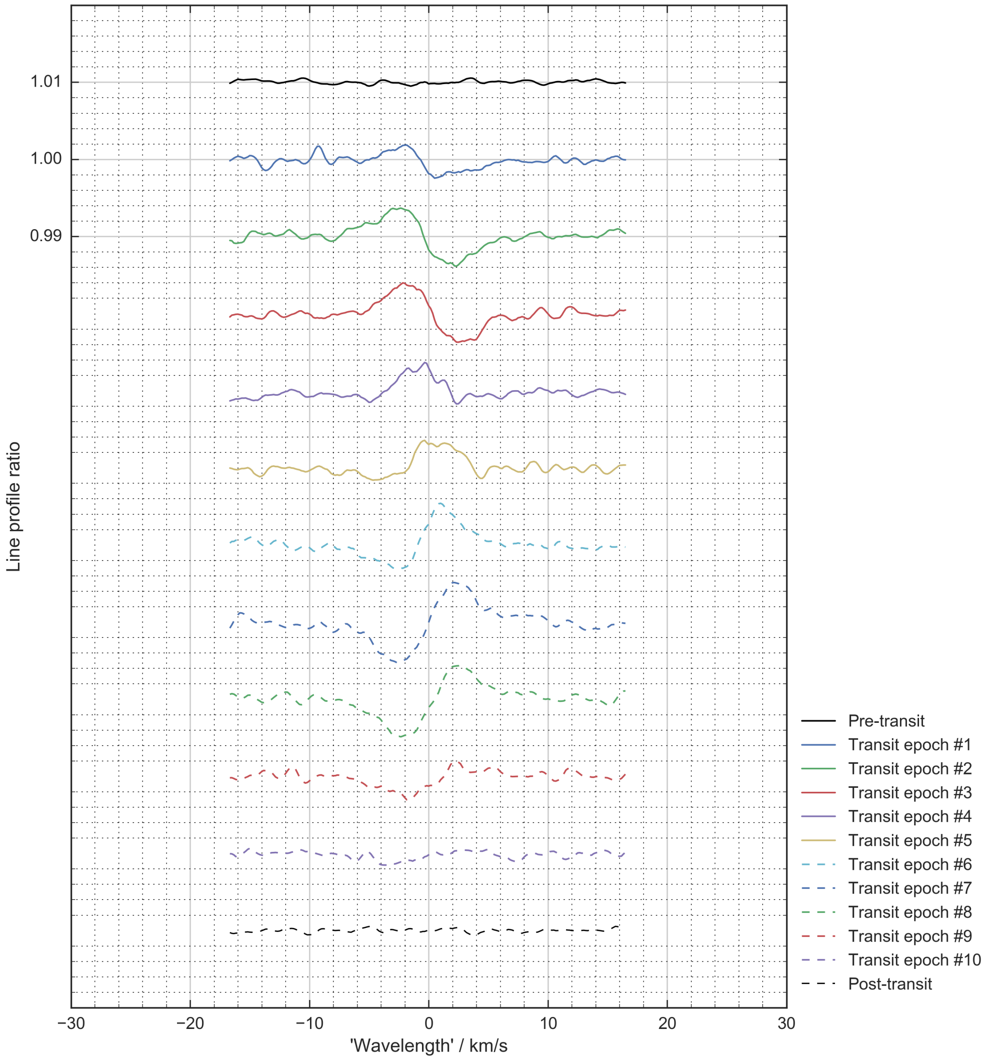

Figure 2.12: The same line profile ratios as shown in Figure 2.11, shifted downwards by 0.01 for each transit epoch to show their sequence. The sequence is analogous to that predicted by 3D hydrodynamic models shown in Figure 1.4.

2.4 The Rossiter-McLaughlin effect

Although the Rossiter-McLaughlin (RM) effect is usually determined by cross-correlating the complete (within the wavelength scale of the spectrograph), integrated stellar spectrum to measure the anomalous RV shift during transit, it can also be obtained by finding the central wavelength of individual line profiles during different transit epochs. We find these central wavelengths of the representative profile obtained from the 158 Fe I lines by fitting the Gaussian in Equation (2.4) (with the continuum and continuum slope parameters held fixed at $\theta_1 = 1$ and $\theta_2 = 0$, respectively). The result is shown in Figure 2.13. There is indeed a resemblance to a prograde RM waveform (cf., Figure 1.6) with similar amplitudes as that measured for Alopex (e.g., Winn et al., 2006).

As the RV shift is here measured for individual spectral lines as opposed to the complete spectrum, the results are not expected to be as precise. We note also that the values obtained for the central wavelength in the curve-fitting depends on what function is chosen; a Gaussian is here used for its simplicity, but it is clear that it does not fit the representative profile optimally, as shown in Figure 2.14. For these reasons, we do not attempt any further quantitative analysis, but show only that measurements of the RM effect using an averaged representative line profile are possible.

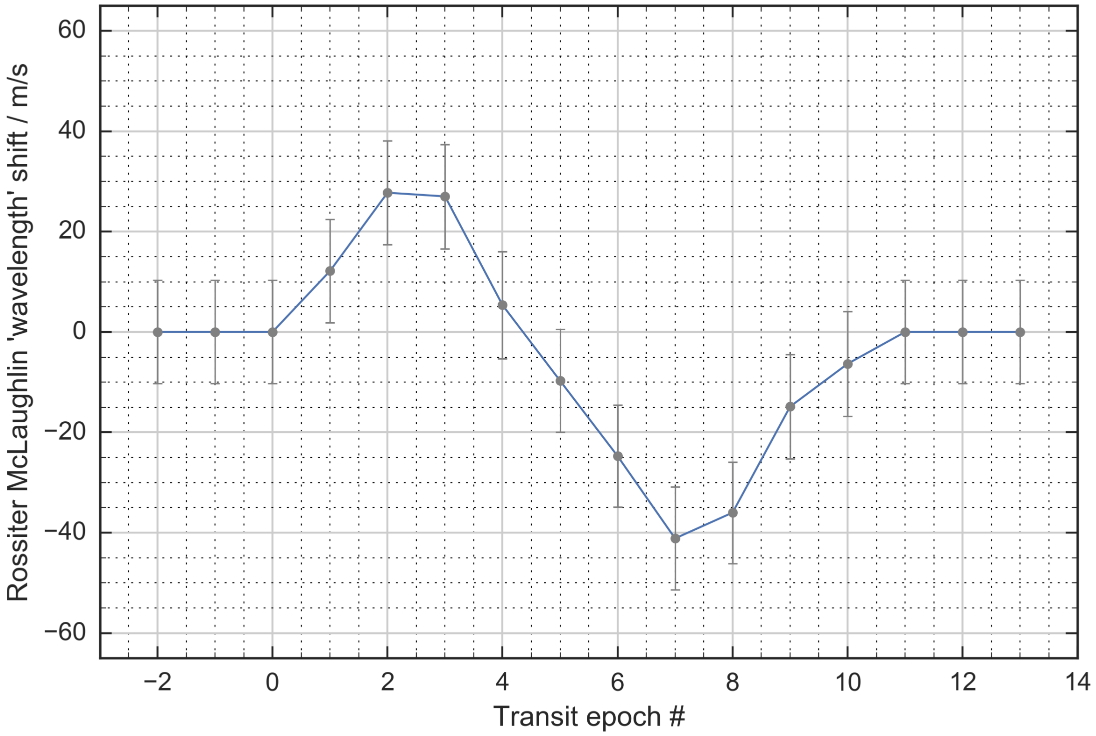

Figure 2.13: The line centers obtained from Gaussian fits to the representative profiles in- and out-of-transit yield the Rossiter-McLaughlin effect. The epochs before #0 and after #10 show the value obtained for the out-of-transit profile. The uncertainty is the formal one standard deviation obtained in the fit.

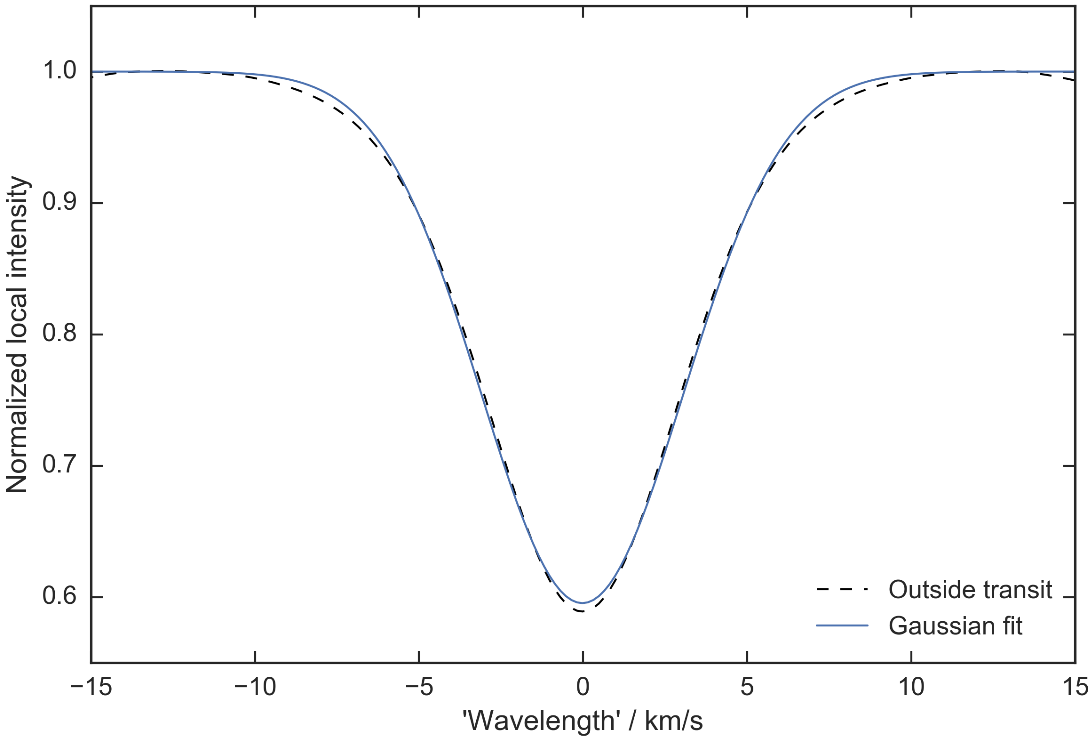

Figure 2.14: The outside-transit representative profile (dashed curve) fitted with a Gaussian (blue solid curve). The fit is visibly not optimal, as both the wings and intensity at line center are too shallow.

2.5 Reconstructing spatially resolved line profiles

Above we have analyzed line profiles from spectra integrated over the whole stellar disk. Now, we want to obtain line profiles from different disk positions. The basic principle of obtaining spatially resolved line profiles using exoplanet transits is illustrated in Figure 2.15; we subtract the spectrum in-transit, weighted by the area covered by the planet, from the spectrum outside transit, yielding the spectrum of the stellar atmosphere behind the planet.

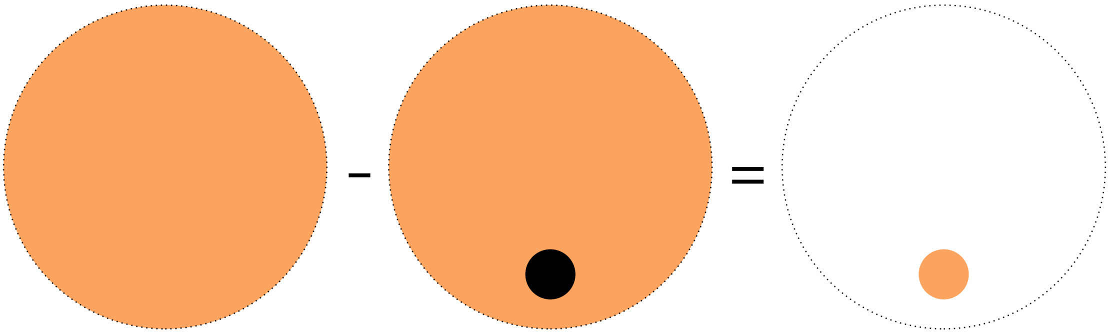

Figure 2.15: Illustration of the principle used to reconstruct spatially resolved line profiles during transit. The spectrum in-transit is subtracted from the spectrum outside transit to yield the spectrum behind the planet.

To weigh the planetary area correctly, the flux removed by the planet at each transit epoch must be known. This hidden flux, or effective planetary area, A_{eff}, is the product of the local stellar brightness and the area of the planet; it can be calculated from the transit geometry and limb-darkening law of the star. However, the value of A_{eff} can also be obtained directly from the photometric light curve during transit. We use as A_{eff} the photometric normalized intensities during a transit from the light curve by Pont et al. (2007) obtained with the Hubble Space Telescope (HST) Advanced Camera for Surveys (ACS)[9], see Figure 2.16; a list of the specific values used for each transit epoch is given in, e.g., Table 2.2.

---

[9] Due to its atmosphere, the size of the planet varies depending on the wavelength with which it is observed. The photometry of the HST ACS covers 5 500–10 500 Å and thus has a slightly longer average wavelength than the HARPS spectra (3 800–6 900 Å). However, slight errors in effective planetary area are found by Dravins et al. (2017) to not significantly affect the results.

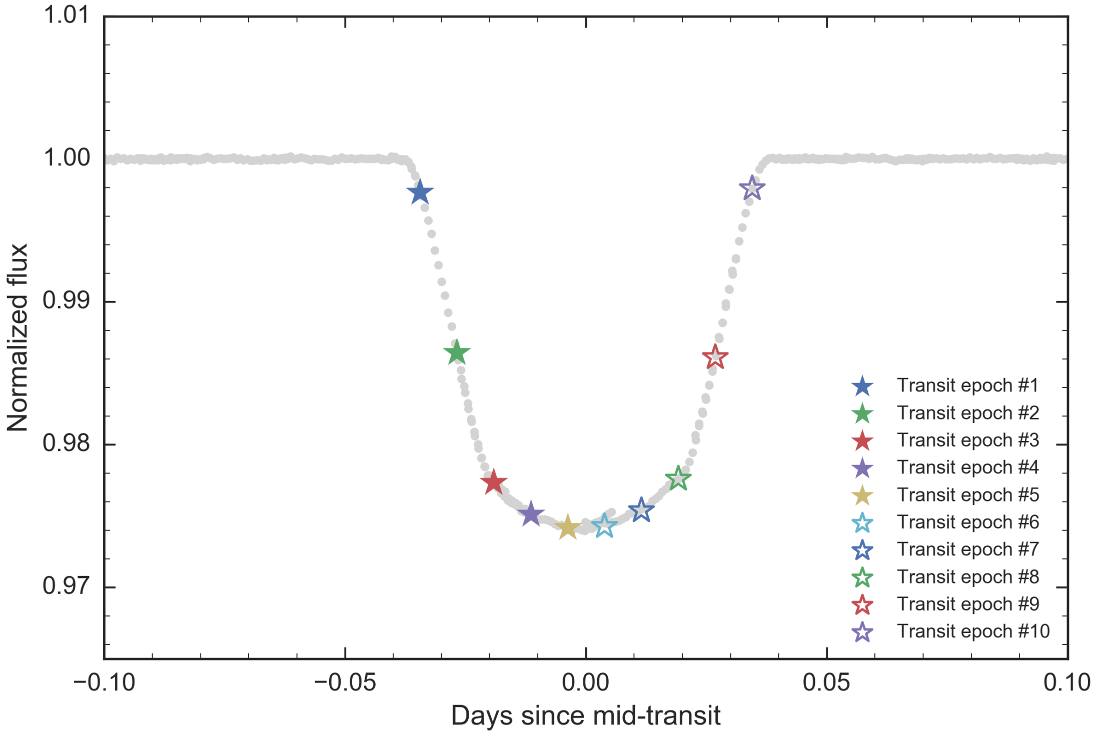

Figure 2.16: The phase folded HST light curve of three Alopex b transits (gray dots) by Pont et al. (2007). The normalized flux corresponds to A_{eff}; its value at each transit epoch is marked with a colored star, corresponding to those in Figure 2.8, and shown in, e.g., Table 2.2.

The method is elaborated in Figure 2.17, where the right-hand panel shows two idealized Gaussian profiles; one profile is centered at 0 km/s, representing the static outside-transit spectrum, and the other is shifted slightly in wavelength, representing a spectrum during transit. For demonstration purposes, we set for our hypothetical planet $A_{\text{eff}} = 0.1$. The flux behind the planet is obtained by

$$F_{\text{behind}} = F_{\text{out-transit}} - (1 - A_{\text{eff}})\, F_{\text{in-transit}}. \tag{2.5}$$

The normalized reconstructed profile is then obtained by dividing F_{behind} by A_{eff}. The same method using HARPS data is shown in the bottom panel of Figure 2.17, where $A_{\text{eff}} = 0.015$.

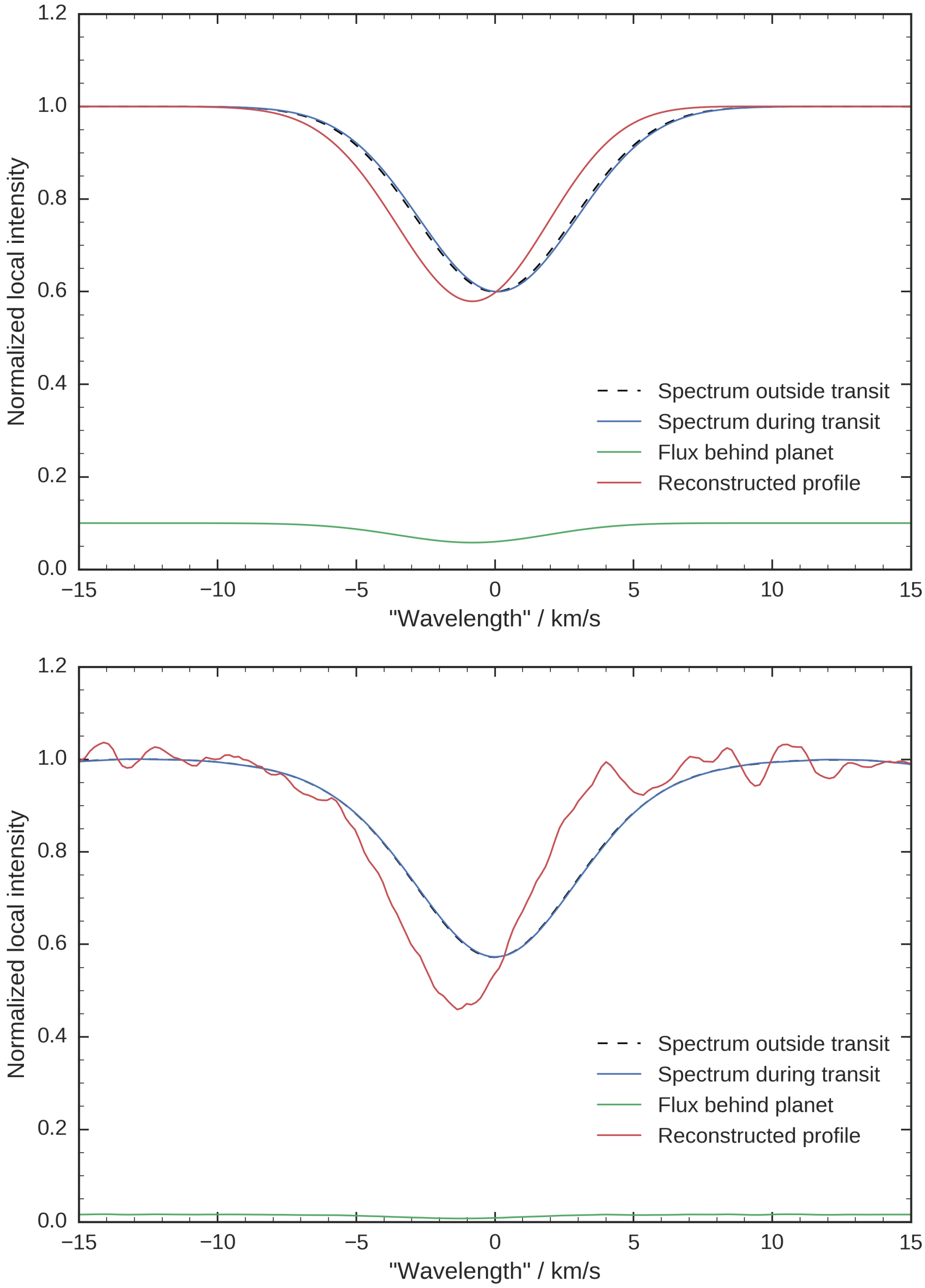

Figure 2.17: The principle for reconstructing the line profile behind the planet. The top panel shows the procedure for an idealized Gaussian profile shifted slightly in central wavelength during transit; the effective area of the hypothetical transiting planet is an exaggerated 10 % of the stellar disk area. The bottom panel shows the same procedure for the HARPS data using an effective planetary area of 1.5 %. The resulting S/N of the reconstructed profile is around 30.

2.5.1 Reconstructing spatially resolved representative profiles from 158 Fe I lines

The representative profile obtained from averaging the 158 Fe I lines is reconstructed at transit epochs 2–9, i.e., at different stellar disk positions, in Figure 2.18; the top panel shows the data and the bottom panel the Gaussian fits to the data. The profiles for epochs 1 and 10 are shown in Figure 2.19; no reliable Gaussian fits are obtained for these profiles as the S/N is too poor. The parameters of the Gaussian fits of epochs 2–9 and the S/N and A_{eff} (obtained from Figure 2.16) of all epochs are shown in Table 2.2.

The spatially resolved line profiles in-transit are in general deeper and narrower than the integrated profile from outside transit, as they are not subject to rotational broadening. There is also a sequence of shifting of the central wavelength from slightly blueshifted at the ingress side of the transit to redshifted at the egress side; this shift is more readily seen in Figure 2.20, where the line profiles are displaced vertically each transit epoch. This shift in central wavelength is due to the rotation of the star at the latitude of the transit chord and its transition from a blueshift to a redshift reflects the prograde motion of the planet.

Figure 2.21 shows how the line width varies with transit epoch. 3D hydrodynamical models predict an increase in the line width towards the limbs, as the horizontal convective velocity dispersion increases there. The reconstructed line profiles show a trend of broadening towards the limb on the egress side of the transit, but not on the ingress one. We note that observations of the limbs are difficult; the significantly lower S/N there result from the fully pronounced limb darkening and only part of the planet covering the stellar disk.

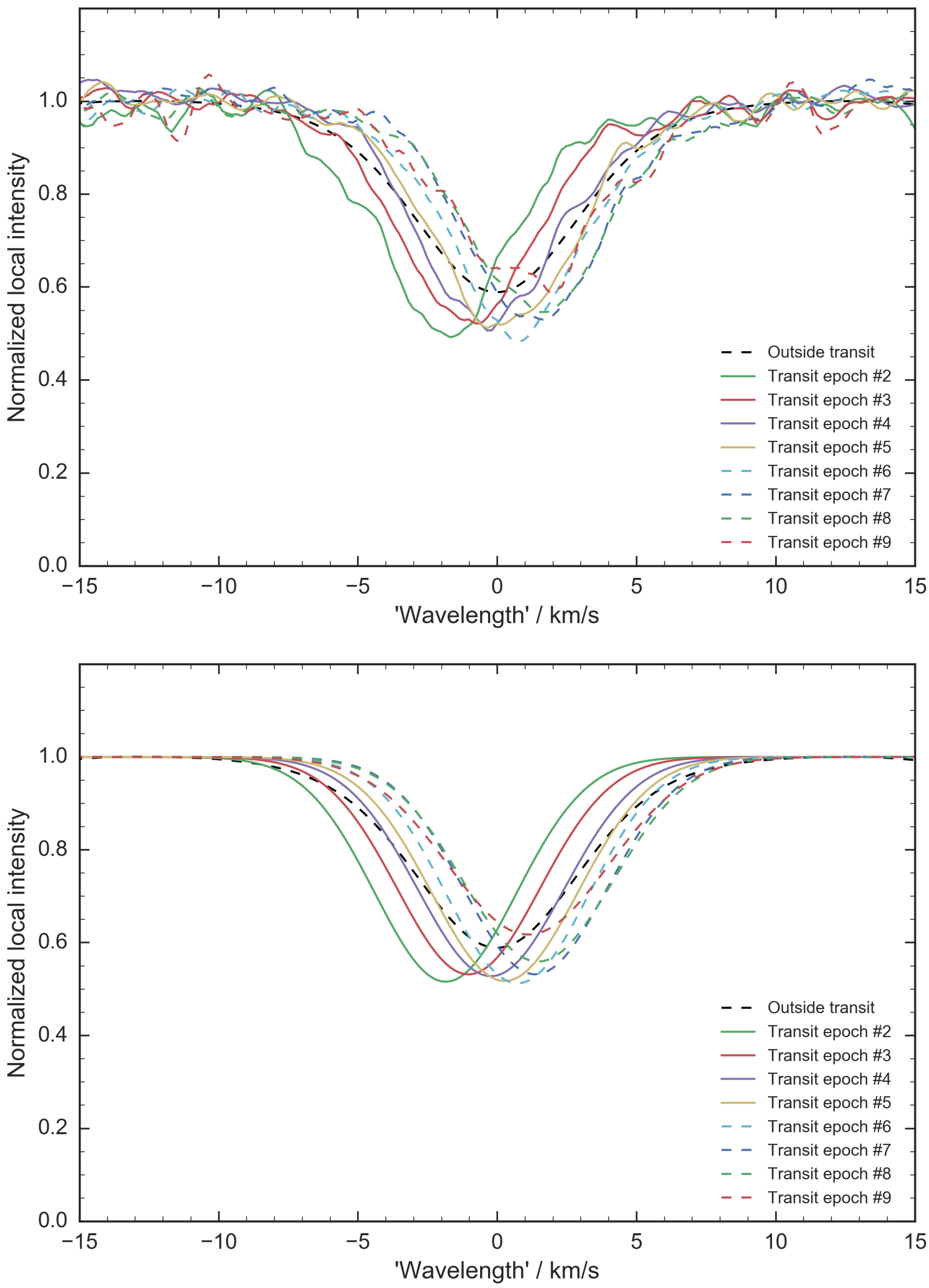

Figure 2.18: Spatially resolved reconstructed line profiles from the spectrum behind the planet for the representative profile obtained from averaging the 158 Fe I lines. The top panel shows the reconstructed profiles against the profile outside transit (black dashed line); the bottom panel their fitted 5 parameter Gaussians. The colors of the curves correspond to the transit epochs in Figure 2.8.

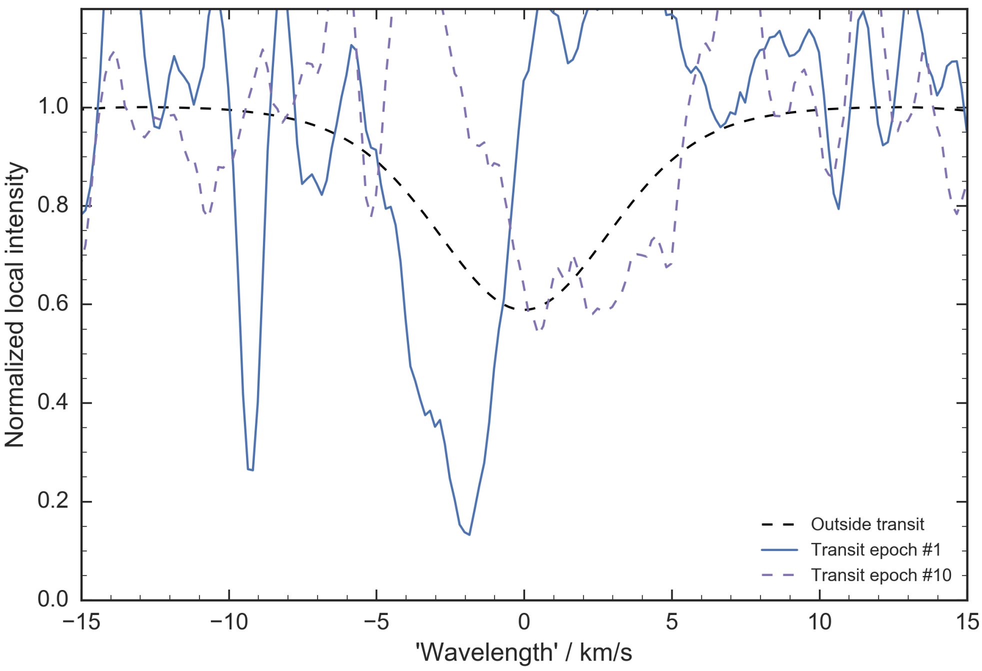

Figure 2.19: The reconstructed profile of the first and last epoch, i.e., at the limbs of the star, have poor S/N due to limb darkening and only part of the planet covering the stellar surface. No reliable Gaussian fits are obtained for these profiles and are therefore omitted.

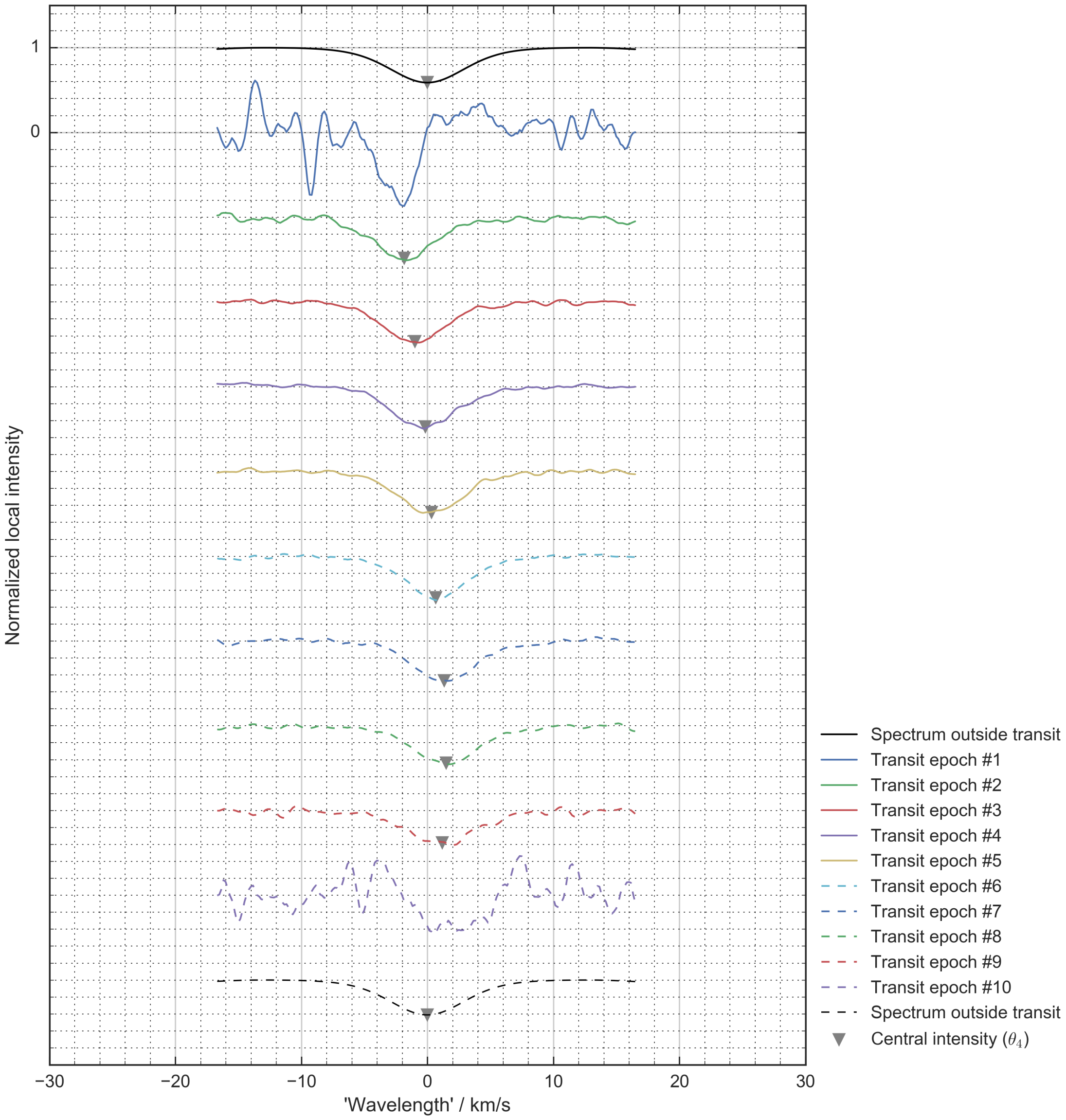

Figure 2.20: The spatially resolved reconstructed line profiles shifted down by 1 on the intensity axis for each transit epoch to show the sequence as the planet scans the stellar disk. The gray triangles show the fitted Gaussian center values (θ_4). The line centers shift due to the rotation of the star and in a fashion reflecting the prograde motion of the planet.

Table 2.2: The obtained parameters from the Gaussian fit[a] to the representative profile formed from 158 Fe I lines during the different transit epochs. Epoch numbers correspond to those in Figure 2.8. The uncertainties are the formal one standard deviation obtained in the fit.

Transit epoch	A_{eff}[b]	Central intensity (θ_3)	Line center (θ_4)	Width (θ_5)	S/N[c]
Outside transit		0.60 ± 0.001	-0.02 ± 0.010 km/s	4.35 ± 0.015 km/s	6400
#1	0.0023				5
#2	0.0136	0.52 ± 0.007	-1.85 ± 0.044	3.59 ± 0.062	27
#3	0.0227	0.53 ± 0.004	-1.03 ± 0.026	3.62 ± 0.036	46
#4	0.0249	0.53 ± 0.004	-0.23 ± 0.027	3.70 ± 0.039	50
#5	0.0258	0.52 ± 0.004	+0.26 ± 0.024	3.70 ± 0.033	52
#6	0.0257	0.51 ± 0.004	+0.73 ± 0.024	3.62 ± 0.035	52
#7	0.0246	0.53 ± 0.005	+1.37 ± 0.031	3.64 ± 0.043	50
#8	0.0224	0.56 ± 0.005	+1.46 ± 0.032	3.81 ± 0.045	45
#9	0.0139	0.62 ± 0.006	+1.12 ± 0.053	4.09 ± 0.075	28
#10	0.0021				4

---

[a] The continuum and continuum slope parameters in Equation (2.4) are here held fixed at $\theta_1 = 1$ and $\theta_2 = 0$, respectively.

[b] Obtained from Figure 2.16.

[c] Calculated using Equation (2.2) multiplied by A_{eff}.

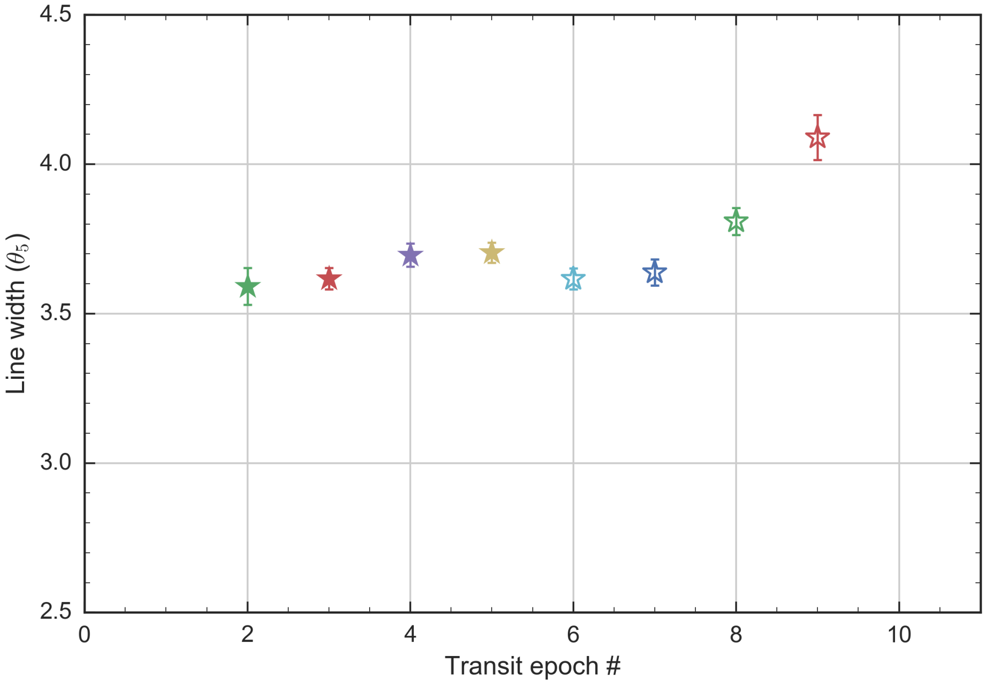

Figure 2.21: The reconstructed line profile widths at transit epochs 2–9. Epochs 1 and 10 are omitted as no reliable fits are obtained. The uncertainties are the formal one standard deviation from the fits. 3D hydrodynamical models predict an increase in the line width towards the limbs; a slight such broadening is seen here, but only near one of the limbs.

2.6 Effects from varying the line selection

2.6.1 'Strictly unblended' lines

To determine if the results for the representative profile formed from 158 Fe I lines are affected by excessive blends contained in that set of lines, we run the same procedures as above (§2.3 and §2.5) with a representative profile formed from a subset of the 158 lines that we determine are less blended. A line in the set of 158 is determined to be 'strictly unblended' when, in the profile averaged over all exposures as shown in Figure 2.22, the normalized local intensity does not obtain a value below 0.95 at ±15 km/s on the 'wavelength' axis. This new set of lines, totaling 74, are shown in Figure 2.22.

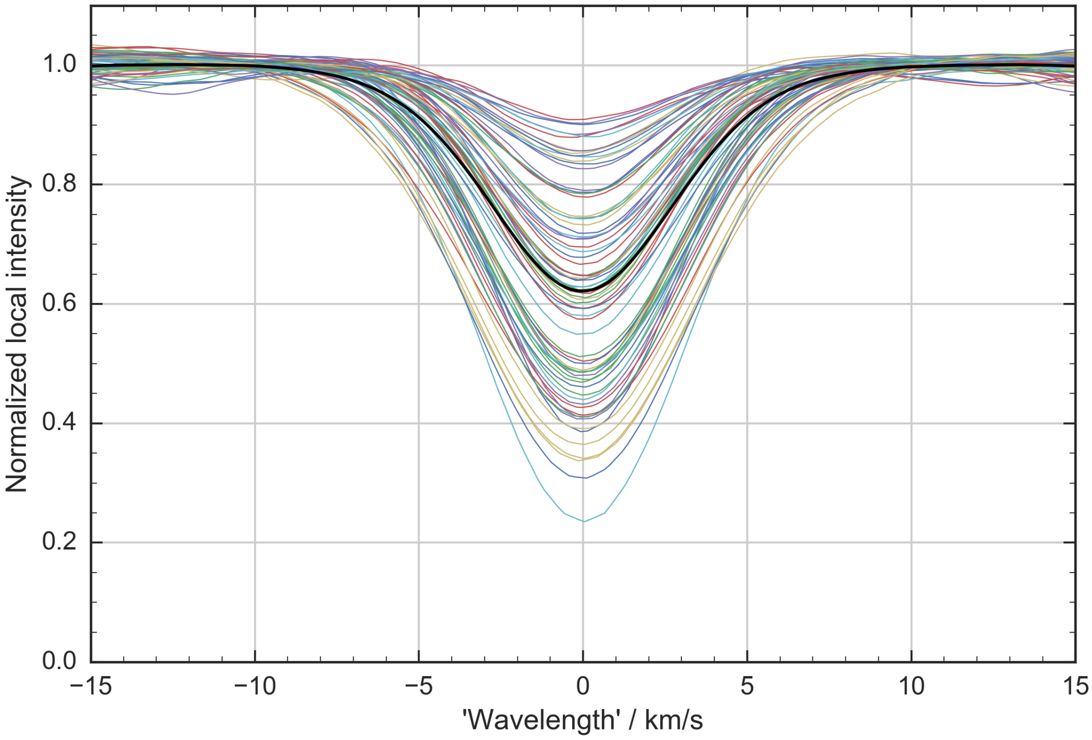

Figure 2.22: A subset of lines with less blending from the 158 Fe I lines in Figure 2.5, totaling 74 lines. The solid black line is the grand average of all the lines in this subset, forming a synthesized representative profile with 0.63 line center intensity (cf., 0.59 for the grand average from the one from 158 lines).

Line profile ratios

The in- to out-of-transit profile ratios are shown in Figures 2.23 and 2.24; these have similar amplitudes to the ratios of the representative profile comprised of 158 lines, as expected from their similar central line intensity (0.59 for the profile fom 158 lines and 0.63 for the one from 74); they also show the same prograde Rossiter-McLaughlin wavelength shift.

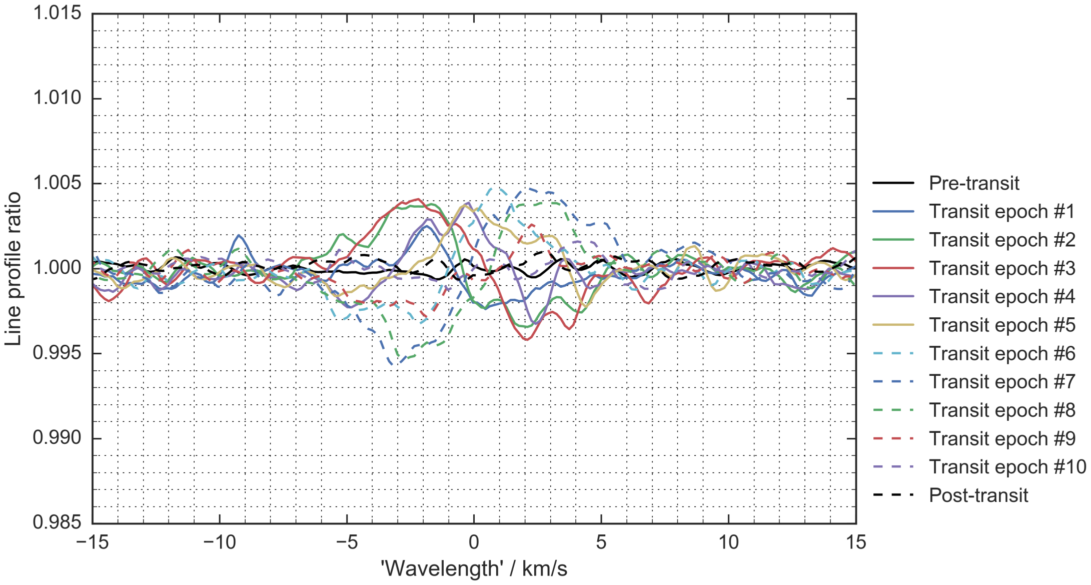

Figure 2.23: The in- to out-of-transit profile ratios for the representative profile from the less blended subset of 74 Fe I lines. The amplitudes are similar to that in Figure 2.11, as expected, since the representative profiles are of similar depth.

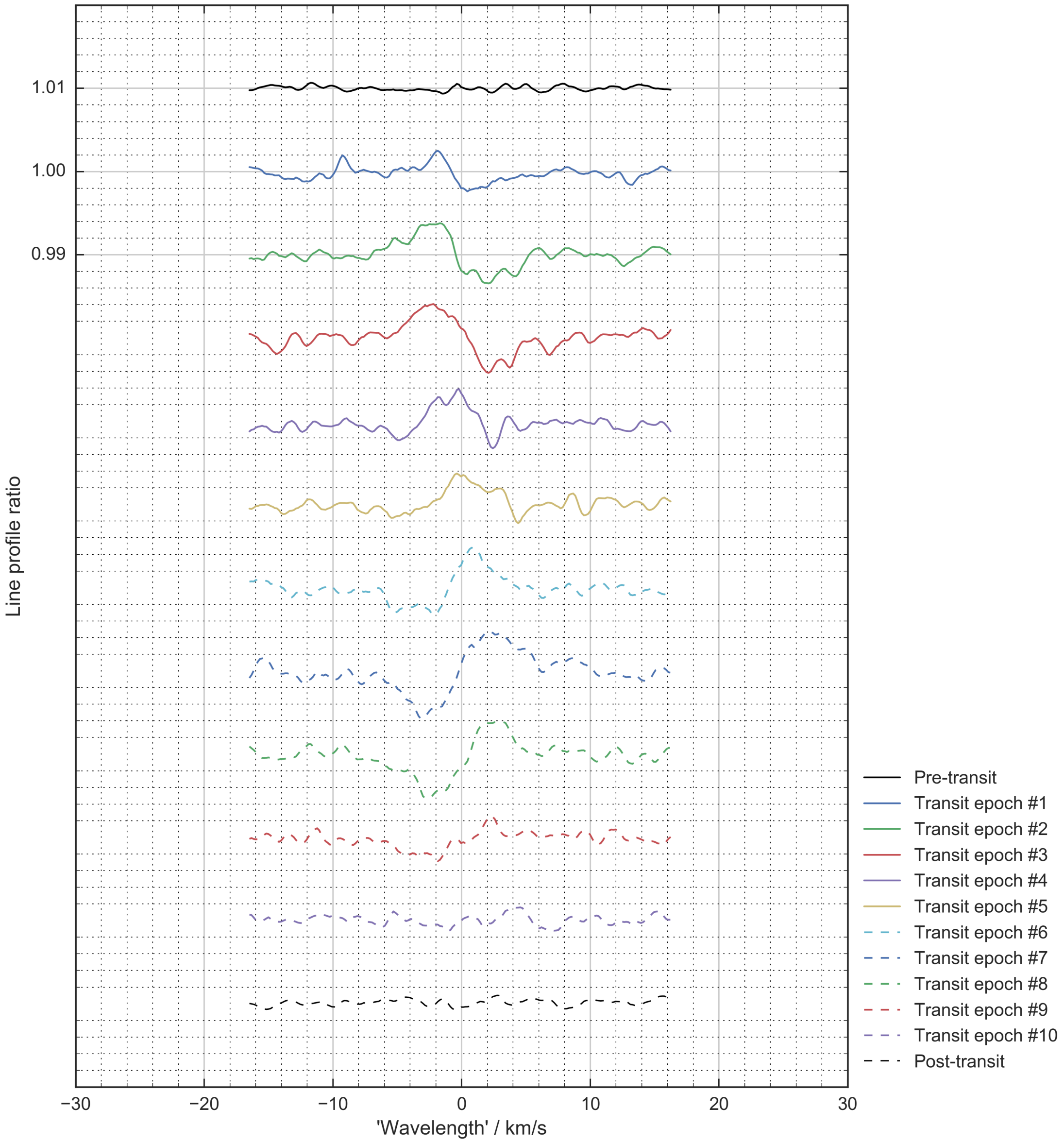

Figure 2.24: The sequence of the in- to out-of-transit profile ratios for the representative profile from the less blended subset of 74 Fe I lines. The S/N is slightly decreased compared to the ratios for the representative profile obtained from averaging the 158 Fe I lines, shown in Figure 2.12.

Reconstructed, spatially resolved profiles

The reconstructed, spatially resolved profiles are shown in Figures 2.25 and 2.26; they have slightly reduced S/N ratios, as expected from the decrease in the number of lines; the fit parameters for the central line intensity remain largely the same (cf., Tables 2.2 and 2.3). The line widths shown in Figure 2.27, however, does not increase towards one of the limbs, as in Figure 2.21; the absence of any line broadening could result from the decrease in S/N or that the broadening in the 158 lines profile is the result of blending.

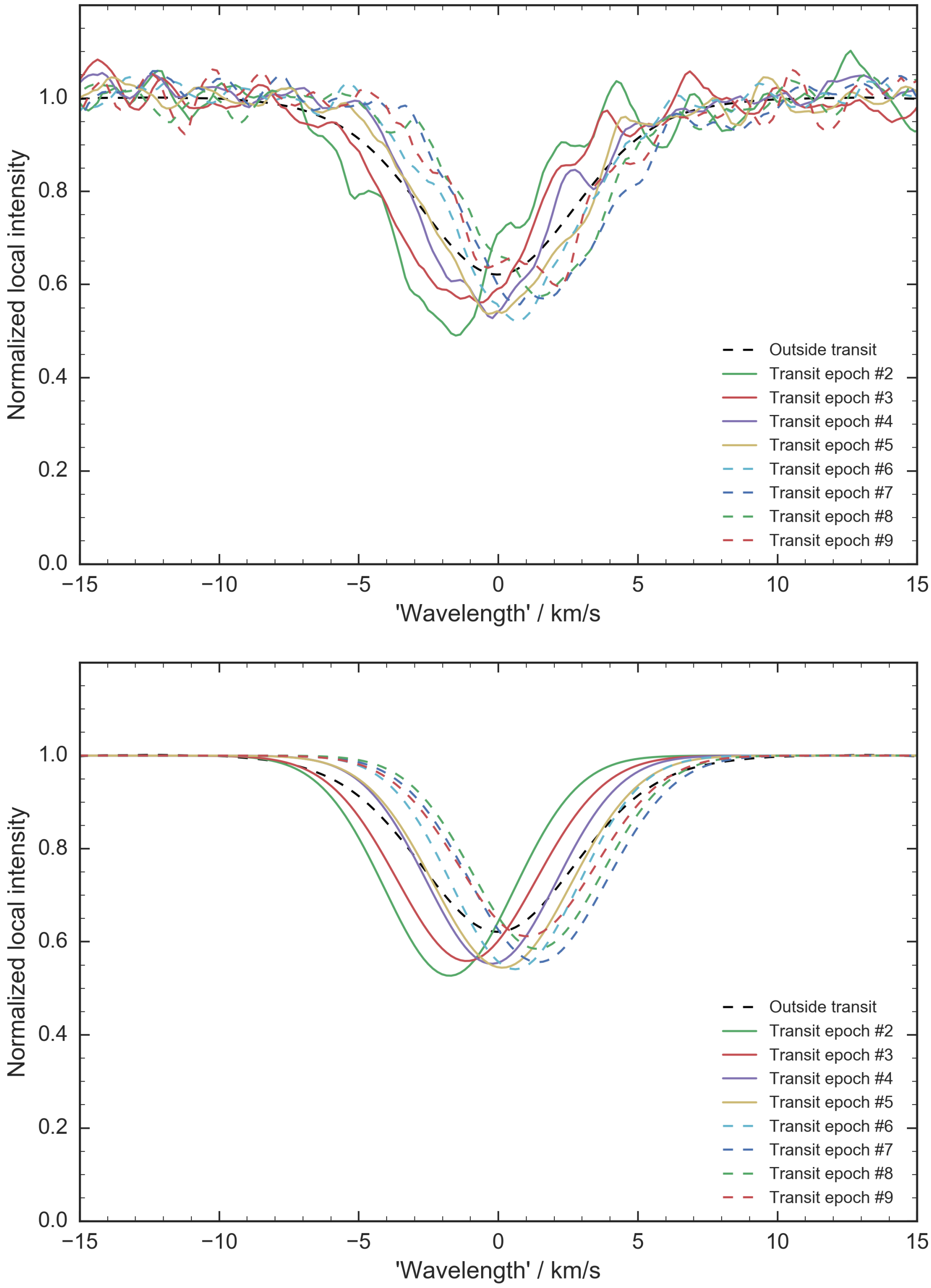

Figure 2.25: Reconstructed line profiles from the spectrum behind the planet for the representative profile obtained from averaging the 74 ‘strictly unblended’ Fe I lines. The top panel shows the reconstructed profiles against the profile outside transit (black dashed curve); the bottom panel their fitted 5 parameter Gaussians. The colors of the solid lines correspond to the transit epochs in Figure 2.8.

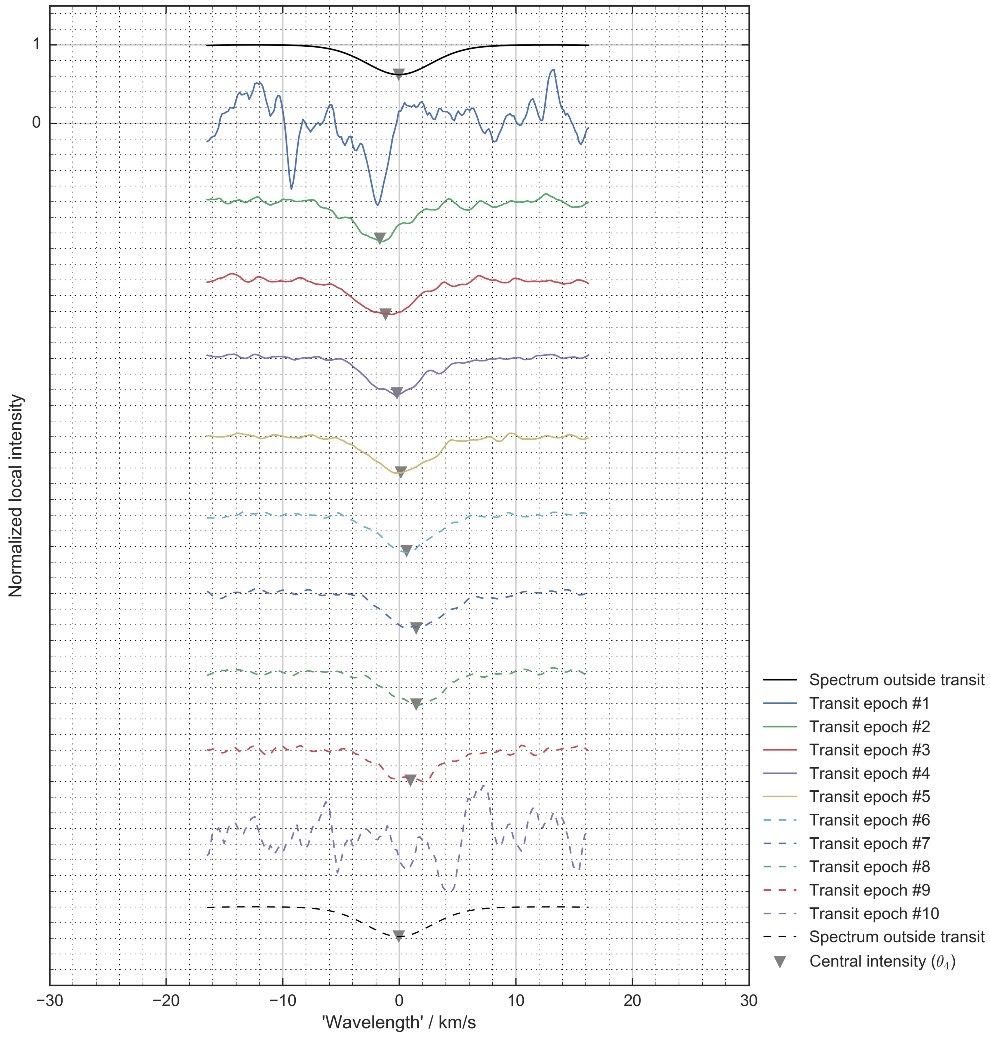

Figure 2.26: The reconstructed profiles for the 'strictly unblended' representative profile shows the same qualitative sequence as for the 158 Fe I lines in Figure 2.20.

Conclusions

The line profile ratios for the representative profile from the subset of 74 'strictly unblended' lines are consistent with those from the profile from 158 Fe I lines, as expected from the similar central line intensity of the two representative profiles. The spatially resolved profiles from the 158 lines show a slight broadening towards one of the limbs (§2.5.1) while the subset of 74 'strictly' unblended profiles do not, which could be due to significantly lower S/N at transit epochs 2 and 9 in the latter case. We cannot rule out that the broadening seen for the representative profile from 158 lines could be due to blending.

We note that a change in the number of lines only slightly affects the S/N; as the S/N $\propto \sqrt{n_{\text{lines}}}$ (Equation (2.2)), it is only slowly increasing with the number of lines, where doubling (halving) the amount of lines increases (decreases) the S/N merely by a factor 1.4 (1/1.4). Thus, to increase the S/N to around 100 for the reconstructed profiles at transit epochs 2 and 9 with the current data and analysis scheme would require increasing the amount of lines by a factor 25, i.e., totaling $74 \cdot 25 = 1\,850$ strictly unblended lines. Observations with higher nominal S/N are likely a better option.

Table 2.3: The obtained parameters from the Gaussian in Equation (2.4)[a] during the different transit epochs for the subset of 74 more strictly unblended Fe I lines. Epoch numbers correspond to those in Figure 2.8. The uncertainties are the formal one standard deviation obtained in the fit.

Transit epoch	A_{eff}[b]	Central intensity (θ_3)	Line center (θ_4)	Width (θ_5)	S/N[c]
Outside transit		0.63 ± 0.001	-0.02 ± 0.010 km/s	4.11 ± 0.014 km/s	4400
#1	0.0023				3
#2	0.0136	0.53 ± 0.010	-1.75 ± 0.054	3.28 ± 0.077	19
#3	0.0227	0.56 ± 0.006	-1.13 ± 0.041	3.51 ± 0.058	31
#4	0.0249	0.55 ± 0.007	-0.24 ± 0.041	3.28 ± 0.058	34
#5	0.0258	0.54 ± 0.005	+0.14 ± 0.031	3.47 ± 0.044	36
#6	0.0257	0.54 ± 0.005	+0.60 ± 0.028	3.20 ± 0.040	35
#7	0.0246	0.56 ± 0.007	+1.43 ± 0.042	3.47 ± 0.060	34
#8	0.0224	0.58 ± 0.006	+1.40 ± 0.037	3.30 ± 0.053	31
#9	0.0139	0.61 ± 0.008	+1.04 ± 0.056	3.47 ± 0.080	19
#10	0.0021				3

---

[a] The continuum and continuum slope parameters are here held fixed at $\theta_1 = 1$ and $\theta_2 = 0$, respectively.
[b] Obtained from Figure 2.16.
[c] Calculated using Equation (2.2) multiplied by A_{eff}.

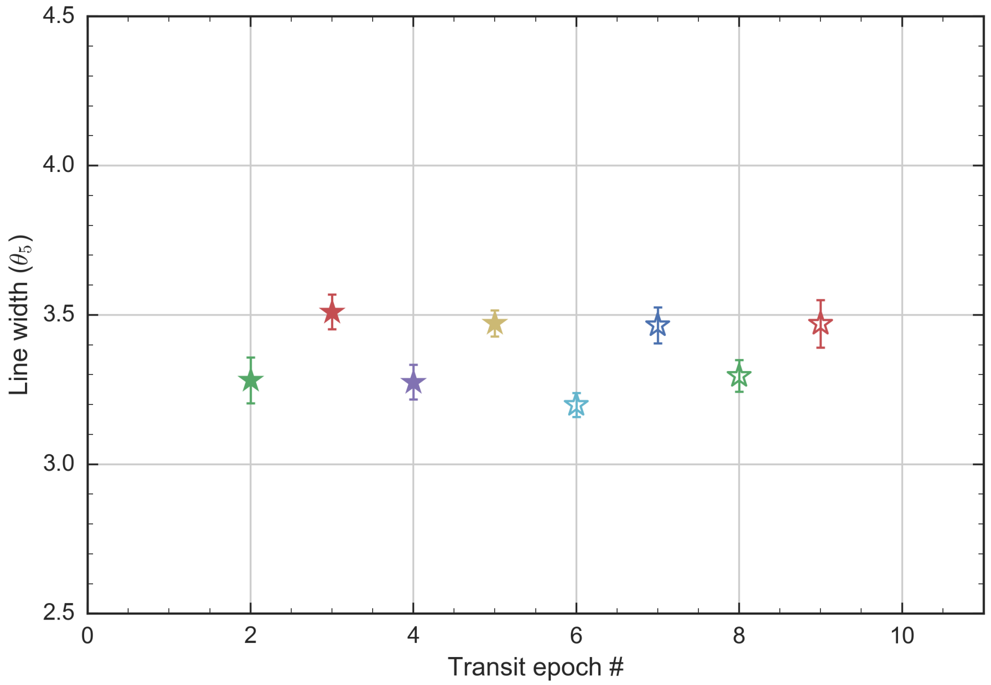

Figure 2.27: The widths of the reconstructed line profile at transit epochs 2–9. Epochs 1 and 10 are omitted as no reliable fits are obtained. The uncertainties are the formal one standard deviation from the fits.

2.6.2 Representative 'strong' and 'weak' line profiles

Above, we have analyzed representative line profiles from lines with unconstrained central line intensities. However, lines are formed at different heights in the stellar atmosphere; stronger lines, i.e., those with a low normalized local intensity at line center, are formed higher in the atmosphere, and weaker lines are formed closer to the continuum. Consequently, any difference in the velocity fields at different heights cannot be discerned if a representative profile is formed from profiles with a broad range of central line intensities. Therefore, in the following, we divide up the 158 Fe I lines into two representative profiles, one comprised of 'strong' and one of 'weak' lines.

We form as 'strong' representative line profile from those in the set of 158 Fe I lines that have central line intensities in the range 0–0.55 in units of normalized local intensity, totaling 72 lines obtaining a central line intensity of 0.41; as 'weak' line profile those with central line intensities 0.55–1, totaling 86 lines obtaining a central line intensity of 0.75. These two representative line profiles are shown in Figures 2.28 and 2.29. We subject these two line profiles to the same analyses as described in §2.3 and §2.5.

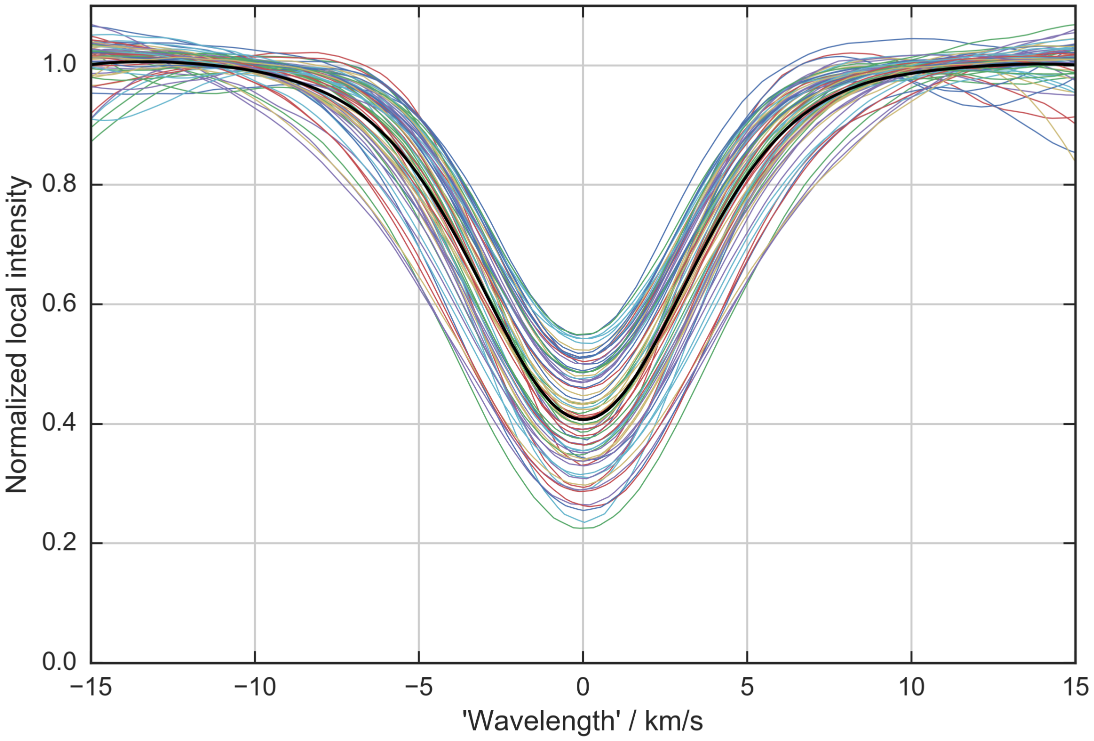

Figure 2.28: The 'strong' line profile formed from a subset of the 158 Fe I lines (Figure 2.5) with central line intensities in the range 0–0.55, totaling 72 lines. Averaging of these lines (colored curves) forms a representative line profile with central line intensity 0.41 shown as the solid black curve.

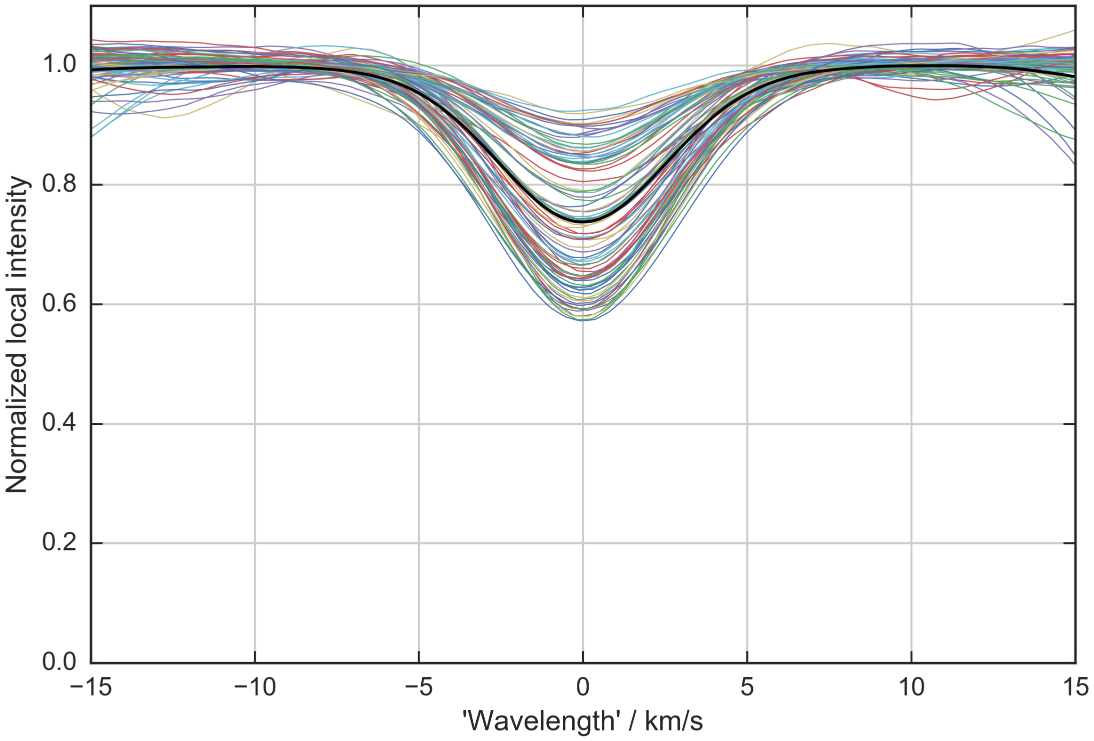

Figure 2.29: The ‘weak’ line profile formed from another subset of the 158 lines with central line intensities in the range 0.55–1, totaling 86 lines. Averaging of these lines (colored curves) forms a representative line profile with central line intensity 0.75, shown as the solid black curve.

Line profile ratios

A comparison between the ‘strong’ and ‘weak’ line profile ratios are shown in Figures 2.30 and 2.31. Both lines show the same sequence as the ratios of the representative profile from 158 Fe I lines in Figure 2.12 do, although less convincingly for the ‘weak’ line as its signal is smaller. Naturally, the amplitudes are larger for the stronger line, as the ratios are sensitive to the gradient of the profile; i.e., a steeper gradient gives a larger ratio, as seen in Figure 1.4. Even though the ‘weak’ line is comprised of more lines than the ‘strong’ one, the latter obtains a ratio amplitude larger by almost one order of magnitude. Stronger line profiles are thus preferred in low S/N situations. We note that the link between gradient and ratio amplitude also means that the calibration of the amplitude-to-wavelength-shift is different for each line strength. For the ‘strong’ and ‘weak’ line, respective amplitudes of about 0.010 and 0.003 both correspond to shifts in ‘wavelength’ of about 0.05 km/s, again consistent with the Rossiter-McLaughlin effect obtained in §2.4.

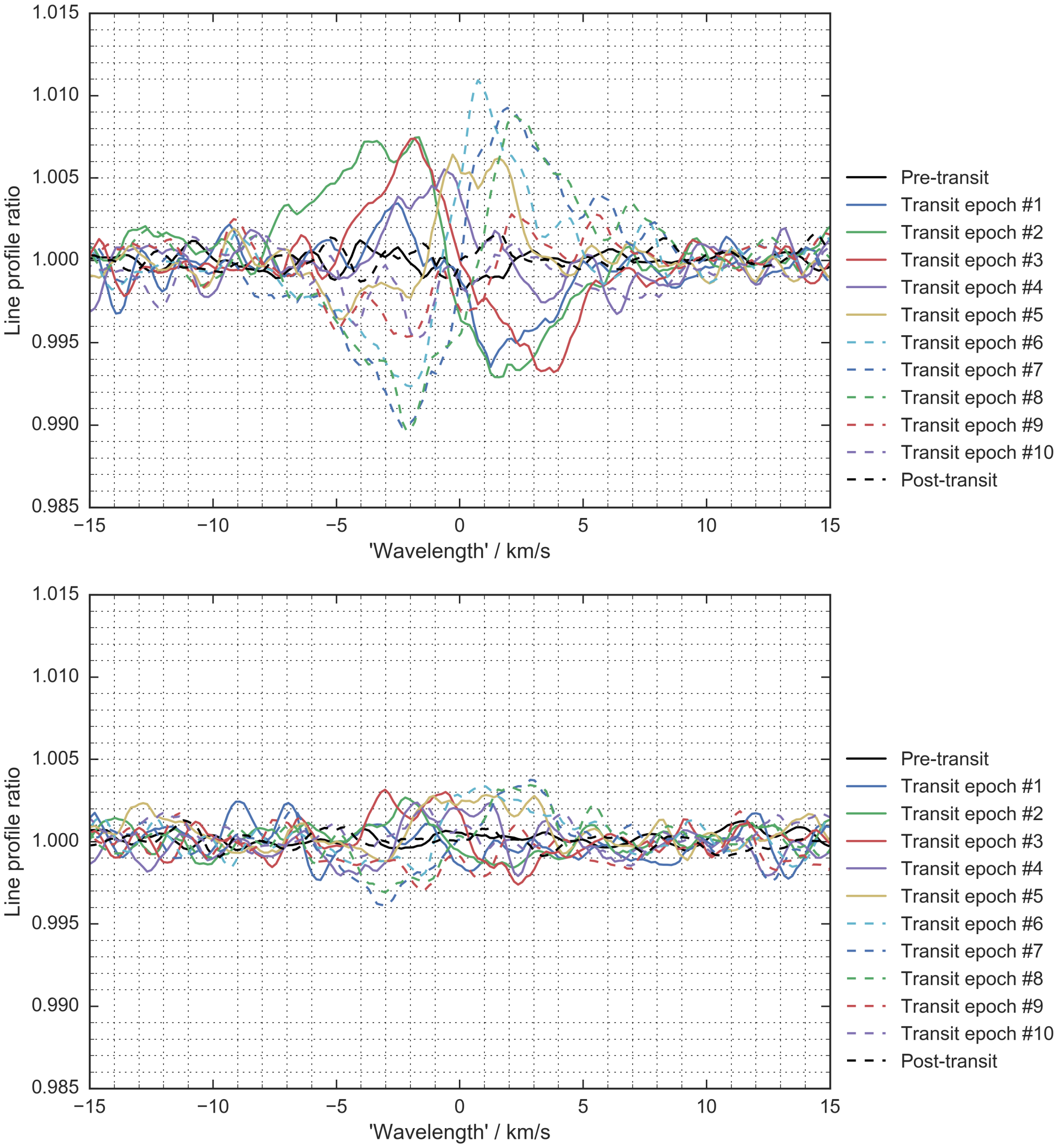

Figure 2.30: A comparison between the line profile ratios for the ‘strong’ (top) and ‘weak’ (bottom) line profiles. The shapes of the ratios in the sequence for both line strengths follow that of the representative profile from 158 Fe I lines (Figure 2.12). Clearly, a stronger line produces a larger amplitude than a weaker one, reflecting that the ratio is sensitive to the gradient of the profile. For the ‘strong’ and ‘weak’ line, respective amplitudes of about 0.010 and 0.003 both correspond to shifts in ‘wavelength’ of 0.05 km/s.

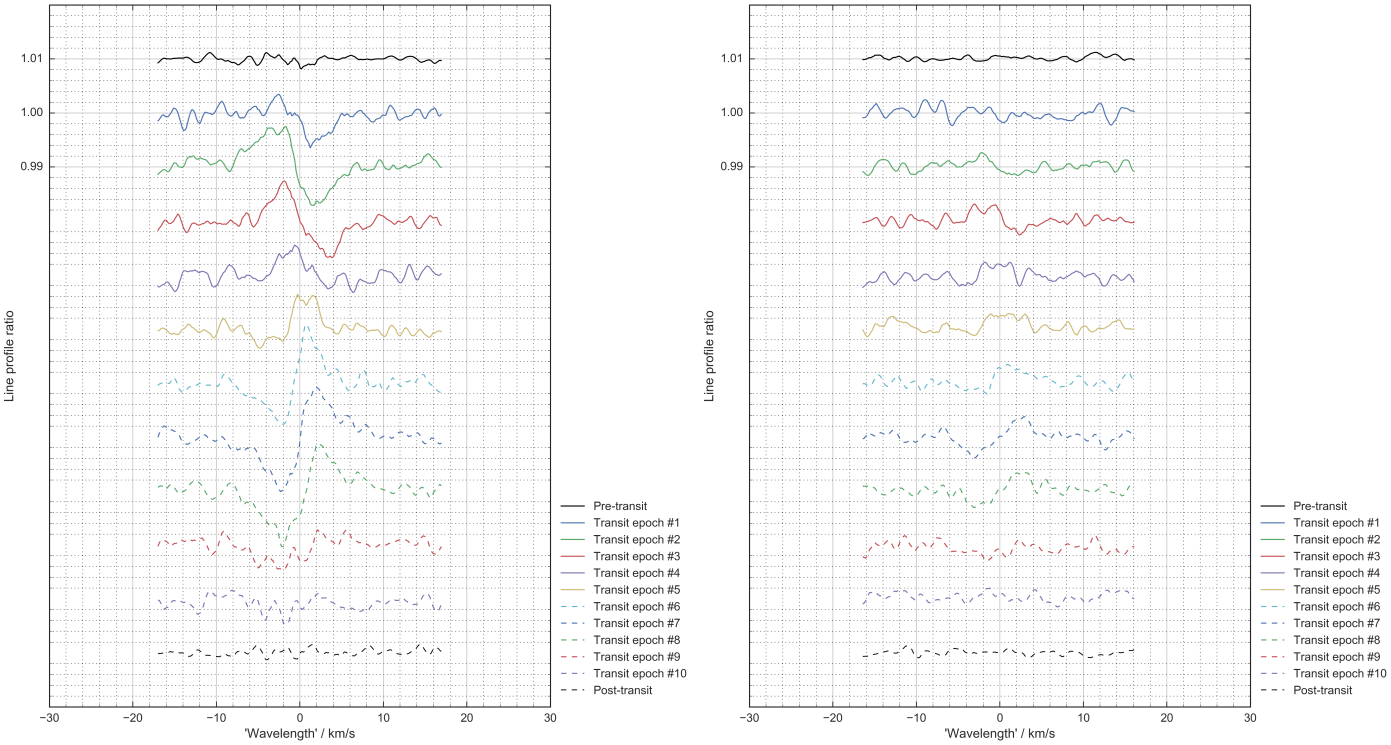

Figure 2.31: A comparison between the sequences of the same line profile ratios for the 'strong' (left) and 'weak' (right) lines as seen in Figure 2.30.

Reconstructed, spatially resolved profiles

The spatially resolved reconstructed line profiles are shown in Figures 2.32 and 2.33. Table 2.4 shows the parameters obtained from the fits. The results have lower S/N than those for the representative profile from the 158 Fe I lines, as expected from the reduced number of lines, but show general qualitative agreement for both the 'strong' and 'weak' line. The line widths at the different transit epochs are shown in Figure 2.34; there is no evidence of broadening towards the limbs for either line.

Conclusions

The representative 'strong' and 'weak' lines show similar qualitative sequences in their line profile ratios. We note that the ratios of the 'strong' line shows a larger amplitude and is thus easier to measure in low S/N situations. No evidence of line broadening towards the limbs is found for either representative line.

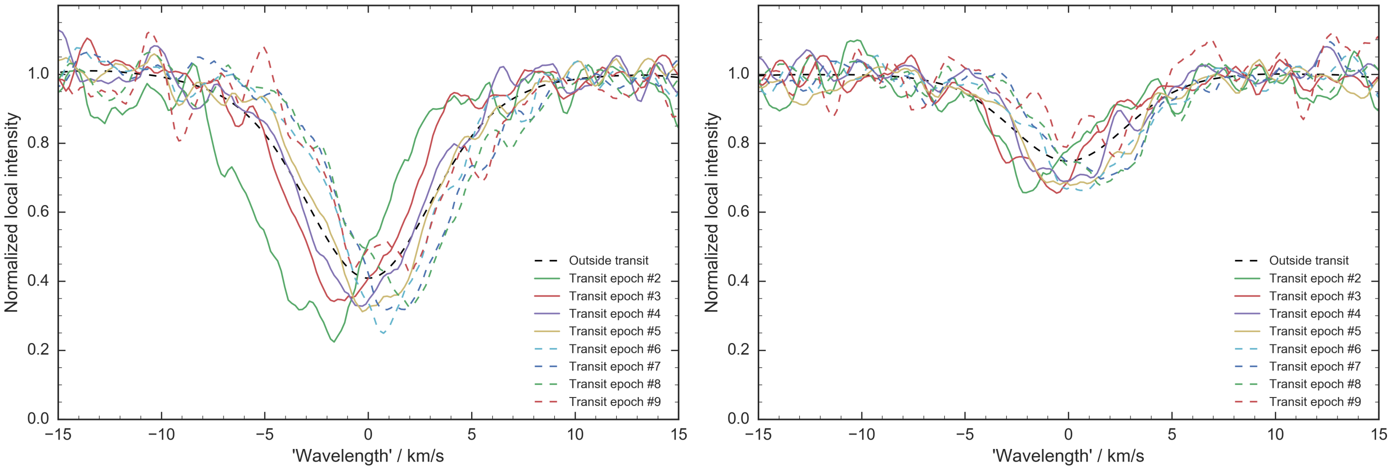

Figure 2.32: Comparison between the reconstructed line profiles for the ‘strong’ (left) and ‘weak’ (right) representative profiles.

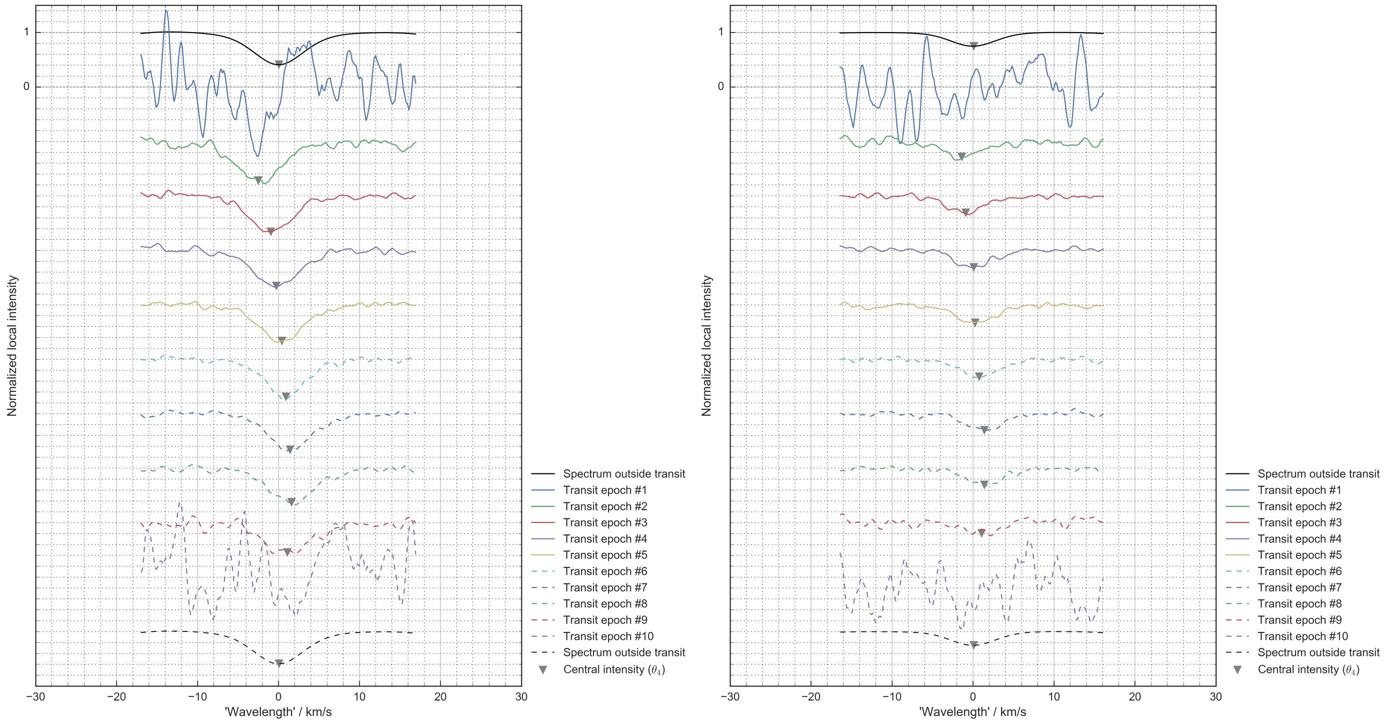

Figure 2.33: Comparison between the sequences of the reconstructed line profiles for the ‘strong’ (left) and ‘weak’ (right) representative profiles shown in Figure 2.32.

Table 2.4: The obtained parameters from the Gaussian in Equation (2.4)[a] during the different transit epochs for the 'strong' and 'weak' lines. Epoch numbers correspond to those in Figure 2.8. The uncertainties are the formal one standard deviation obtained in the fit.

Transit epoch	A_{eff}[b]	Central intensity (θ_3)	Line center (θ_4)	Width (θ_5)	S/N[c]
'Strong' line					
Outside transit		0.42 ± 0.002	+0.03 ± 0.012 km/s	4.61 ± 0.017 km/s	4300
#1	0.0023				3
#2	0.0136	0.28 ± 0.014	-2.37 ± 0.065	4.20 ± 0.091	18
#3	0.0227	0.34 ± 0.008	-0.96 ± 0.036	3.79 ± 0.051	31
#4	0.0249	0.35 ± 0.009	-0.24 ± 0.047	4.07 ± 0.067	34
#5	0.0258	0.34 ± 0.007	+0.35 ± 0.035	4.00 ± 0.049	35
#6	0.0257	0.31 ± 0.008	+0.85 ± 0.036	3.63 ± 0.051	35
#7	0.0246	0.34 ± 0.008	+1.51 ± 0.037	3.96 ± 0.053	33
#8	0.0224	0.38 ± 0.009	+1.69 ± 0.048	4.18 ± 0.068	30
#9	0.0139	0.45 ± 0.014	+1.17 ± 0.088	4.33 ± 0.124	19
#10	0.0021				3
'Weak' line					
Outside transit		0.75 ± 0.001	-0.01 ± 0.012 km/s	4.03 ± 0.017 km/s	4700
#1	0.0023				3
#2	0.0136	0.72 ± 0.012	-1.36 ± 0.125	3.65 ± 0.177	20
#3	0.0227	0.69 ± 0.007	-0.94 ± 0.059	3.30 ± 0.084	34
#4	0.0249	0.69 ± 0.008	+0.05 ± 0.067	3.18 ± 0.094	37
#5	0.0258	0.67 ± 0.007	+0.31 ± 0.064	3.60 ± 0.090	38
#6	0.0257	0.68 ± 0.007	+0.79 ± 0.058	3.48 ± 0.082	38
#7	0.0246	0.70 ± 0.008	+1.35 ± 0.065	3.18 ± 0.092	37
#8	0.0224	0.70 ± 0.007	+1.44 ± 0.064	3.34 ± 0.091	33
#9	0.0139	0.80 ± 0.015	+1.01 ± 0.187	2.94 ± 0.264	21
#10	0.0021				3

---

[a] The continuum and continuum slope parameters are here held fixed at $\theta_1 = 1$ and $\theta_2 = 0$, respectively.

[b] Obtained from Figure 2.16.

[c] Calculated using Equation (2.2) multiplied by A_{eff}.

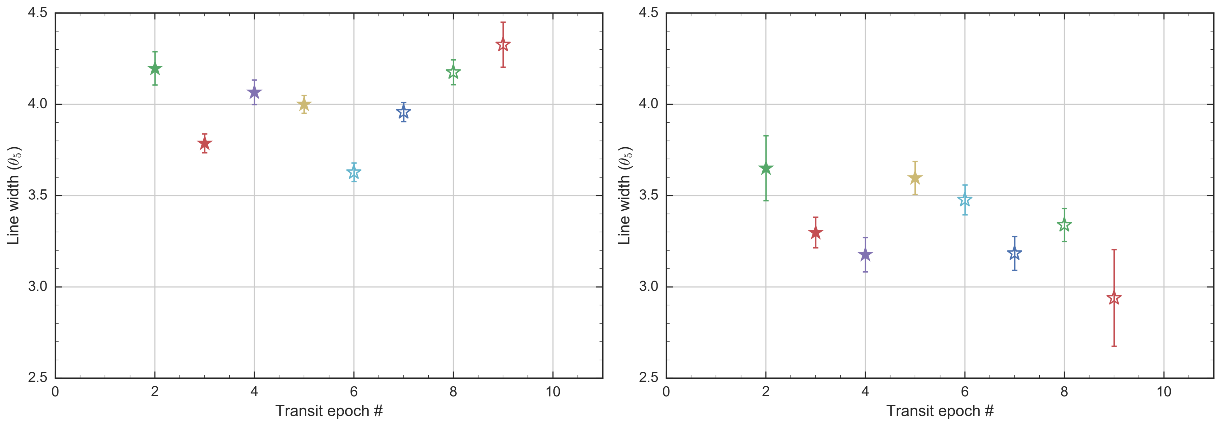

Figure 2.34: Comparison of the widths of the reconstructed line profiles for the 'strong' (left) and 'weak' (right) representative profiles at transit epochs 2–9. Epochs 1 and 10 are omitted as no reliable fits are obtained. The uncertainties are the formal one standard deviation from the fits.

3

Summary and conclusions

Using data from the HARPS spectrograph recorded during exoplanet transits across the cool K-type dwarf star HD 189733A, here called Alopex, we have shown that spatially resolved spectroscopy using exoplanet transits is viable already with current instruments. Although the analyzed HARPS spectra had a S/N of only around 80 per exposure, the deep transit of the planet Alopex b, the averaging of 158 unblended photospheric Fe I lines and the combination of two transit events were used to obtain reconstructed representative profiles across the surface of Alopex with an individual S/N of 30–50.

The spatially resolved profiles are not subject to rotational broadening and are visibly deeper and narrower than the integrated stellar spectrum outside transit. The wavelength shifting of the profiles show a prograde orbit of the planet and a value for the rotation of the star of around 1–2 km/s at the transit latitude, which is consistent with other measurements. Broadening of the spatially resolved profiles towards the limbs reflecting larger horizontal velocity amplitudes is predicted by 3D models but is not confirmed. Broadening only towards one limb is found for the representative profile from 158 Fe I lines, but disappears for the representative profile from a subset of 74 less blended lines. Thus, that the initial broadening is due to blends cannot be ruled out. We note that the limbs are hard to observe with this method as they are substantially limb-darkened and only part of the planet covers the stellar surface. Higher S/N for the reconstructed profiles is likely required to say anything conclusive about line broadening towards the limbs, which is feasibly obtained with future observations with larger telescopes. Furthermore, the resolution $\frac{\Delta\lambda}{\lambda} = 115\,000$ of HARPS is not sufficient to resolve asymmetries in the line profiles.

The amplitude and sequence of the ratios between representative line profiles in-transit and out-of-transit again show a prograde orbit. From these ratios and a line center determination of representative line profiles, the RV shift from the Rossiter-McLaughlin effect can be obtained, although with lower precision than, e.g., cross-correlation of the complete stellar spectrum. Tests of representative profiles with different line strengths show that strong profiles give a larger ratio amplitude and thus a signal that is easier to analyze, even when the weaker one is formed using more spectral lines and thus higher S/N.

We conclude that exoplanet transits enable spatially resolved spectroscopy across stellar surfaces. Line profile shapes, shifts and asymmetries provide sharp diagnostic tools that can be used to test hydrodynamic 3D models of stellar atmospheres. It is just possible to probe stellar surfaces this way using current facilities, but the next generation of telescopes and instruments should enable precise confrontations with models, including measurements of line broadening towards the limbs and asymmetries. The method further gains from bright host stars, and given the favorable exoplanet statistics and several ongoing transit surveys, such targets are plausibly soon discovered. Furthermore, transiting bright systems are high priority for, e.g., exoplanet atmospheres studies and much high-quality data to that end is likely to be collected, which can then also be used to study the atmosphere of the host star.

Bibliography

Agol, E., Cowan, N. B., Knutson, H. A., et al. 2010, ApJ, 721, 1861

Allende Prieto, C., Barklem, P. S., Asplund, M., & Ruiz Cobo, B. 2001, ApJ, 558, 830

Arras, P., & Bildsten, L. 2006, ApJ, 650, 394

Asplund, M. 2005, ARA&A, 43, 481

Asplund, M. 2014, in American Institute of Physics Conference Series, Vol. 1632, American Institute of Physics Conference Series, 58–87

Asplund, M., Grevesse, N., Sauval, A. J., & Scott, P. 2009, ARA&A, 47, 481

Asplund, M., Nordlund, Å., Trampedach, R., Allende Prieto, C., & Stein, R. F. 2000, A&A, 359, 729

Bakos, G. Á., Pál, A., Latham, D. W., Noyes, R. W., & Stefanik, R. P. 2006, ApJ, 641, L57

Boisse, I., Moutou, C., Vidal-Madjar, A., et al. 2009, A&A, 495, 959

Bouchy, F., Udry, S., Mayor, M., et al. 2005, A&A, 444, L15

Boyajian, T., von Braun, K., Feiden, G. A., et al. 2015, MNRAS, 447, 846

del Burgo, C., & Allende Prieto, C. 2016, MNRAS, 463, 1400

Dravins, D. 2008, A&A, 492, 199

Dravins, D., Ludwig, H.-G., Dahlén, E., & Pazira, H. 2016, in 19th Cambridge Workshop on Cool Stars, Stellar Systems, and the Sun (CS19), 66

Dravins, D., Ludwig, H.-G., Dahlén, E., & Pazira, H. 2017, A&A, *submitted*

Freytag, B., Steffen, M., Ludwig, H.-G., et al. 2012, Journal of Computational Physics, 231, 919

Freytag, B., Steffen, M., Wedemeyer-Böhm, S., et al. 2010, CO5BOLD: COnservative COde for the COmputation of COmpressible COnvection in a BOx of L Dimensions with L=2,3, Astrophysics Source Code Library, ascl:1011.014

Galilei, G., Welser, M., & de Filiis, A. 1613, Istoria E dimostrazioni intorno alle macchie solari E loro accidenti comprese in tre lettere scritte all'illvstrissimo signor Marco Velseri ...

Gray, D. F. 2008, The Observation and Analysis of Stellar Photospheres, Cambridge University Press

Gustavsson, M., Dravins, D., & Ludwig, H.-G. 2016, in 19th Cambridge Workshop on Cool Stars, Stellar Systems, and the Sun (CS19), 53

Hinkle, K., Wallace, L., Valenti, J., & Harmer, D. 2000, Visible and Near Infrared Atlas of the Arcturus Spectrum 3727-9300 A

Hunter, A. 1934, MNRAS, 94, 594

Kervella, P., Thévenin, F., Ségransan, D., et al. 2003, A&A, 404, 1087

Linnaeus, C. 1758, Systema naturae, Vol. 1

Magic, Z., Collet, R., Asplund, M., et al. 2013, A&A, 557, A26

Mayor, M., Pepe, F., Queloz, D., et al. 2003, The Messenger, 114, 20

Monnier, J. D., Zhao, M., Pedretti, E., et al. 2007, Science, 317, 342

Nordlund, A., Spruit, H. C., Ludwig, H.-G., & Trampedach, R. 1997, A&A, 328, 229

Nordlund, Å., Stein, R. F., & Asplund, M. 2009, Living Reviews in Solar Physics, 6, 2

Pont, F., Gilliland, R. L., Moutou, C., et al. 2007, A&A, 476, 1347

Ramírez, I., & Allende Prieto, C. 2011, ApJ, 743, 135

Seager, S., & Mallén-Ornelas, G. 2003, ApJ, 585, 1038

Stein, R. F., & Nordlund, Å. 1998, ApJ, 499, 914

Stenflo, J. O., & Lindegren, L. 1977, A&A, 59, 367

Torres, G., Fischer, D. A., Sozzetti, A., et al. 2012, ApJ, 757, 161

Torres, G., Winn, J. N., & Holman, M. J. 2008, ApJ, 677, 1324

Tremblay, P.-E., Ludwig, H.-G., Freytag, B., Steffen, M., & Caffau, E. 2013, A&A, 557, A7

Triaud, A. H. M. J., Queloz, D., Bouchy, F., et al. 2009, A&A, 506, 377

Uitenbroek, H., Dupree, A. K., & Gilliland, R. L. 1998, AJ, 116, 2501

Winn, J. N. 2011, in IAU Symposium, Vol. 276, The Astrophysics of Planetary Systems: Formation, Structure, and Dynamical Evolution, ed. A. Sozzetti, M. G. Lattanzi, & A. P. Boss, 230–237

Winn, J. N., Johnson, J. A., Marcy, G. W., et al. 2006, ApJ, 653, L69

A

Atlas of the Alopex spectrum

Below is an atlas of the visible part of the spectrum of the K1V star HD 189733A, or Alopex. The atlas is compiled using the data from one HARPS observation run and shows the averaged spectrum from 40 exposures (program ID 079.C-0127(A)).

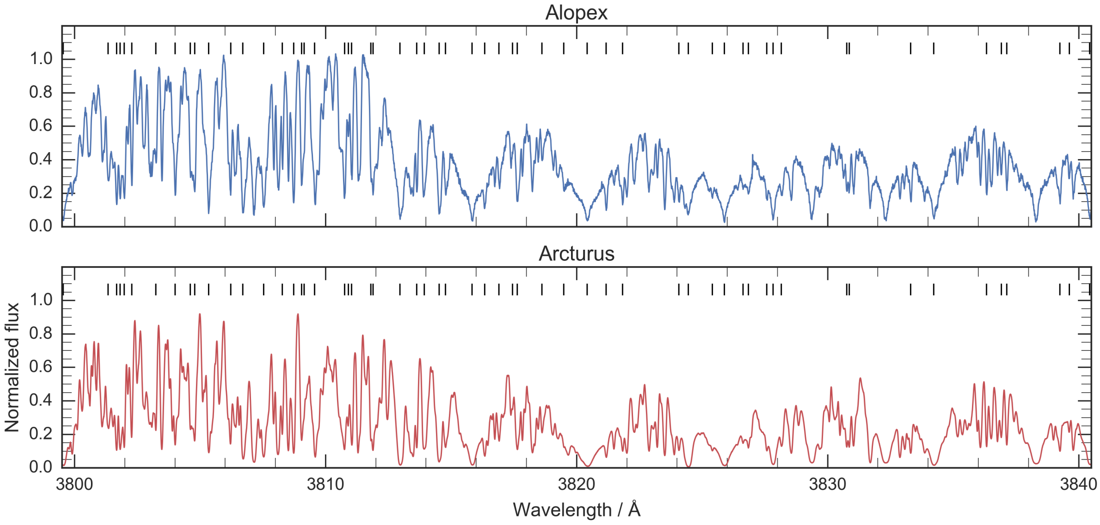

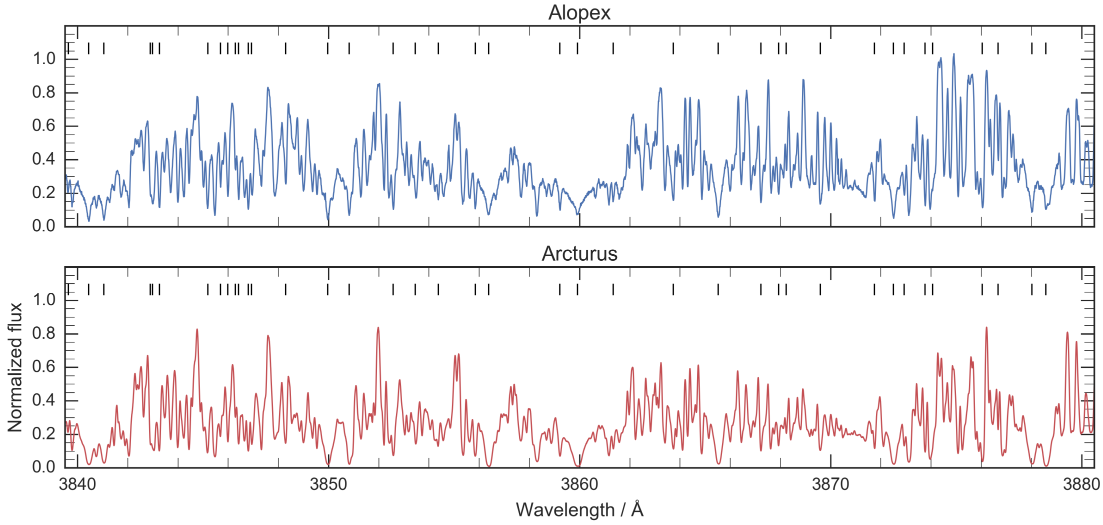
Alopex
Arcturus
Normalized flux
0.0
0.2
0.4
0.6
0.8
1.0
3840
3850
3860
3870
3880
Wavelength / Å

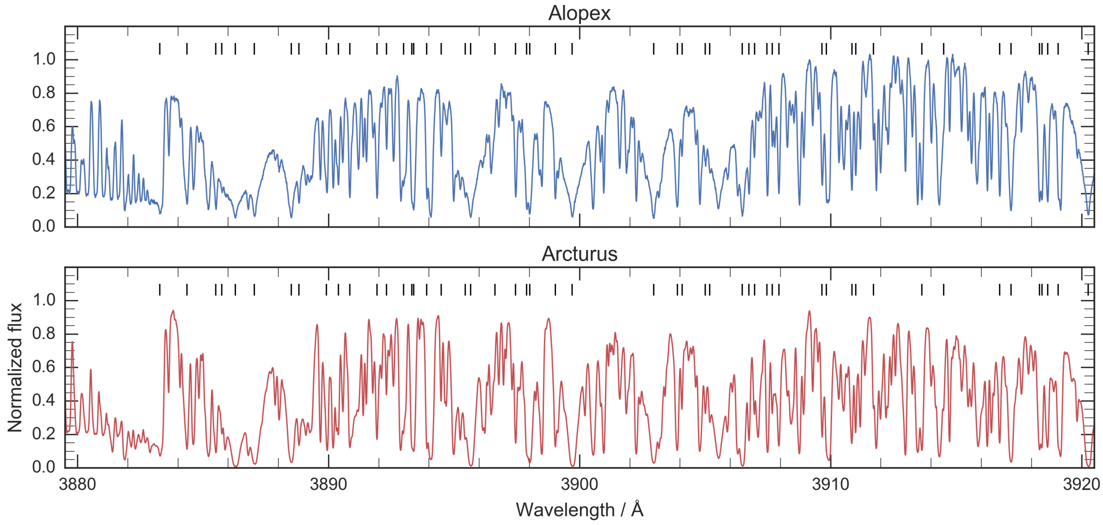
Alopex
Arcturus
Normalized flux
0.0
0.2
0.4
0.6
0.8
1.0
3880
3890
3900
3910
3920
Wavelength / Å

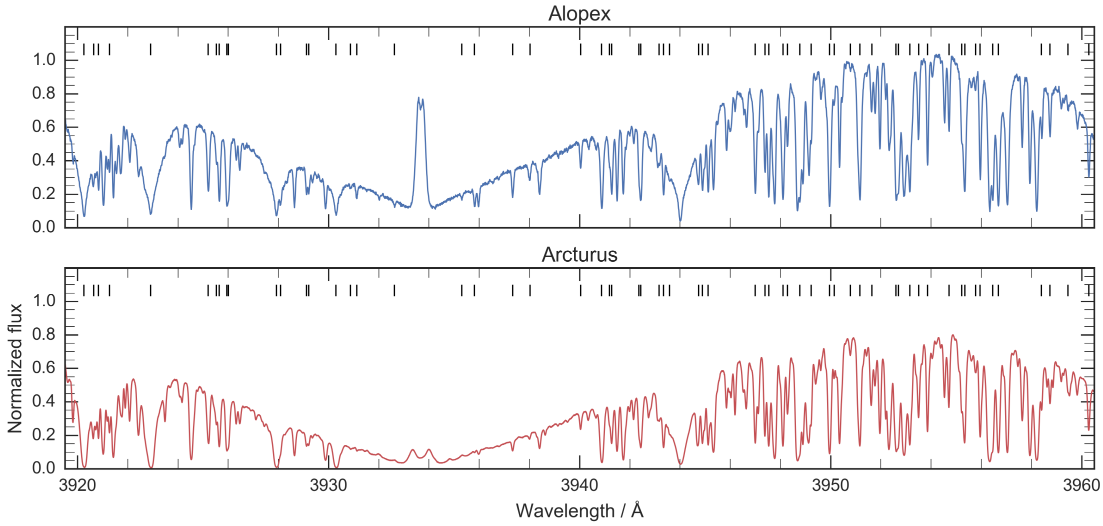
Alopex
Arcturus
Normalized flux
0.0
0.2
0.4
0.6
0.8
1.0
3920
3930
3940
3950
3960
Wavelength / Å

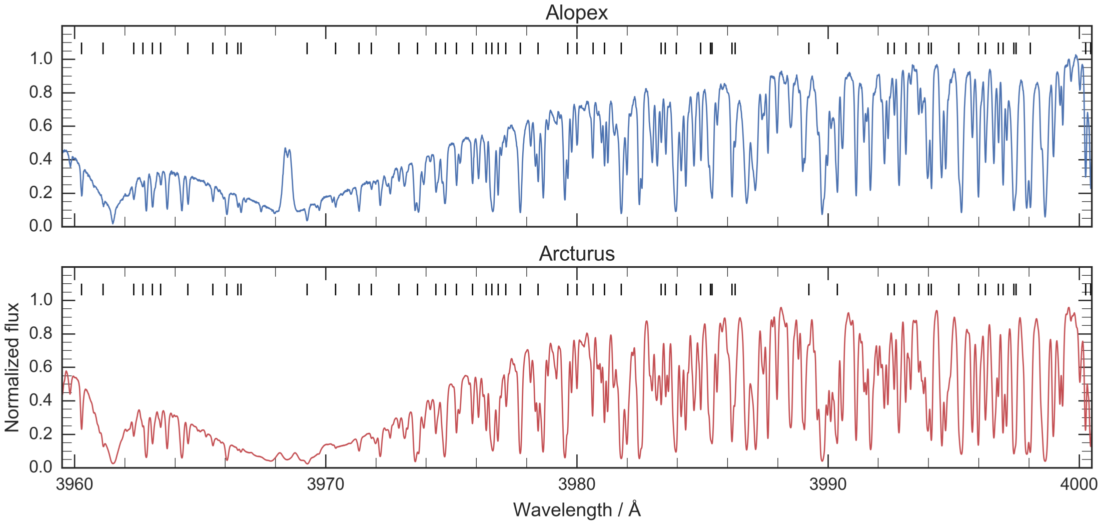
Alopex
Arcturus
Normalized flux
0.0
0.2
0.4
0.6
0.8
1.0
3960
3970
3980
3990
4000
Wavelength / Å

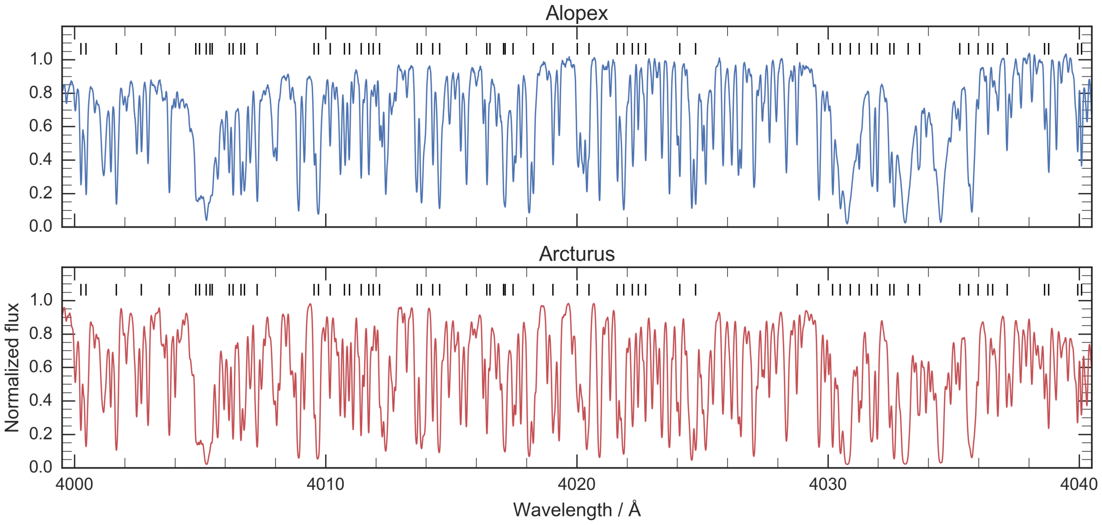
Alopex
Arcturus
Normalized flux
0.0
0.2
0.4
0.6
0.8
1.0
4000
4010
4020
4030
4040
Wavelength / Å

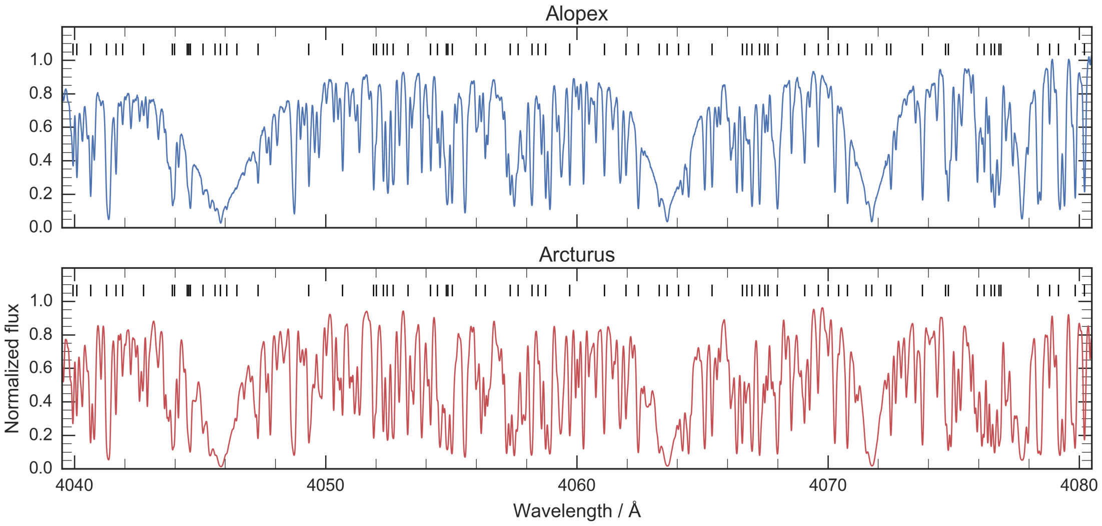
Alopex
Arcturus
Normalized flux
0.0
0.2
0.4
0.6
0.8
1.0
4040
4050
4060
4070
4080
Wavelength / Å

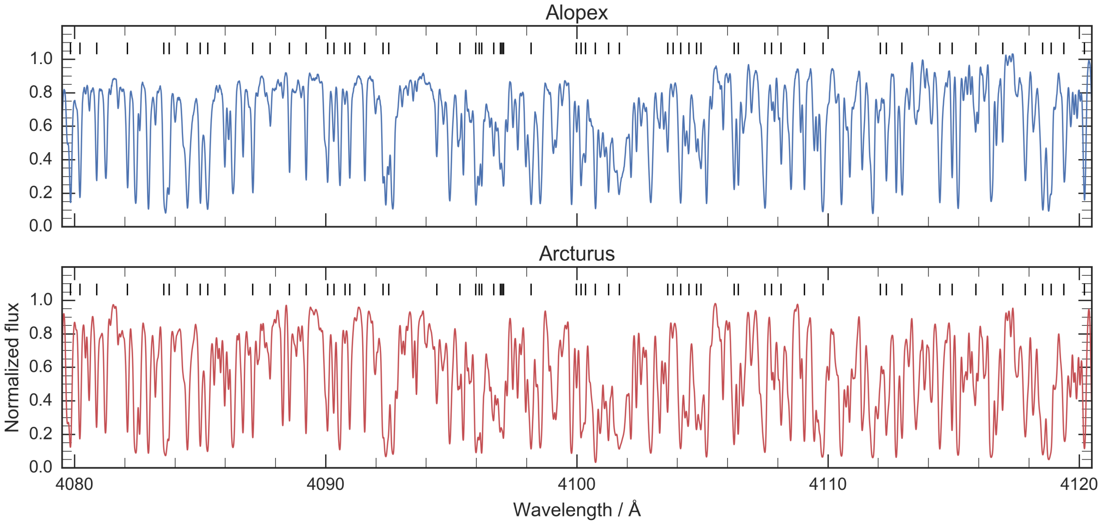
Alopex
Arcturus
Normalized flux
0.0
0.2
0.4
0.6
0.8
1.0
4080
4090
4100
4110
4120
Wavelength / Å

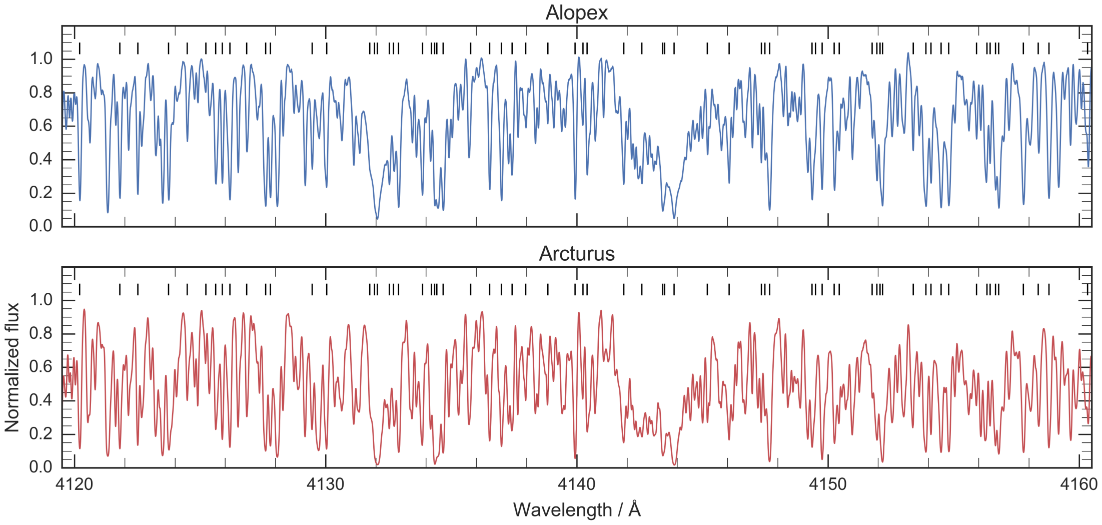
Alopex
Arcturus
Normalized flux
0.0
0.2
0.4
0.6
0.8
1.0
4120
4130
4140
4150
4160
Wavelength / Å

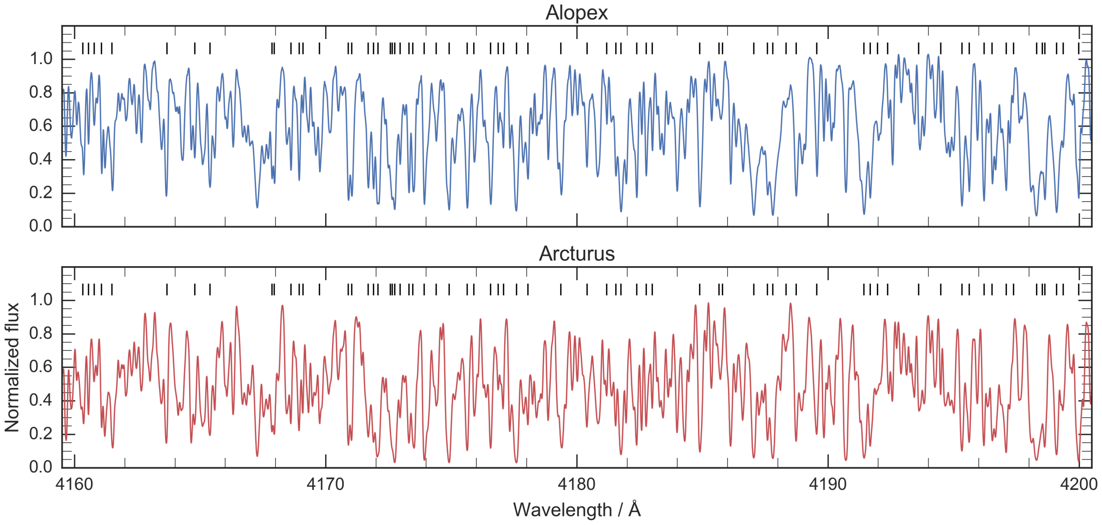
Alopex
Arcturus
Normalized flux
0.0
0.2
0.4
0.6
0.8
1.0
4160
4170
4180
4190
4200
Wavelength / Å

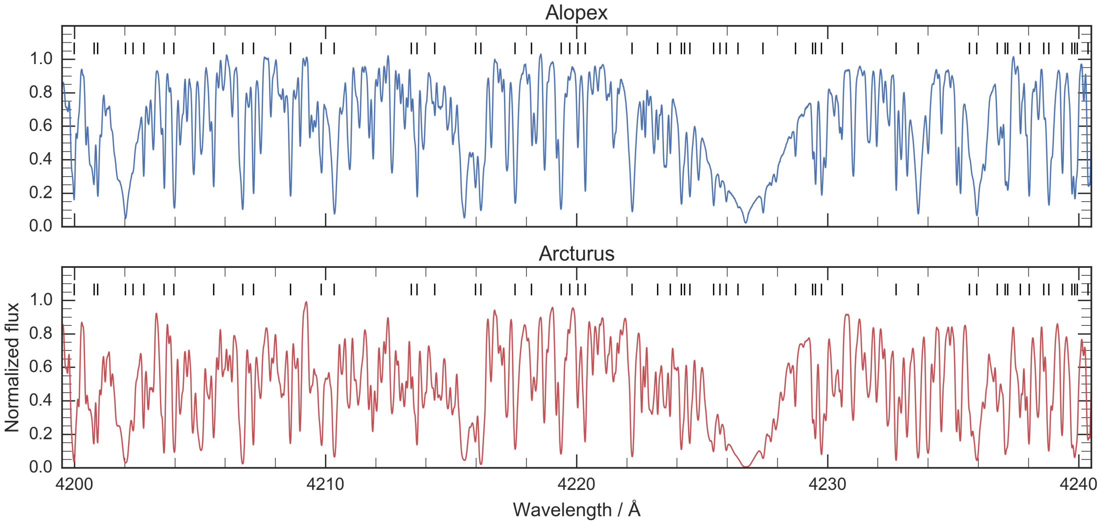
Alopex
Arcturus
Normalized flux
0.0
0.2
0.4
0.6
0.8
1.0
4200
4210
4220
4230
4240
Wavelength / Å

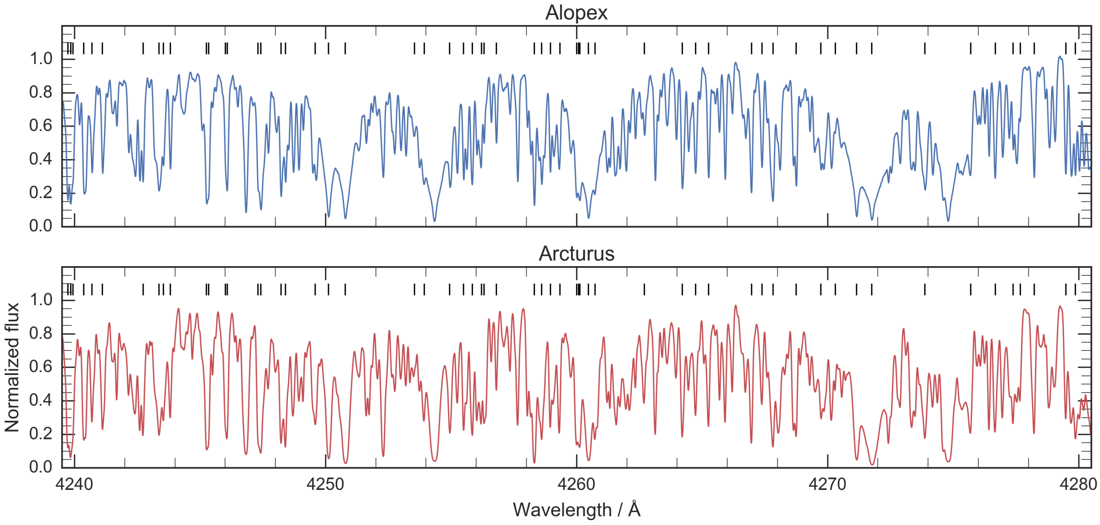
Alopex
Arcturus
Normalized flux
0.0
0.2
0.4
0.6
0.8
1.0
4240
4250
4260
4270
4280
Wavelength / Å

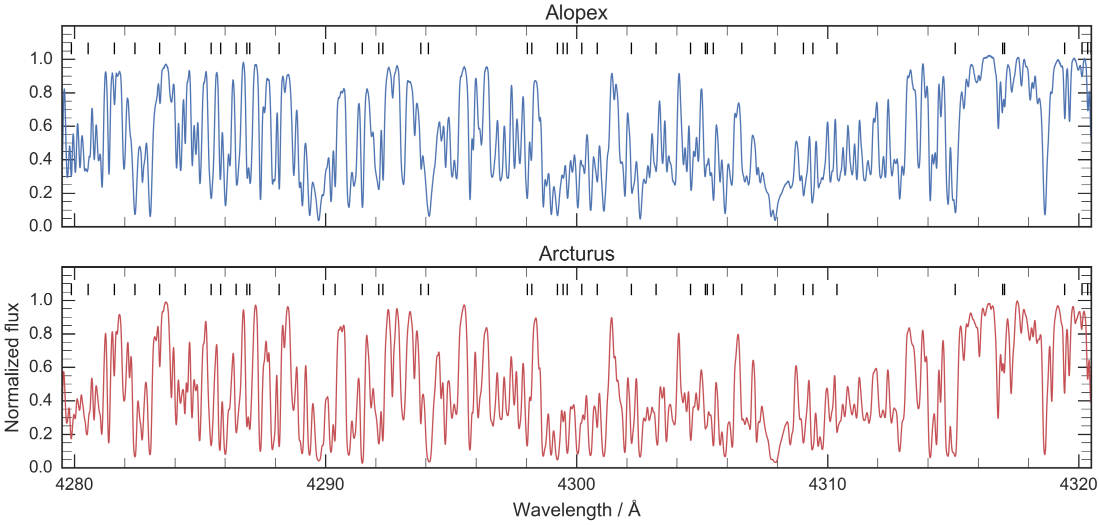
Alopex
Arcturus
Normalized flux
0.0
0.2
0.4
0.6
0.8
1.0
4280
4290
4300
4310
4320
Wavelength / Å

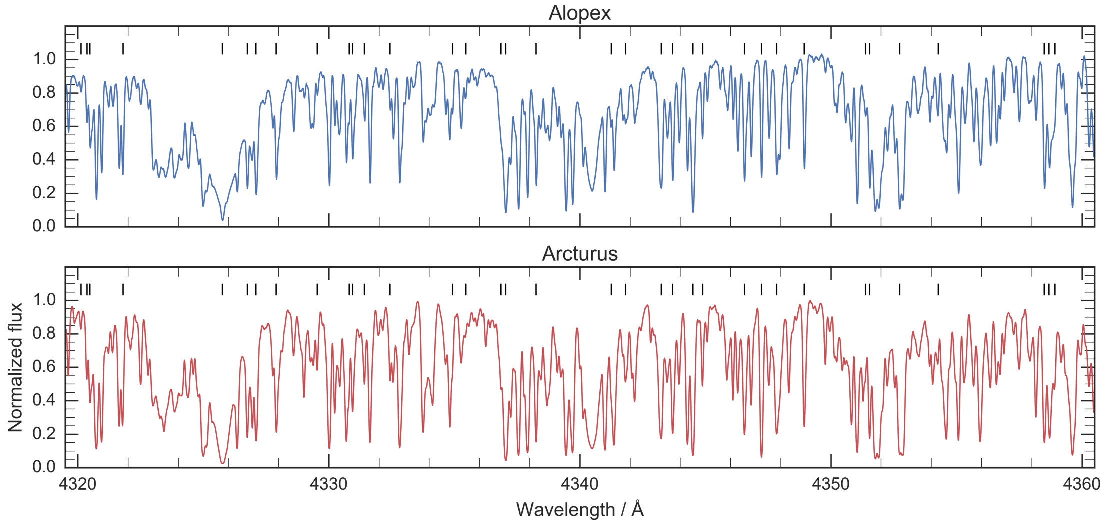
Alopex
Arcturus
Normalized flux
0.0
0.2
0.4
0.6
0.8
1.0
4320
4330
4340
4350
4360
Wavelength / Å

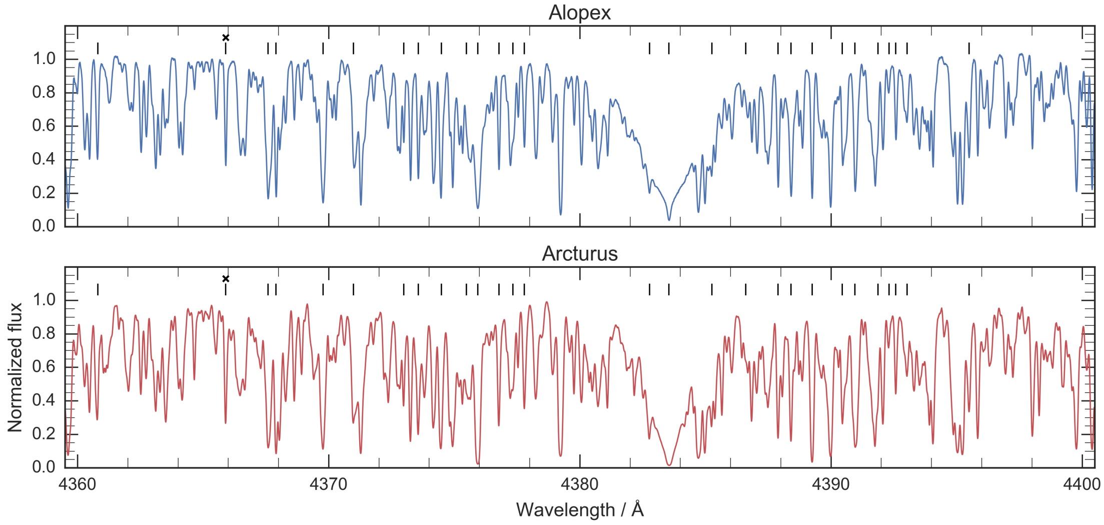
Alopex
Arcturus
×
Normalized flux
0.0
0.2
0.4
0.6
0.8
1.0
4360
4370
4380
4390
4400
Wavelength / Å

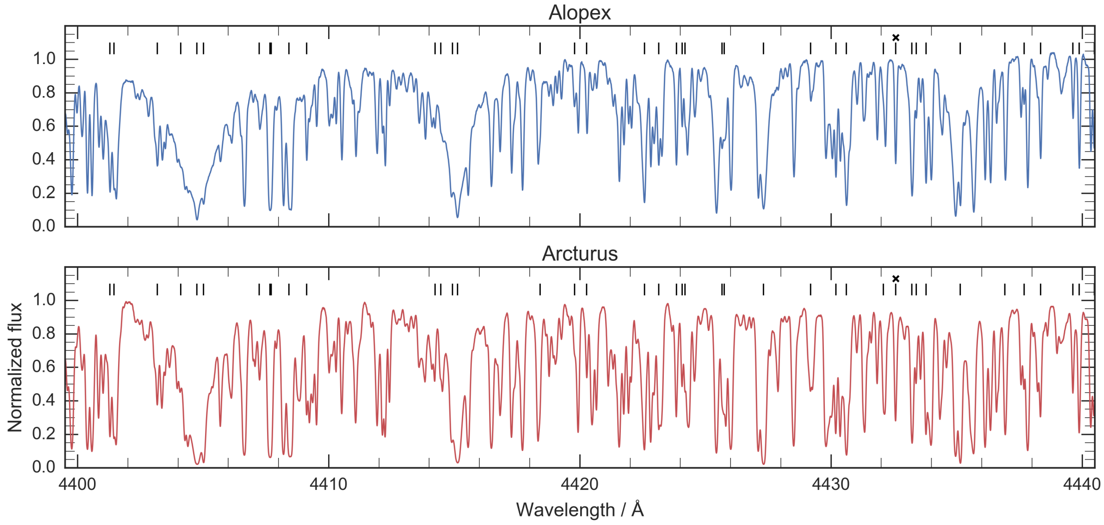
Alopex
Arcturus
×
Normalized flux
0.0
0.2
0.4
0.6
0.8
1.0
4400
4410
4420
4430
4440
Wavelength / Å

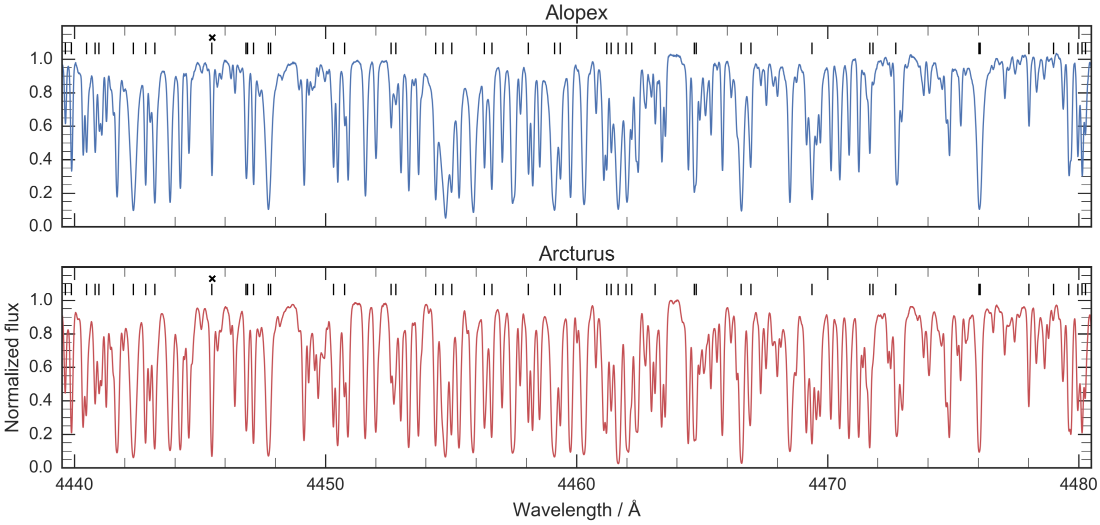
Alopex
Arcturus
Normalized flux
0.0
0.2
0.4
0.6
0.8
1.0
4440
4450
4460
4470
4480
Wavelength / Å

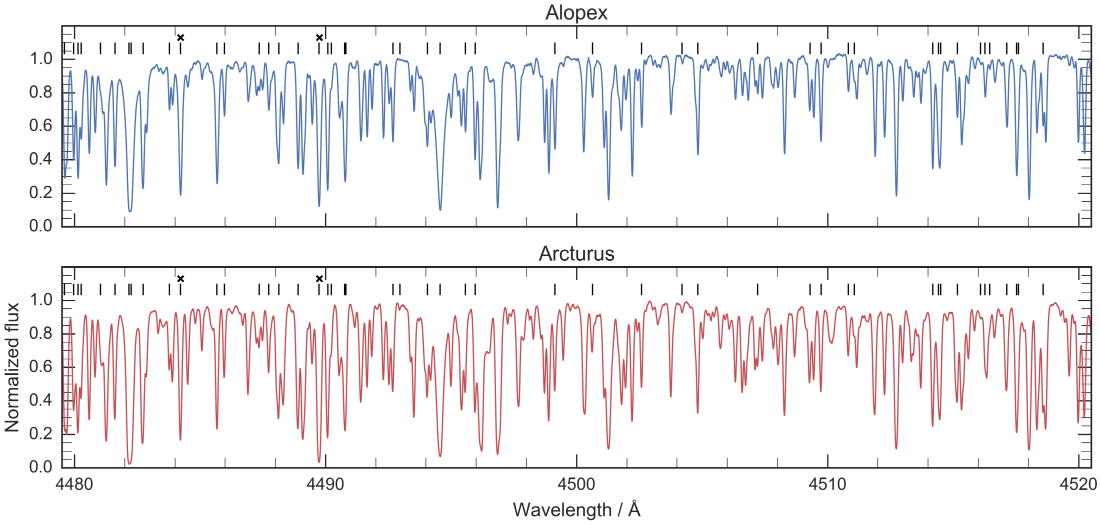
Alopex
Arcturus
Normalized flux
0.0
0.2
0.4
0.6
0.8
1.0
4480
4490
4500
4510
4520
Wavelength / Å

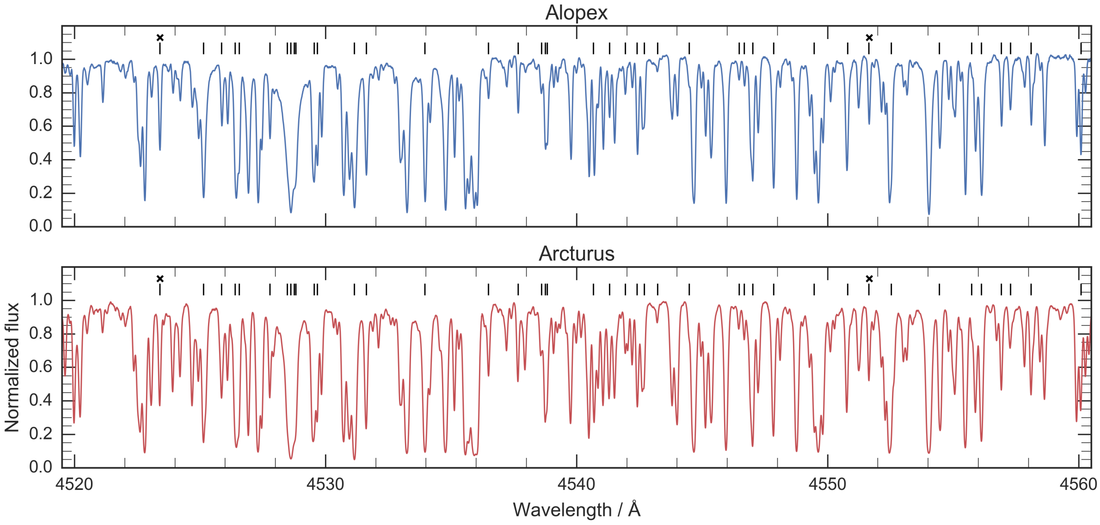
Alopex
Arcturus
Normalized flux
0.0
0.2
0.4
0.6
0.8
1.0
4520
4530
4540
4550
4560
Wavelength / Å

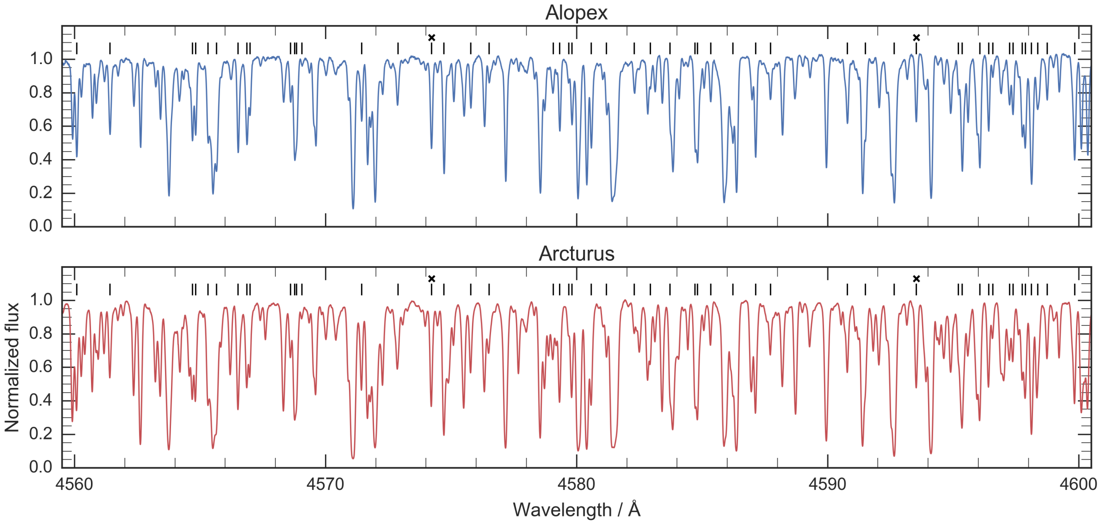
Alopex
Arcturus
Normalized flux
0.0
0.2
0.4
0.6
0.8
1.0
4560
4570
4580
4590
4600
Wavelength / Å

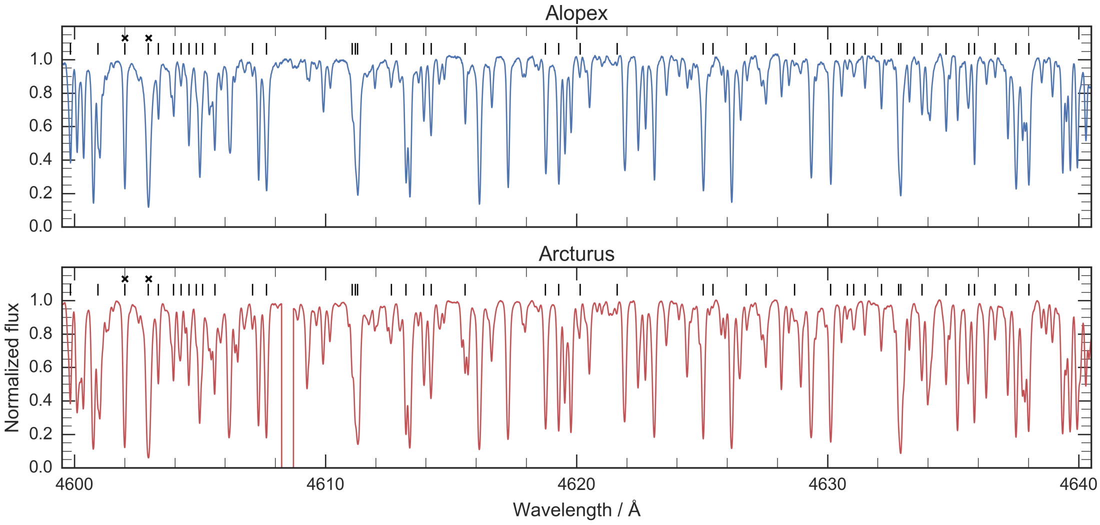
Alopex
Arcturus
Normalized flux
0.0
0.2
0.4
0.6
0.8
1.0
4600
4610
4620
4630
4640
Wavelength / Å

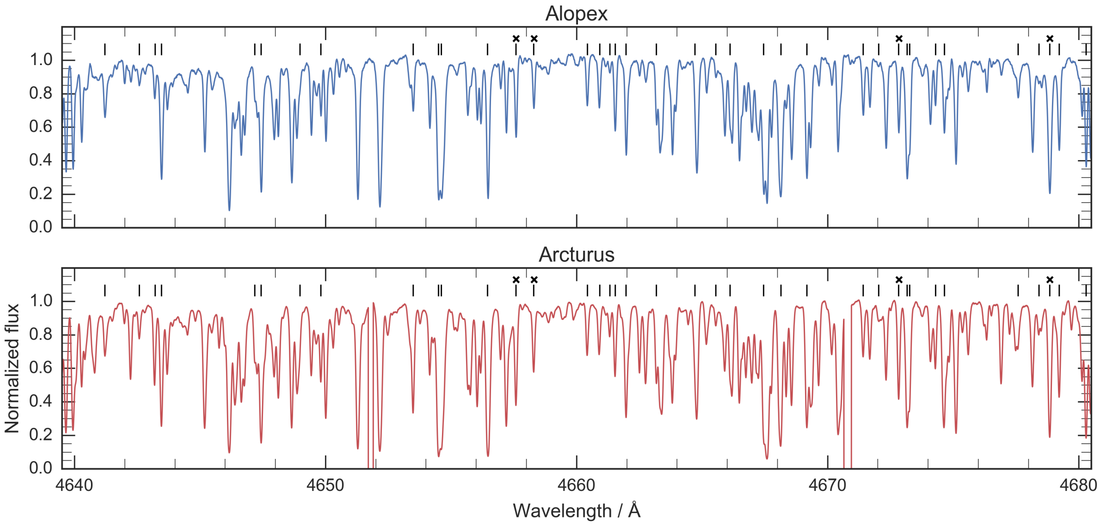
Alopex
Arcturus
Normalized flux
0.0
0.2
0.4
0.6
0.8
1.0
4640
4650
4660
4670
4680
Wavelength / Å

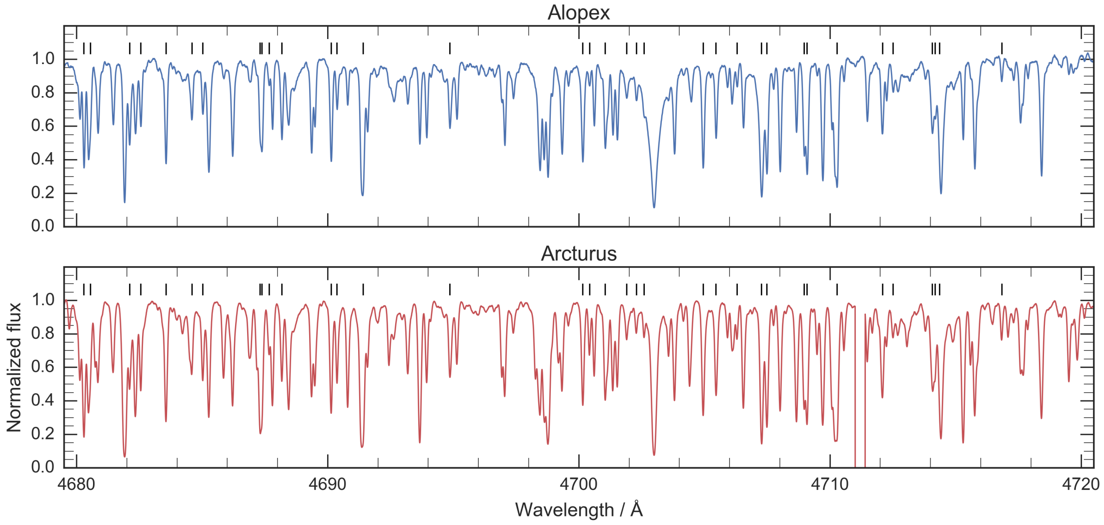
Alopex
Arcturus
Normalized flux
0.0
0.2
0.4
0.6
0.8
1.0
4680
4690
4700
4710
4720
Wavelength / Å

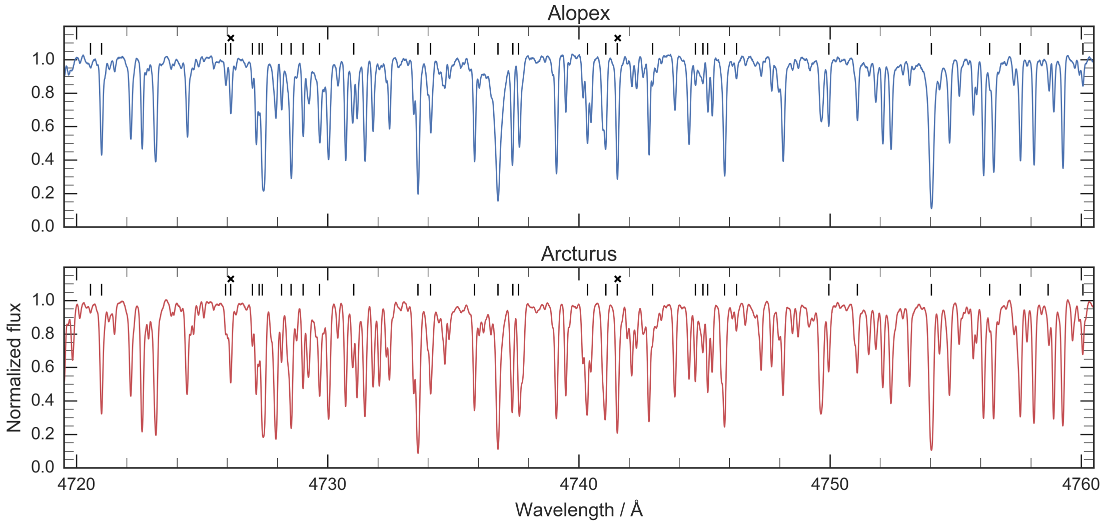
Alopex
Arcturus
Normalized flux
0.0
0.2
0.4
0.6
0.8
1.0
4720
4730
4740
4750
4760
Wavelength / Å

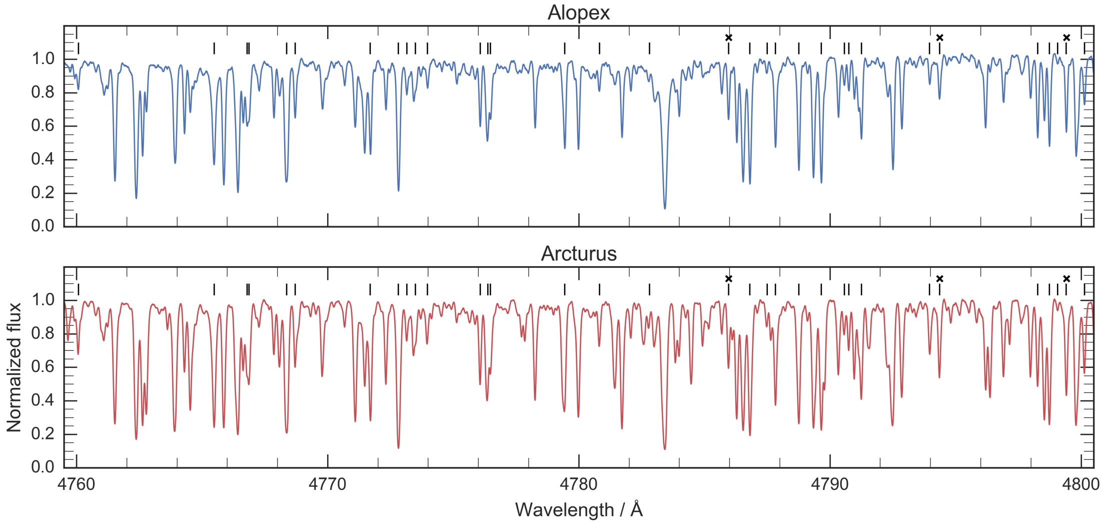
Alopex
Arcturus
Normalized flux
0.0
0.2
0.4
0.6
0.8
1.0
4760
4770
4780
4790
4800
Wavelength / Å

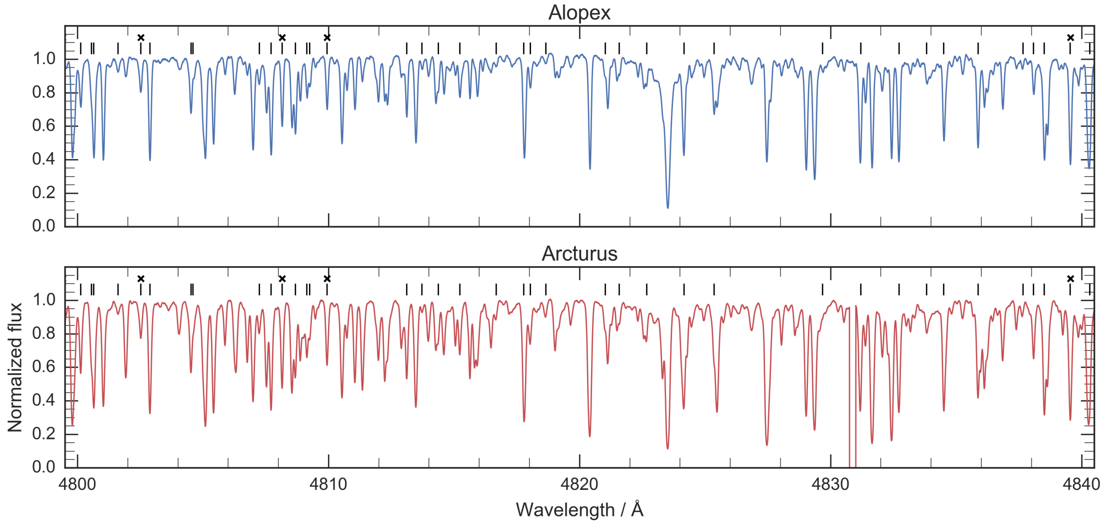
Alopex
Arcturus
Normalized flux
0.0
0.2
0.4
0.6
0.8
1.0
4800
4810
4820
4830
4840
Wavelength / Å

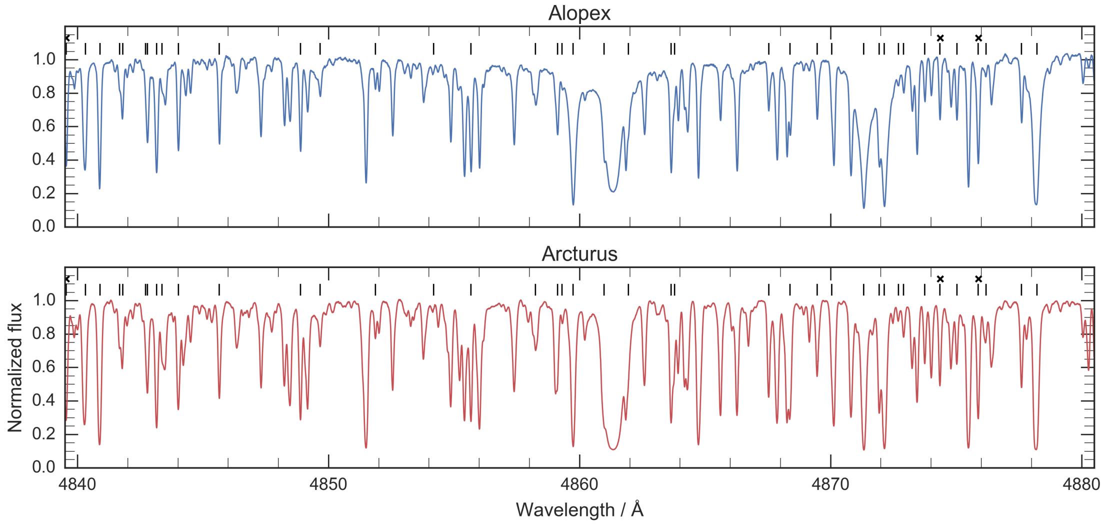
Alopex
Arcturus
Normalized flux
0.0
0.2
0.4
0.6
0.8
1.0
4840
4850
4860
4870
4880
Wavelength / Å

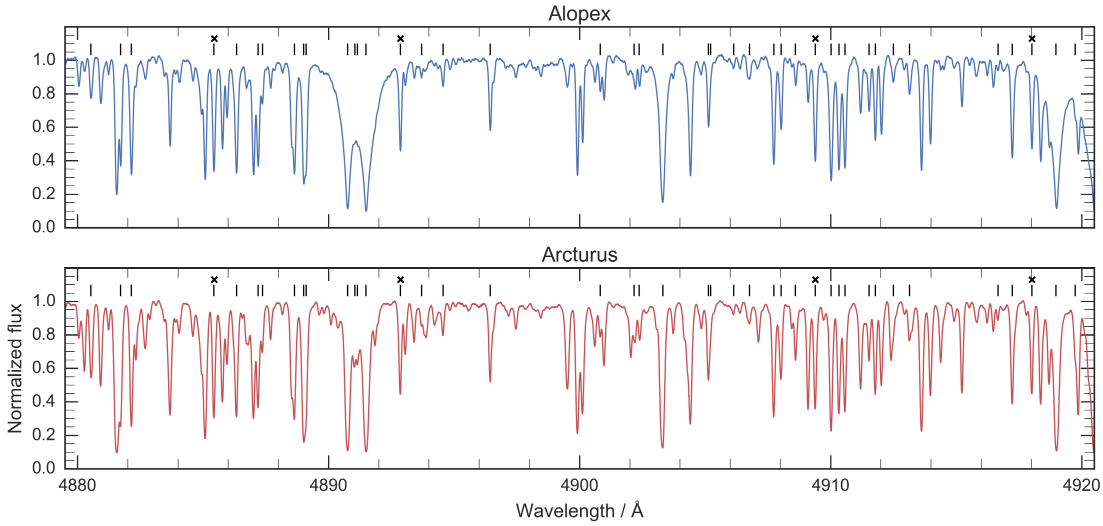
Alopex
Arcturus
Normalized flux
0.0
0.2
0.4
0.6
0.8
1.0
4880
4890
4900
4910
4920
Wavelength / Å

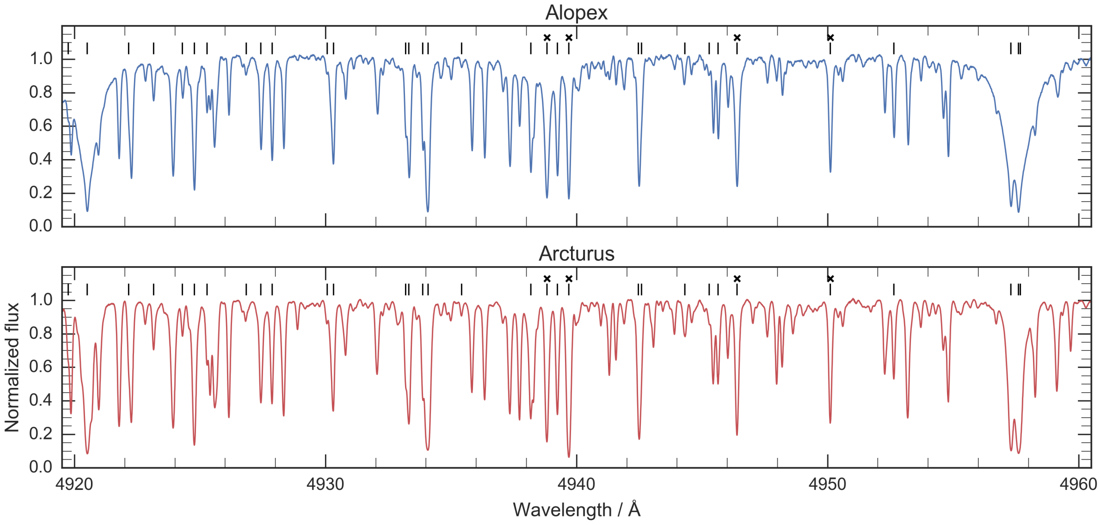
Alopex
Arcturus
Normalized flux
0.0
0.2
0.4
0.6
0.8
1.0
4920
4930
4940
4950
4960
Wavelength / Å

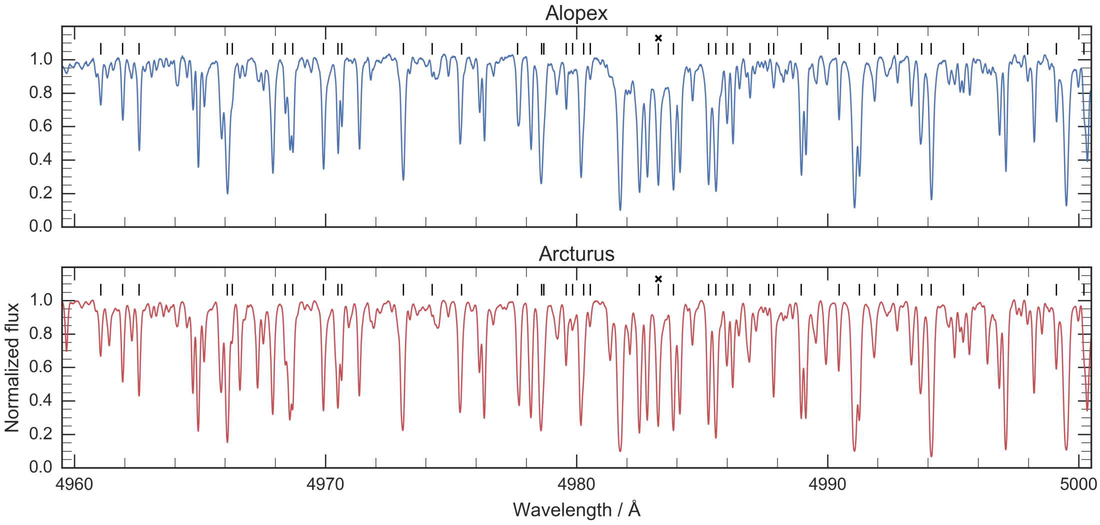
Alopex
Arcturus
Normalized flux
0.0
0.2
0.4
0.6
0.8
1.0
4960
4970
4980
4990
5000
Wavelength / Å

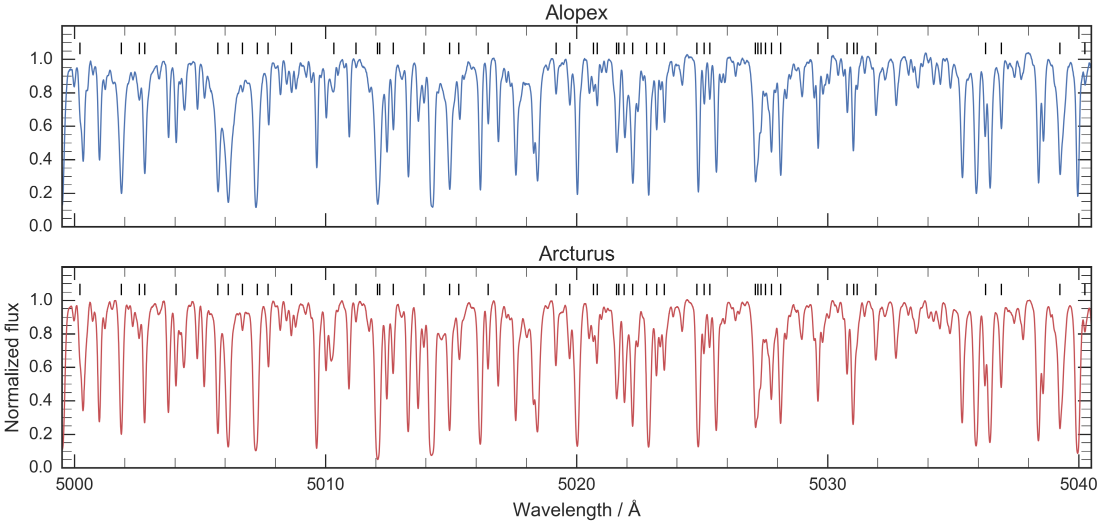
Alopex
Arcturus
Normalized flux
0.0
0.2
0.4
0.6
0.8
1.0
5000
5010
5020
5030
5040
Wavelength / Å

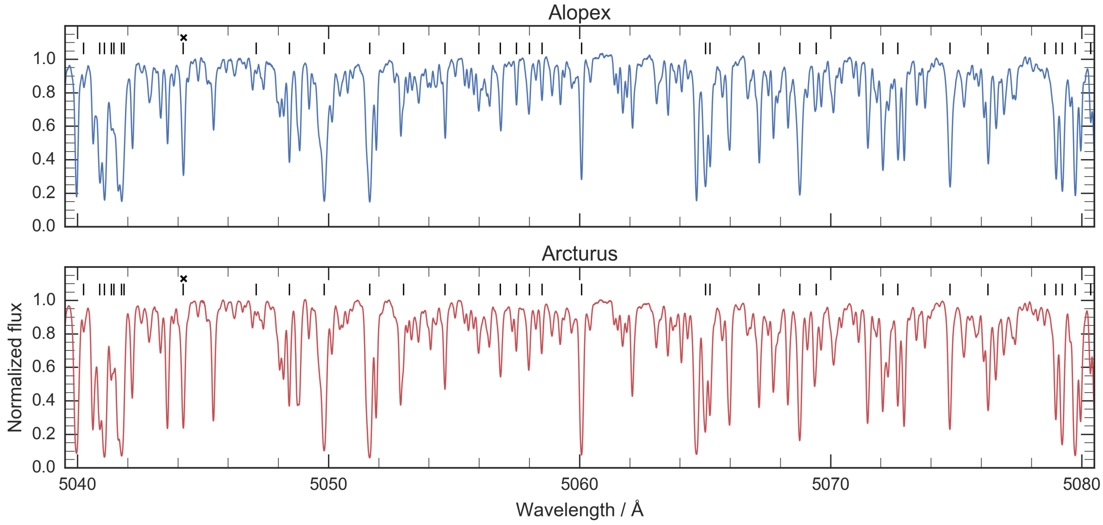
Alopex
Arcturus
Normalized flux
0.0
0.2
0.4
0.6
0.8
1.0
5040
5050
5060
5070
5080
Wavelength / Å

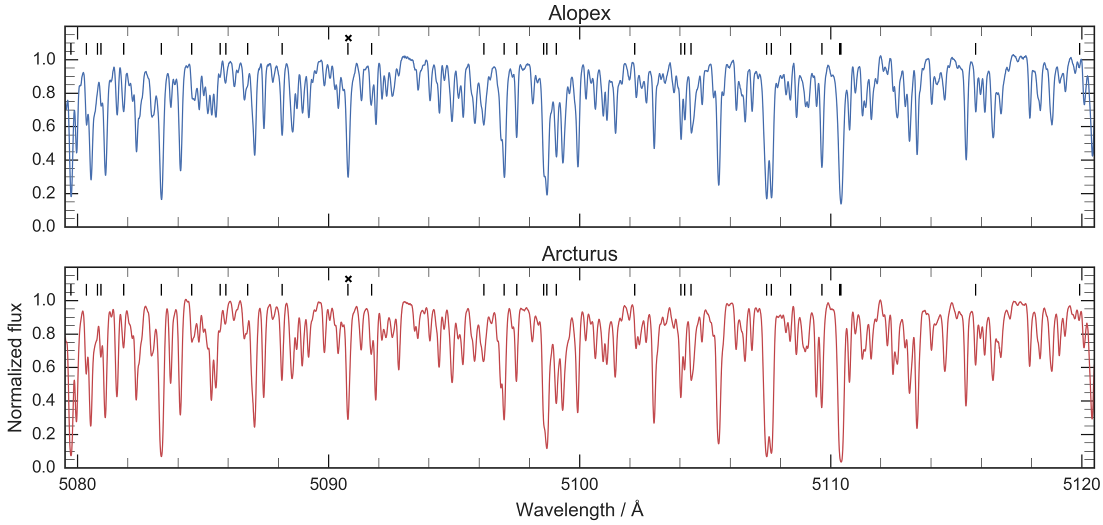
Alopex
Arcturus
Normalized flux
0.0
0.2
0.4
0.6
0.8
1.0
5080
5090
5100
5110
5120
Wavelength / Å

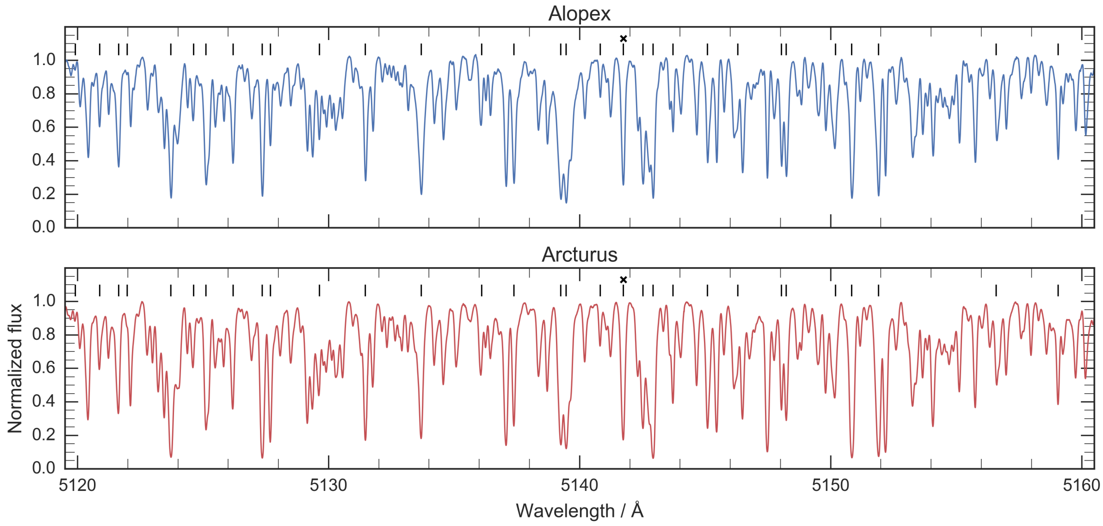
Alopex
Arcturus
Normalized flux
0.0
0.2
0.4
0.6
0.8
1.0
5120
5130
5140
5150
5160
Wavelength / Å

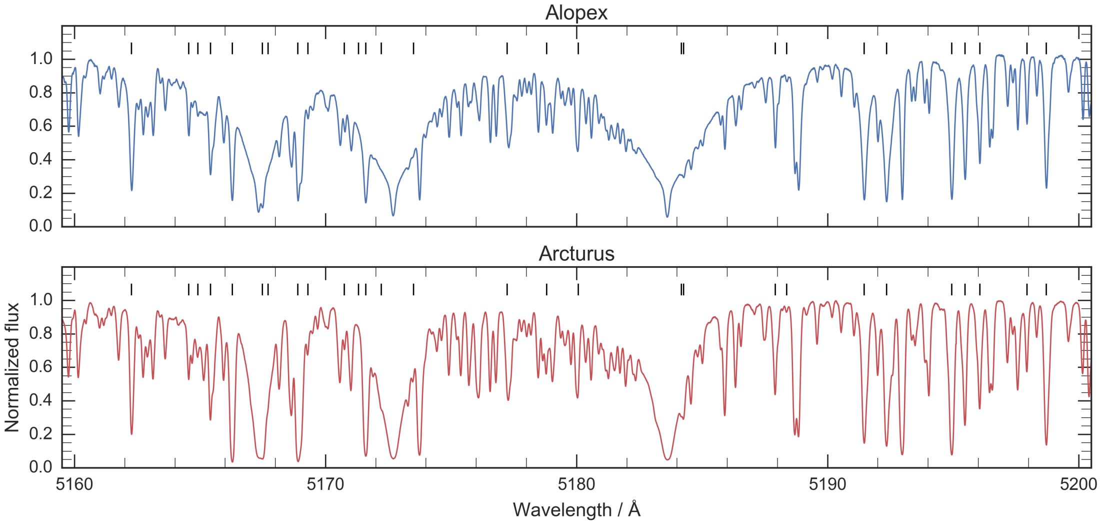
Alopex
1.0
0.8
0.6
0.4
0.2
0.0
Arcturus
Normalized flux
5160
5170
5180
5190
5200
Wavelength / Å

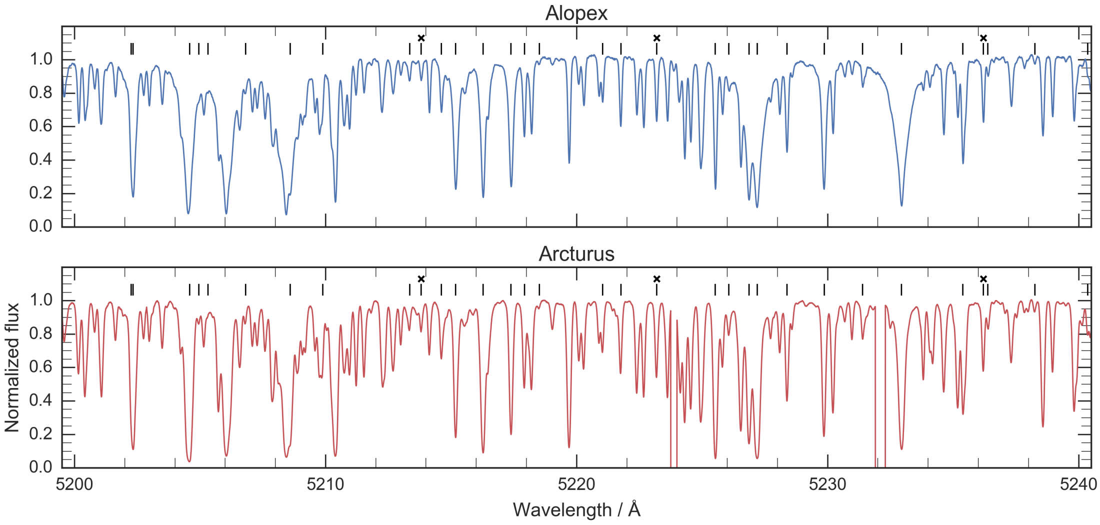
Alopex
1.0
0.8
0.6
0.4
0.2
0.0
Arcturus
Normalized flux
5200
5210
5220
5230
5240
Wavelength / Å

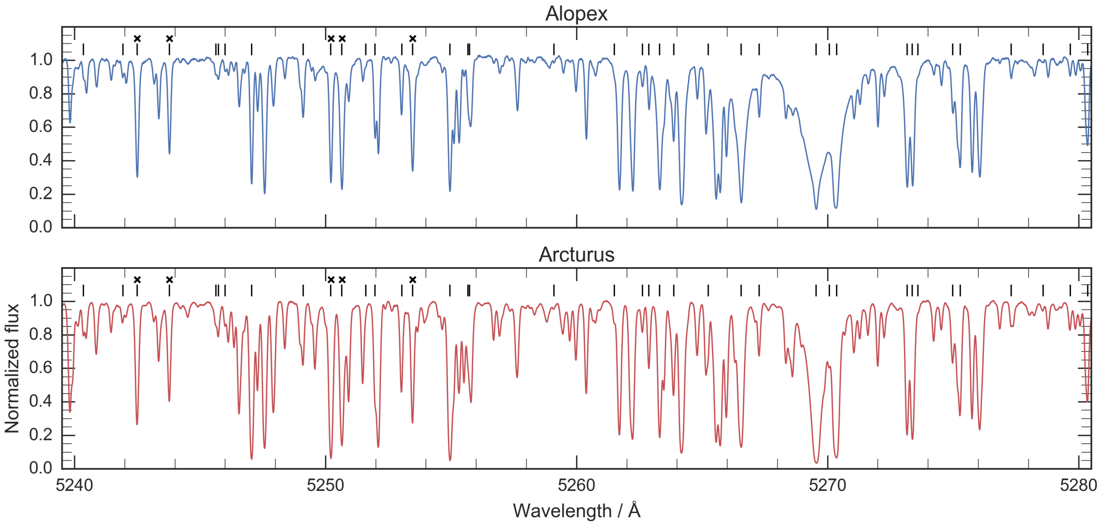
Alopex
1.0
0.8
0.6
0.4
0.2
0.0
Arcturus
Normalized flux
5240
5250
5260
5270
5280
Wavelength / Å

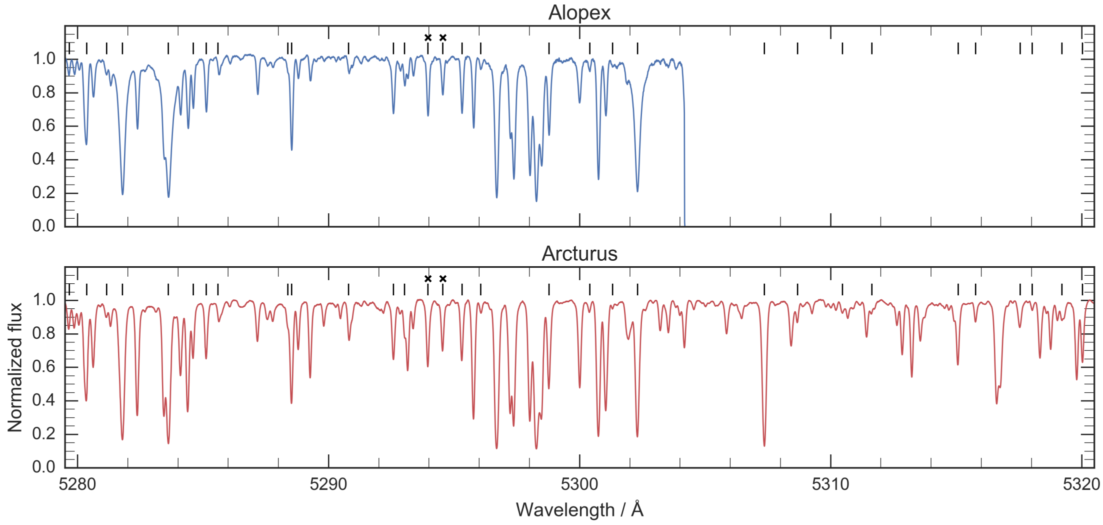
Alopex
Arcturus
Normalized flux
0.0
0.2
0.4
0.6
0.8
1.0
5280
5290
5300
5310
5320
Wavelength / Å

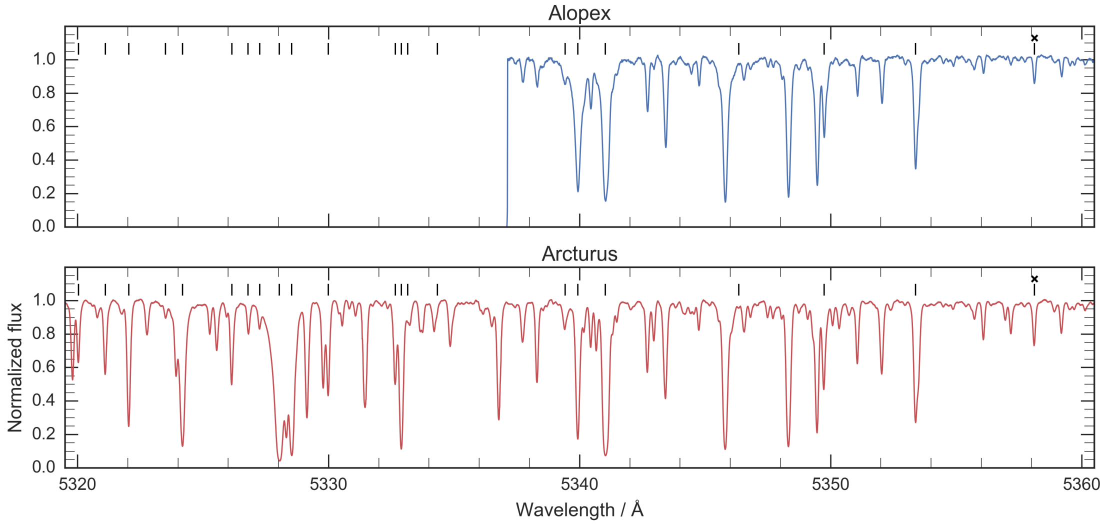
Alopex
Arcturus
Normalized flux
0.0
0.2
0.4
0.6
0.8
1.0
5320
5330
5340
5350
5360
Wavelength / Å

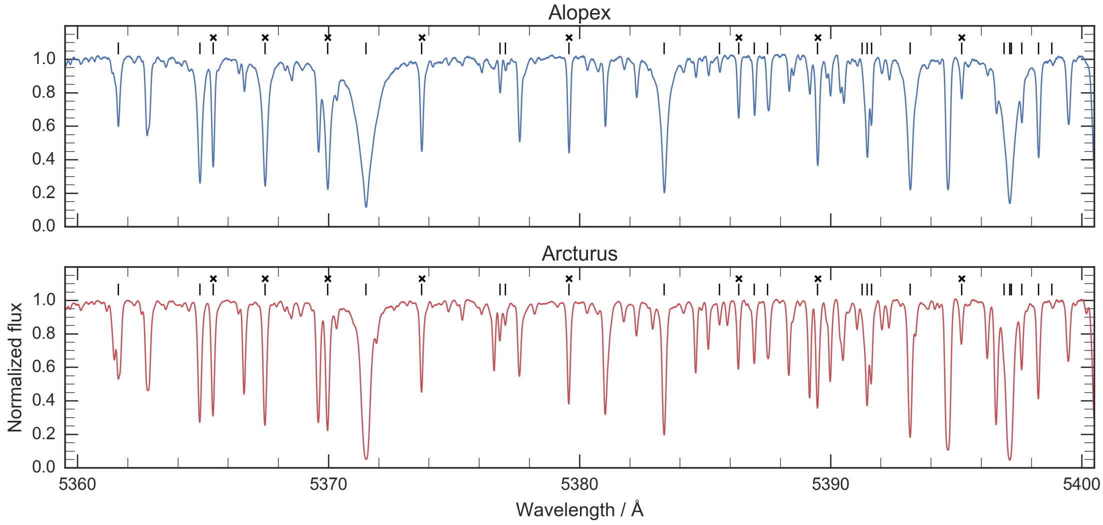
Alopex
Arcturus
Normalized flux
0.0
0.2
0.4
0.6
0.8
1.0
5360
5370
5380
5390
5400
Wavelength / Å

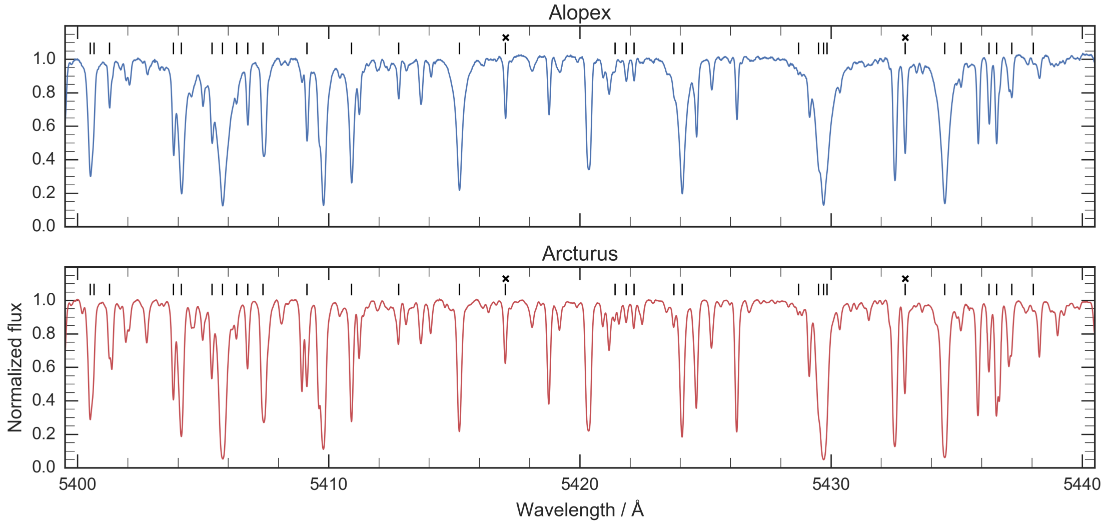
Alopex
Arcturus
Normalized flux
0.0
0.2
0.4
0.6
0.8
1.0
5400
5410
5420
5430
5440
Wavelength / Å

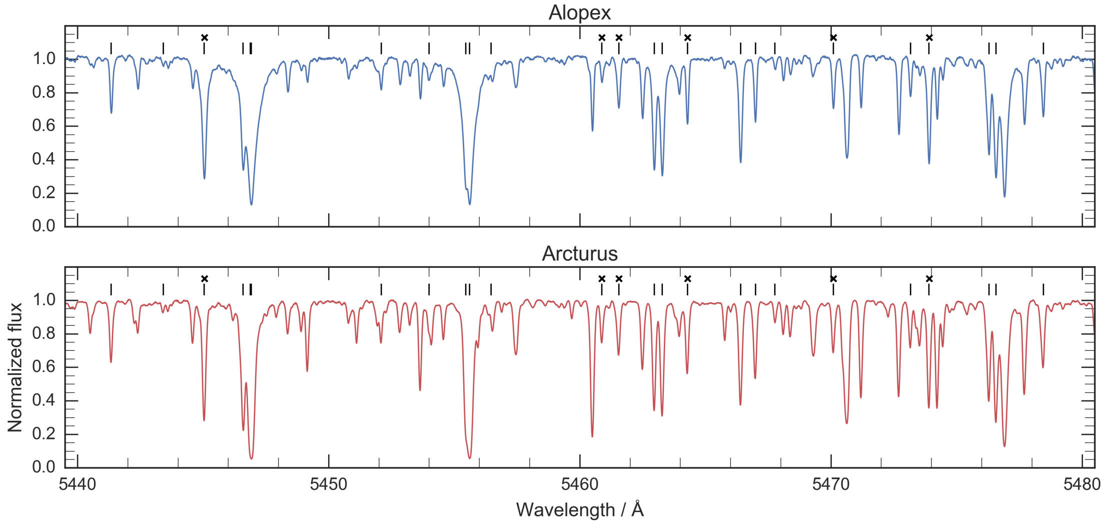
Alopex
Arcturus
Normalized flux
0.0
0.2
0.4
0.6
0.8
1.0
5440
5450
5460
5470
5480
Wavelength / Å

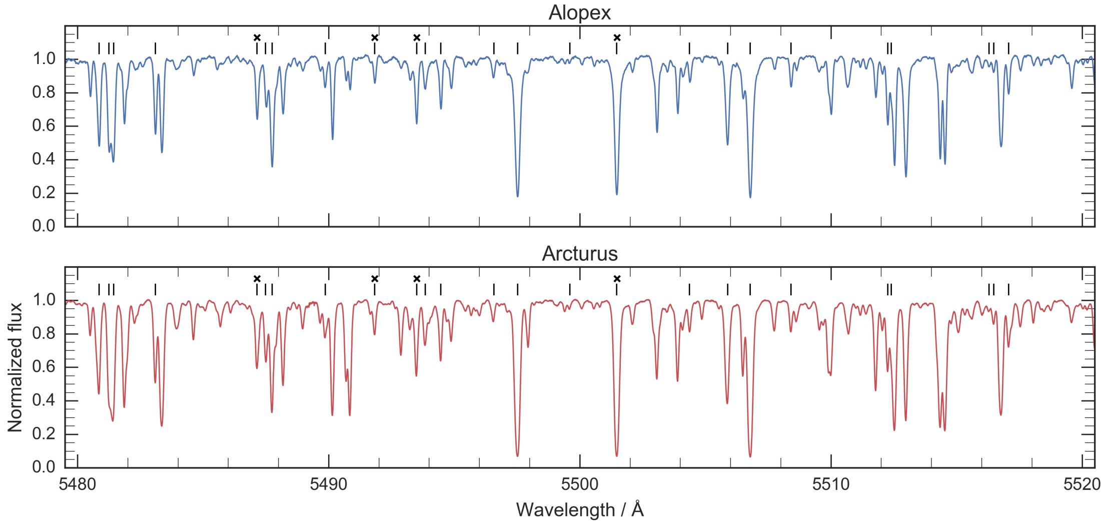
Alopex
Arcturus
Normalized flux
0.0
0.2
0.4
0.6
0.8
1.0
5480
5490
5500
5510
5520
Wavelength / Å

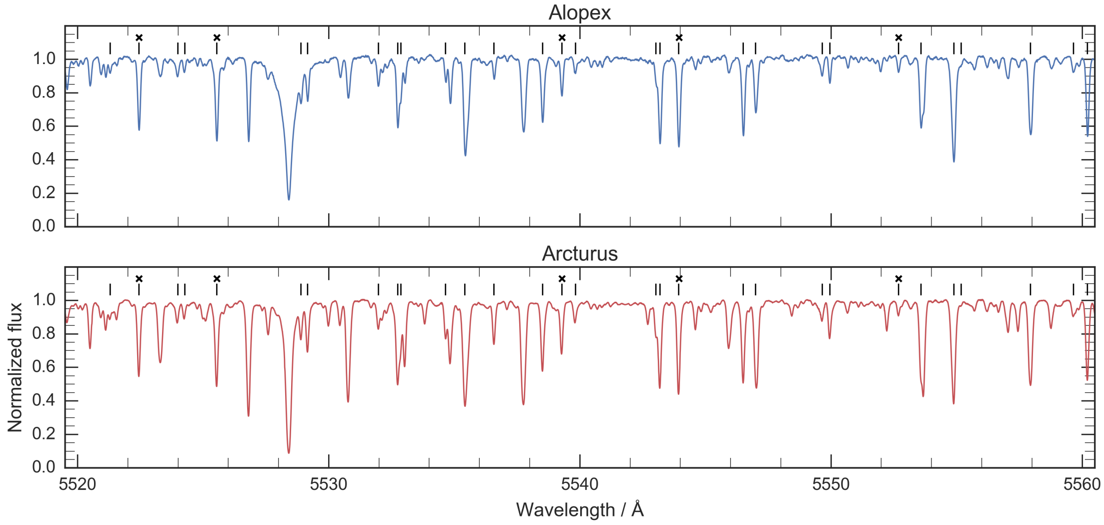
Alopex
Arcturus
Normalized flux
0.0
0.2
0.4
0.6
0.8
1.0
5520
5530
5540
5550
5560
Wavelength / Å

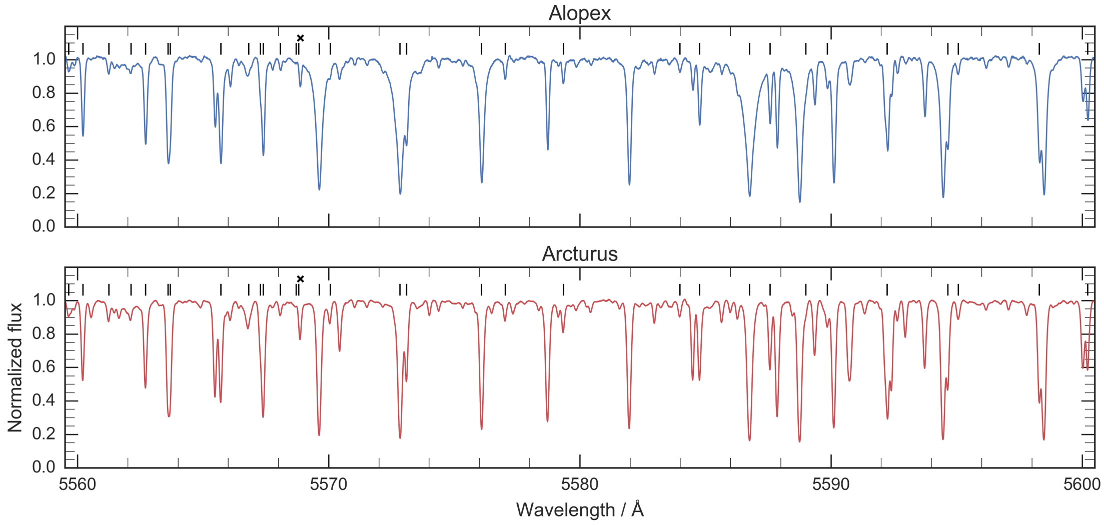
Alopex
Arcturus
Normalized flux
0.0
0.2
0.4
0.6
0.8
1.0
5560
5570
5580
5590
5600
Wavelength / Å

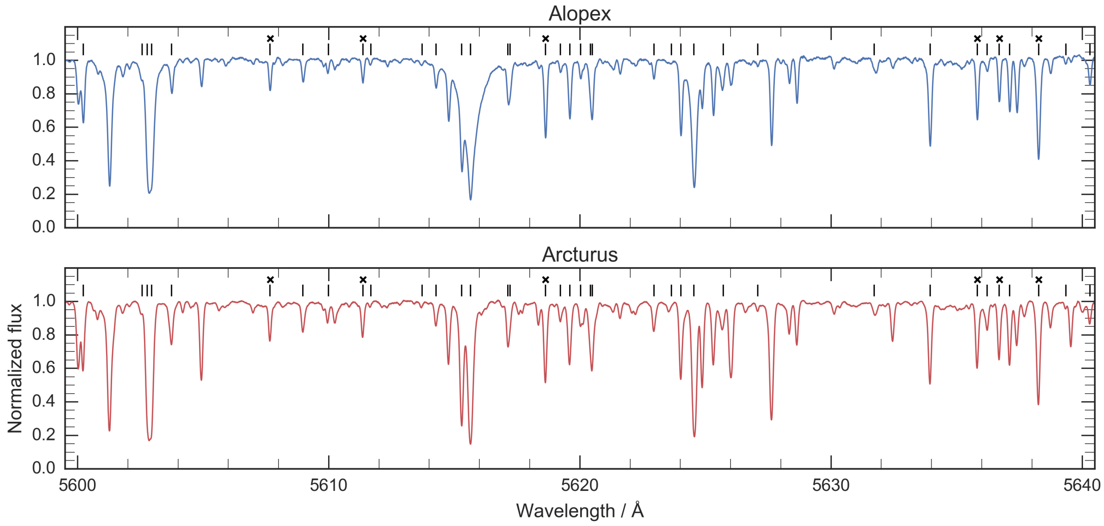
Alopex
Arcturus
Normalized flux
0.0
0.2
0.4
0.6
0.8
1.0
5600
5610
5620
5630
5640
Wavelength / Å

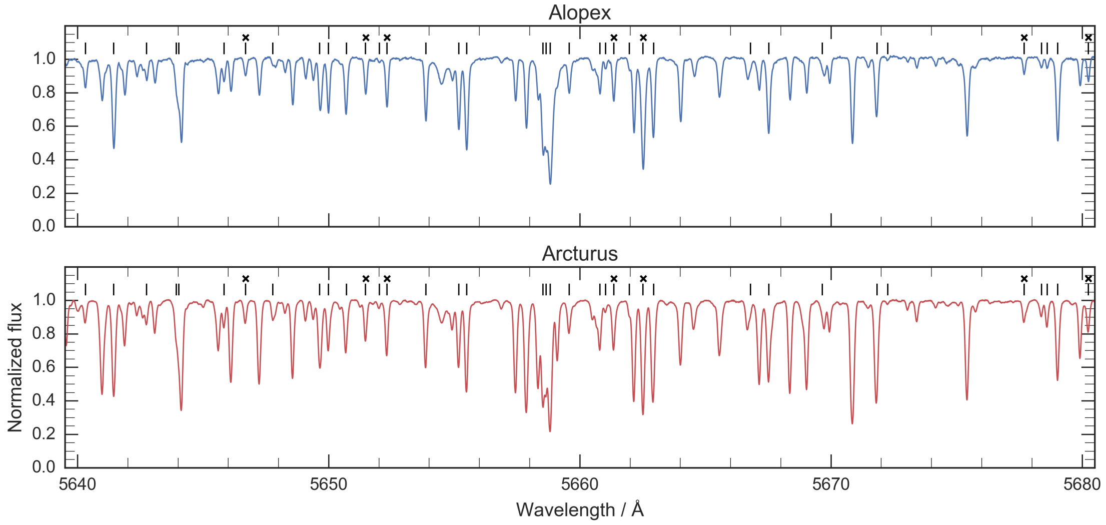
Alopex
Arcturus
Normalized flux
0.0
0.2
0.4
0.6
0.8
1.0
5640
5650
5660
5670
5680
Wavelength / Å

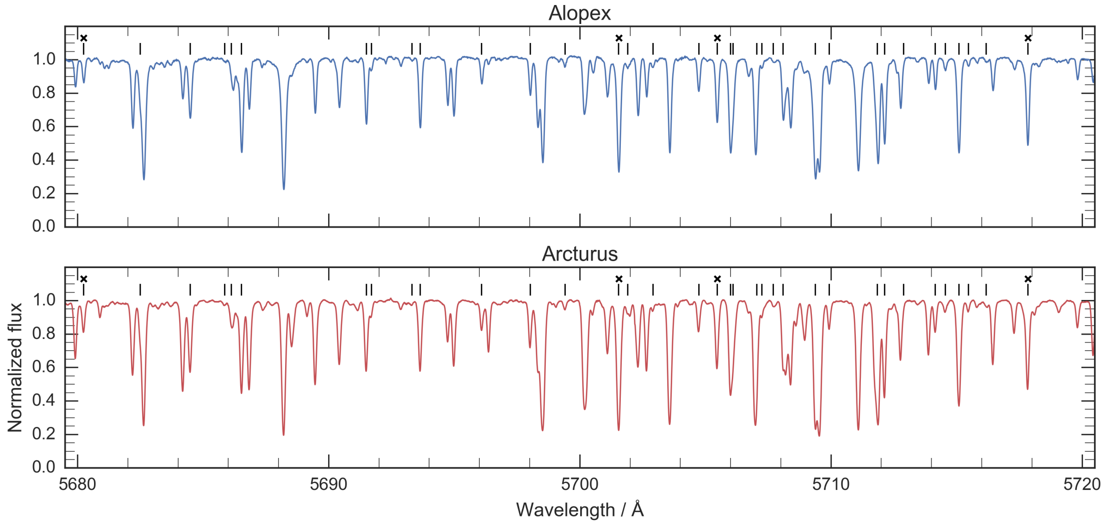
Alopex
Arcturus
Normalized flux
0.0
0.2
0.4
0.6
0.8
1.0
5680
5690
5700
5710
5720
Wavelength / Å

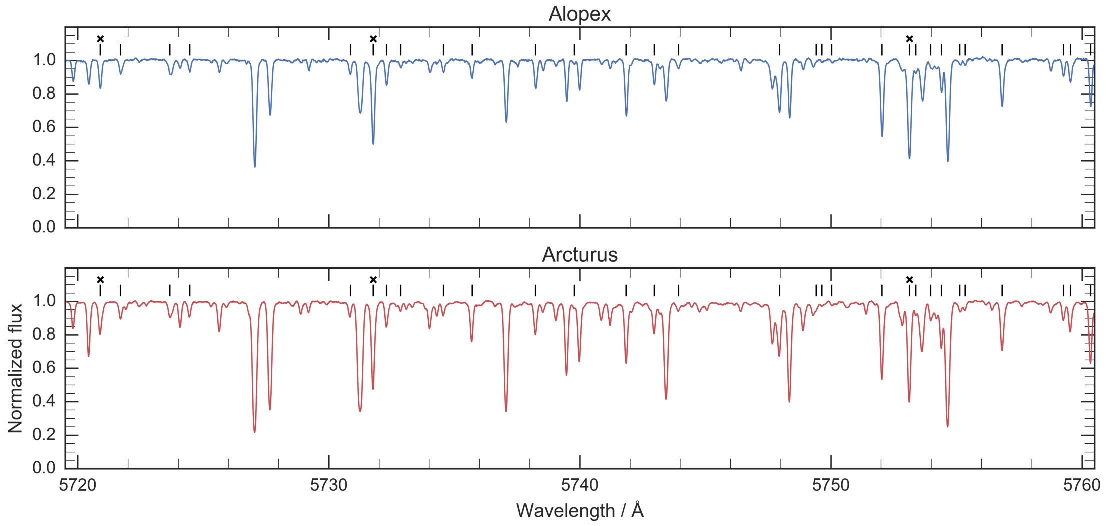
Alopex
Arcturus
Normalized flux
0.0
0.2
0.4
0.6
0.8
1.0
5720
5730
5740
5750
5760
Wavelength / Å

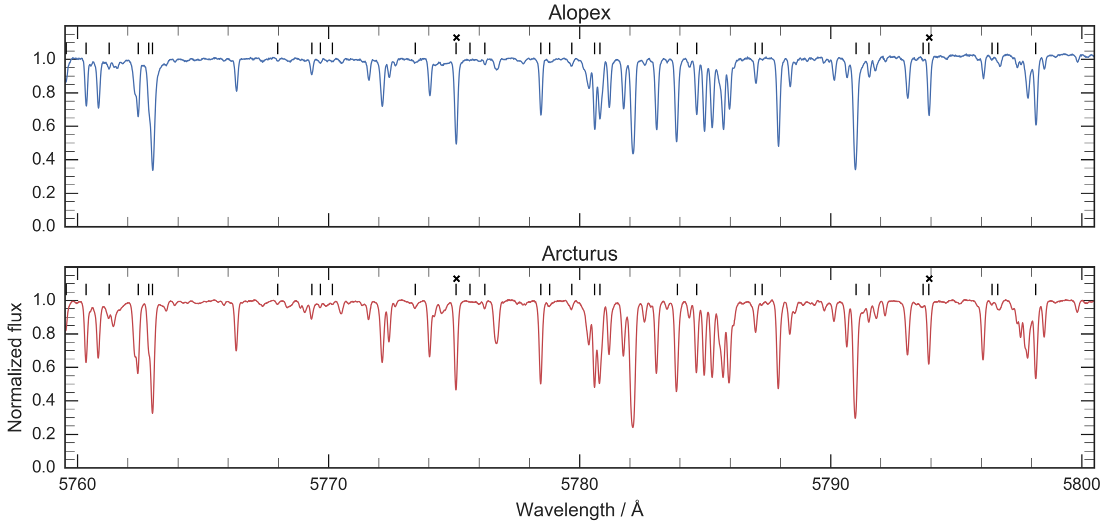
Alopex
Arcturus
Normalized flux
0.0
0.2
0.4
0.6
0.8
1.0
5760
5770
5780
5790
5800
Wavelength / Å

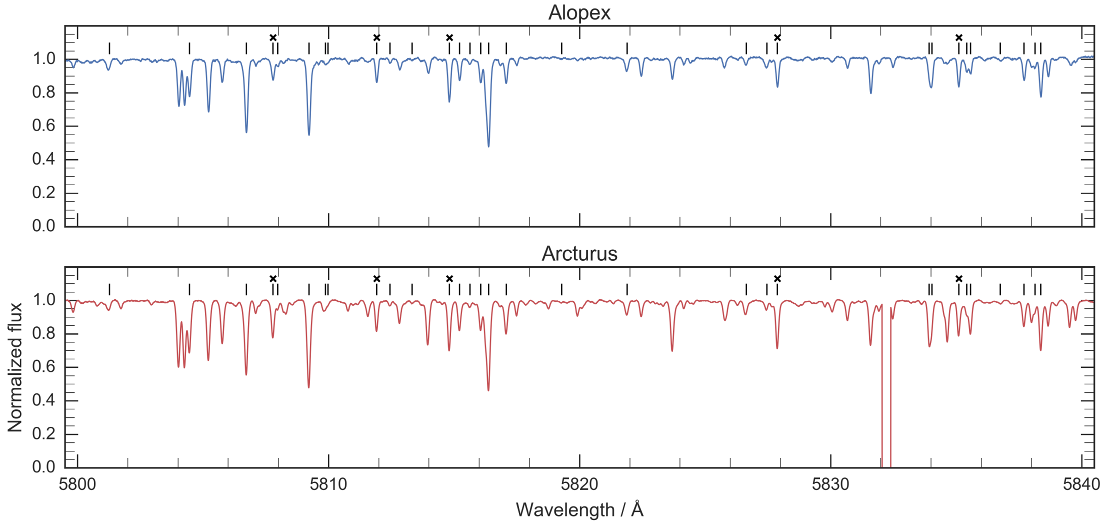
Alopex
Arcturus
Normalized flux
0.0
0.2
0.4
0.6
0.8
1.0
5800
5810
5820
5830
5840
Wavelength / Å

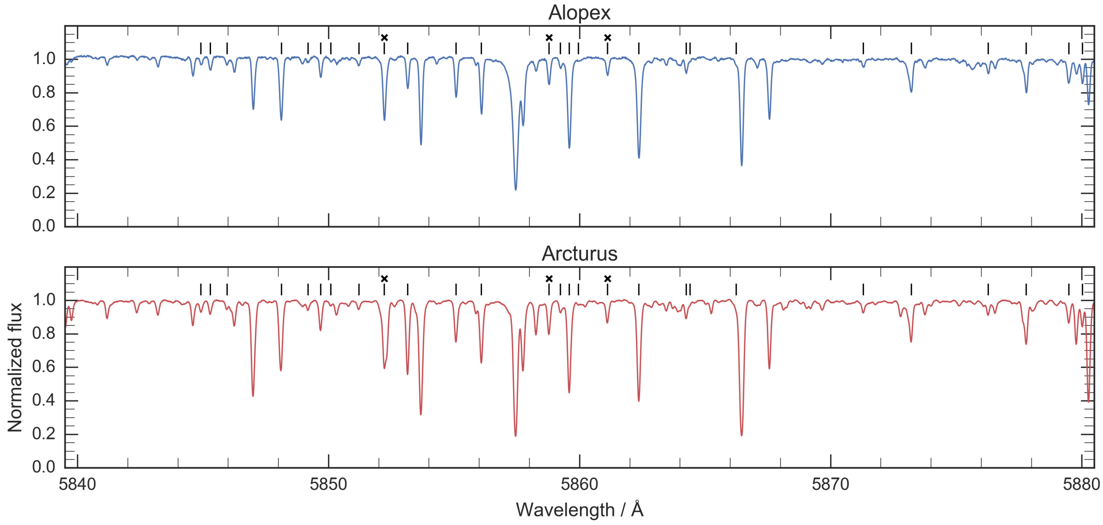
Alopex
Arcturus
Normalized flux
0.0
0.2
0.4
0.6
0.8
1.0
5840
5850
5860
5870
5880
Wavelength / Å

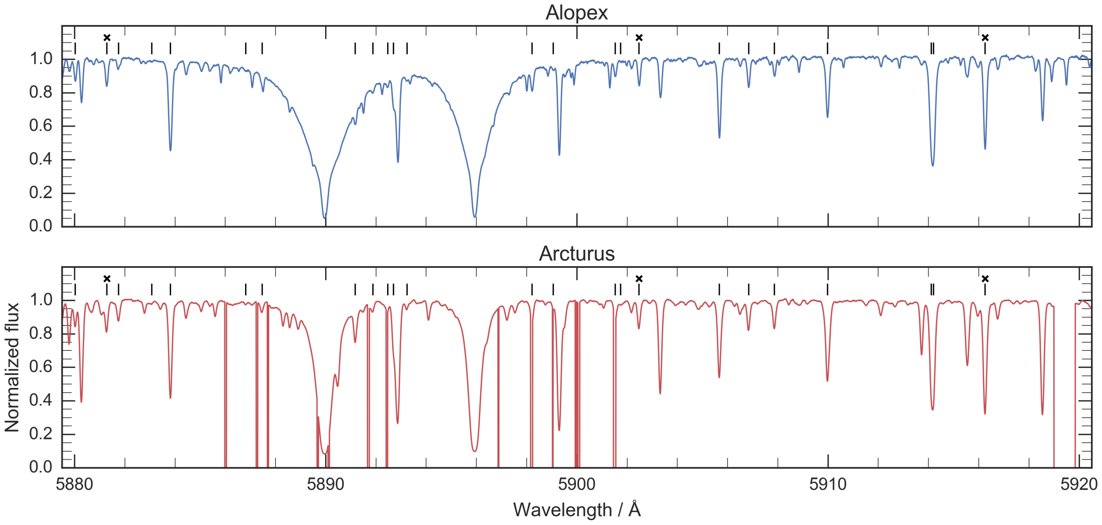
Alopex
Arcturus
Normalized flux
0.0
0.2
0.4
0.6
0.8
1.0
5880
5890
5900
5910
5920
Wavelength / Å

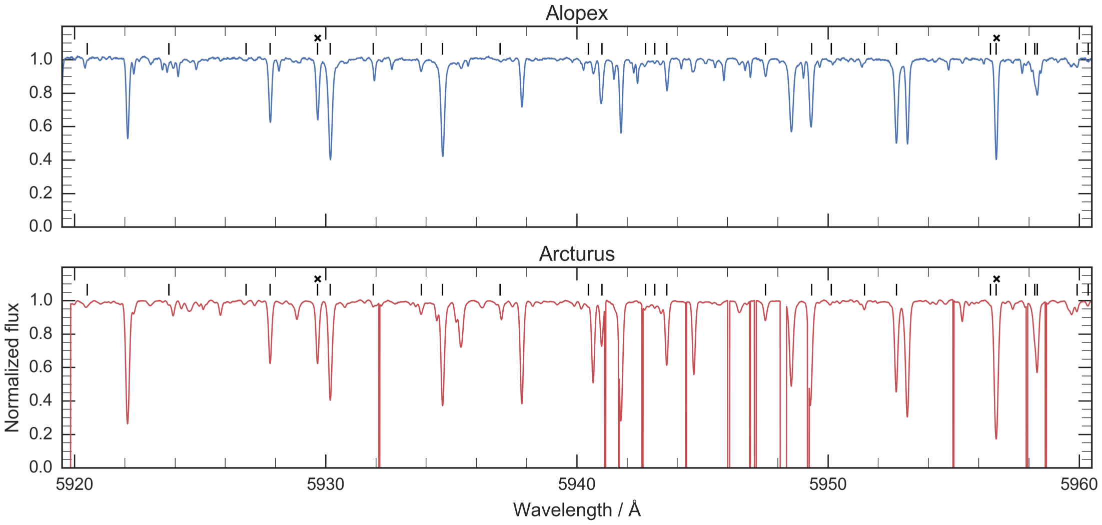
Alopex
Arcturus
Normalized flux
0.0
0.2
0.4
0.6
0.8
1.0
5920
5930
5940
5950
5960
Wavelength / Å

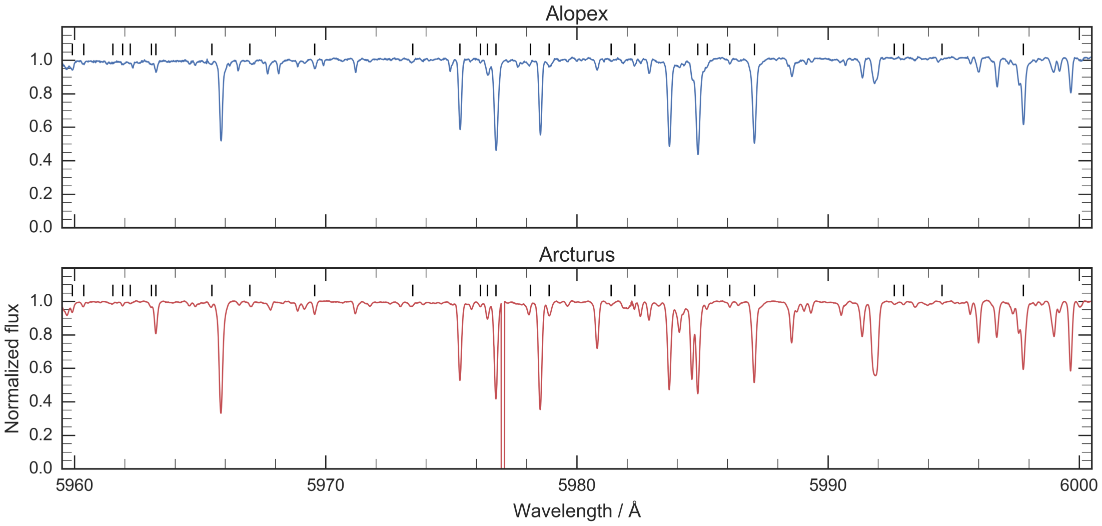
Alopex
Arcturus
Normalized flux
0.0
0.2
0.4
0.6
0.8
1.0
5960
5970
5980
5990
6000
Wavelength / Å

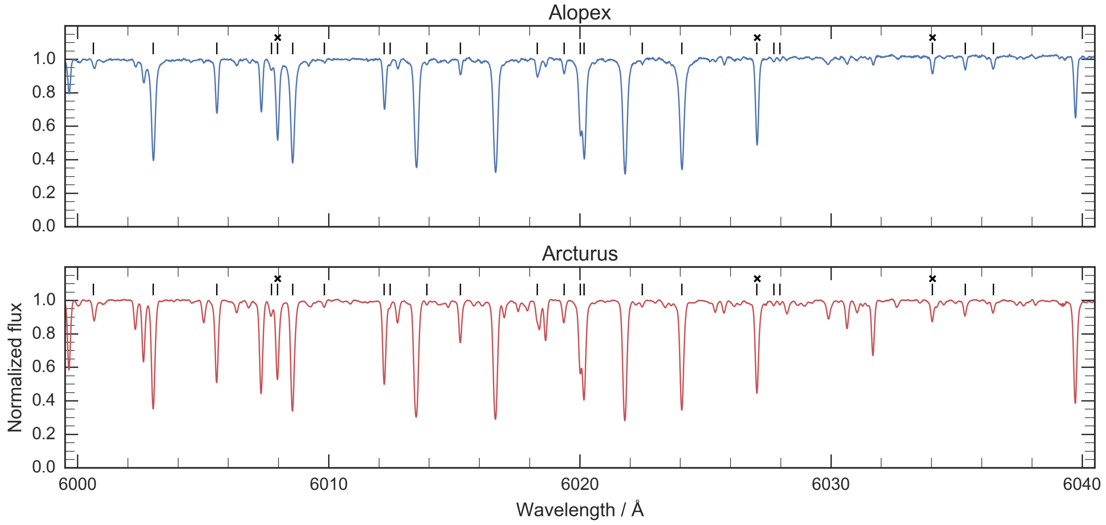
Alopex
Arcturus
Normalized flux
0.0
0.2
0.4
0.6
0.8
1.0
6000
6010
6020
6030
6040
Wavelength / Å

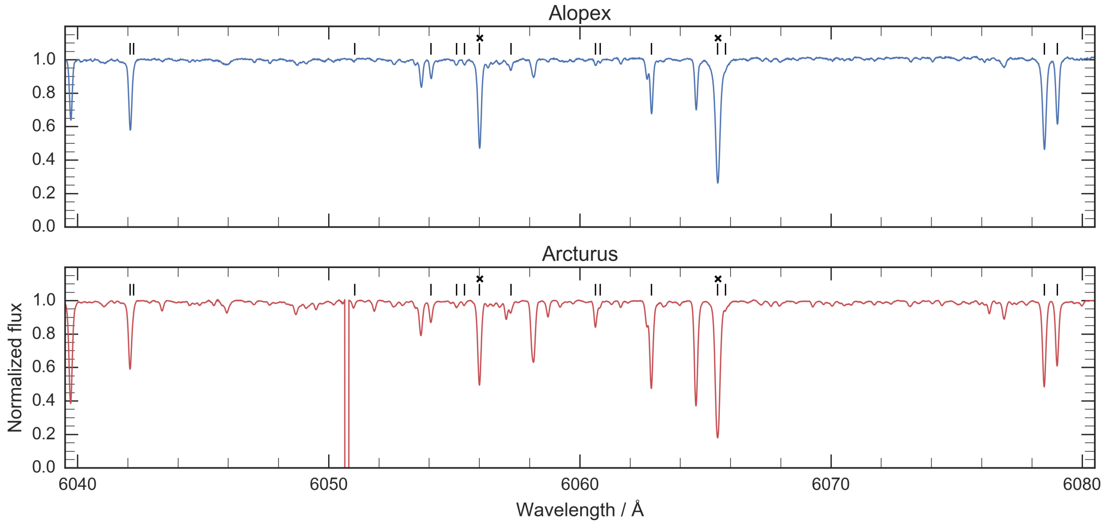
Alopex
Arcturus
Normalized flux
0.0
0.2
0.4
0.6
0.8
1.0
6040
6050
6060
6070
6080
Wavelength / Å

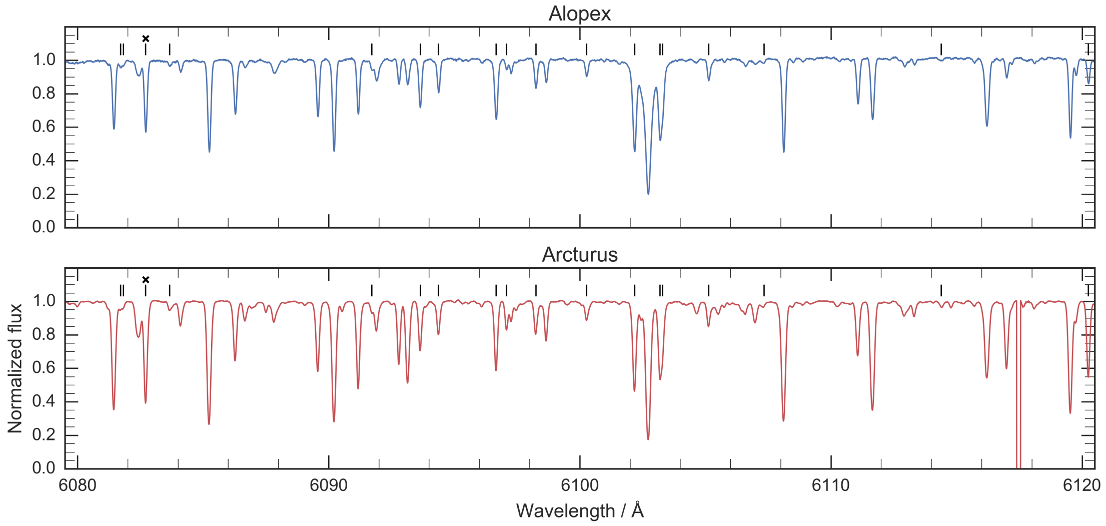
Alopex
Arcturus
Normalized flux
0.0
0.2
0.4
0.6
0.8
1.0
6080
6090
6100
6110
6120
Wavelength / Å

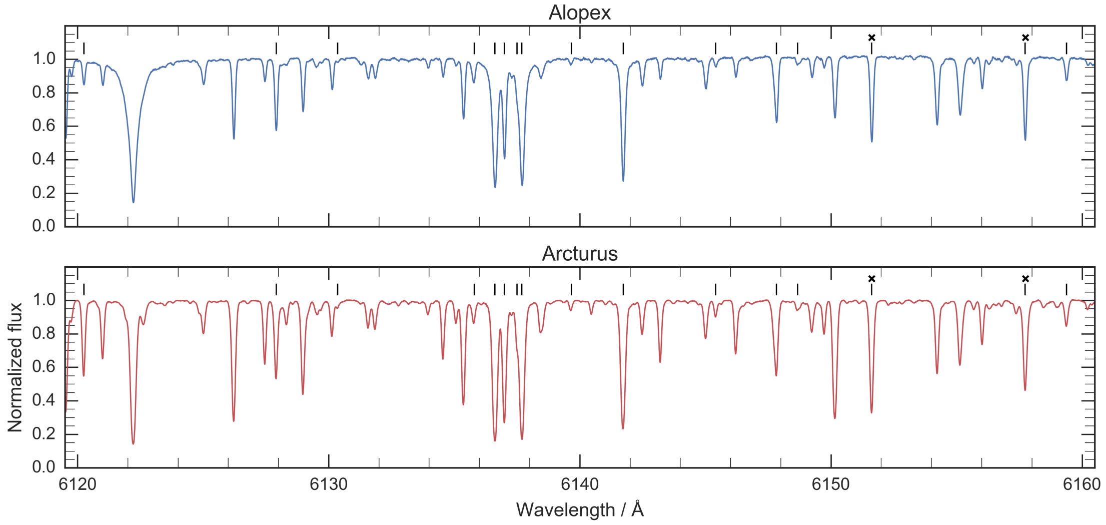
Alopex
Arcturus
Normalized flux
0.0
0.2
0.4
0.6
0.8
1.0
6120
6130
6140
6150
6160
Wavelength / Å

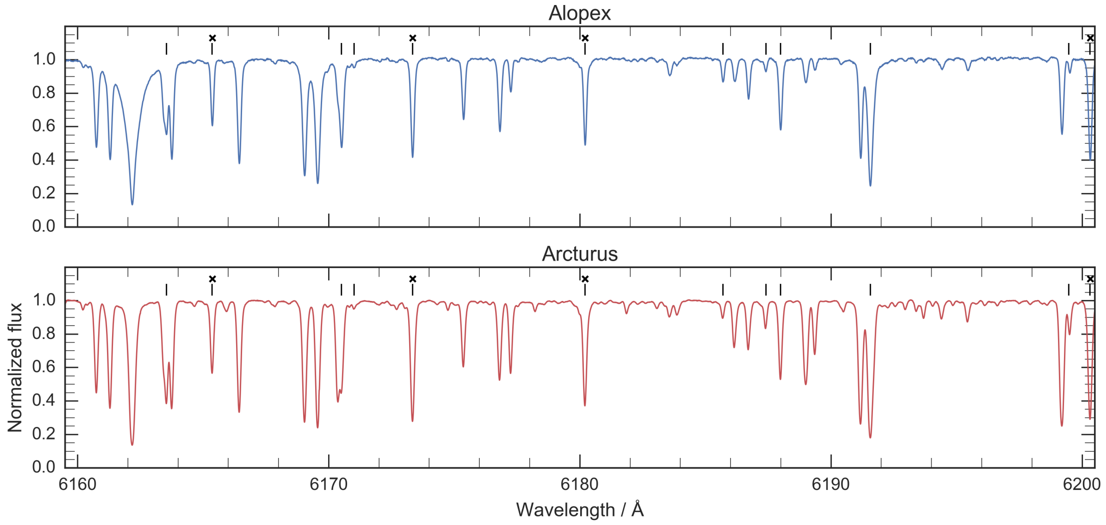
Alopex
Arcturus
Normalized flux
0.0
0.2
0.4
0.6
0.8
1.0
6160
6170
6180
6190
6200
Wavelength / Å

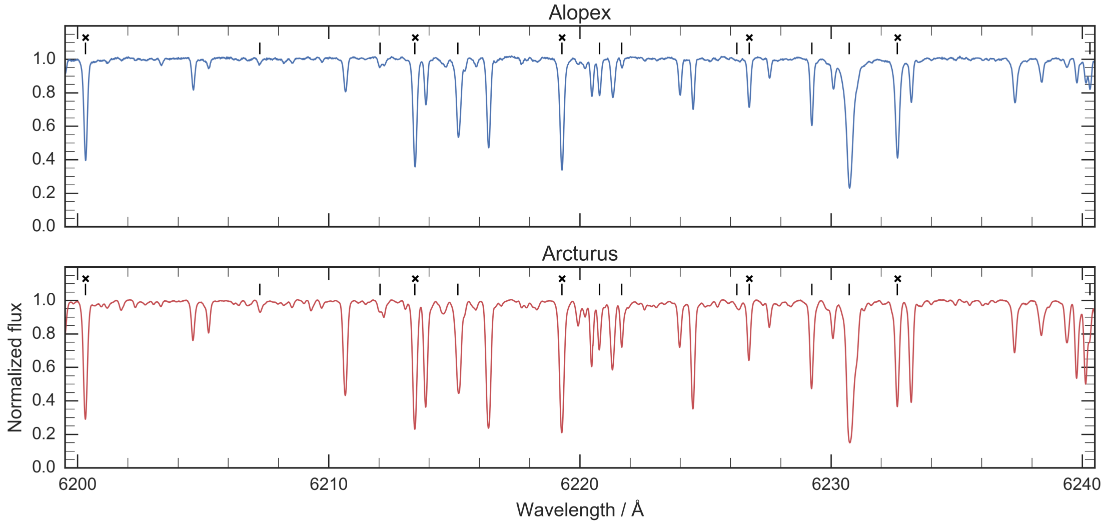
Alopex
Arcturus
Normalized flux
0.0
0.2
0.4
0.6
0.8
1.0
6200
6210
6220
6230
6240
Wavelength / Å

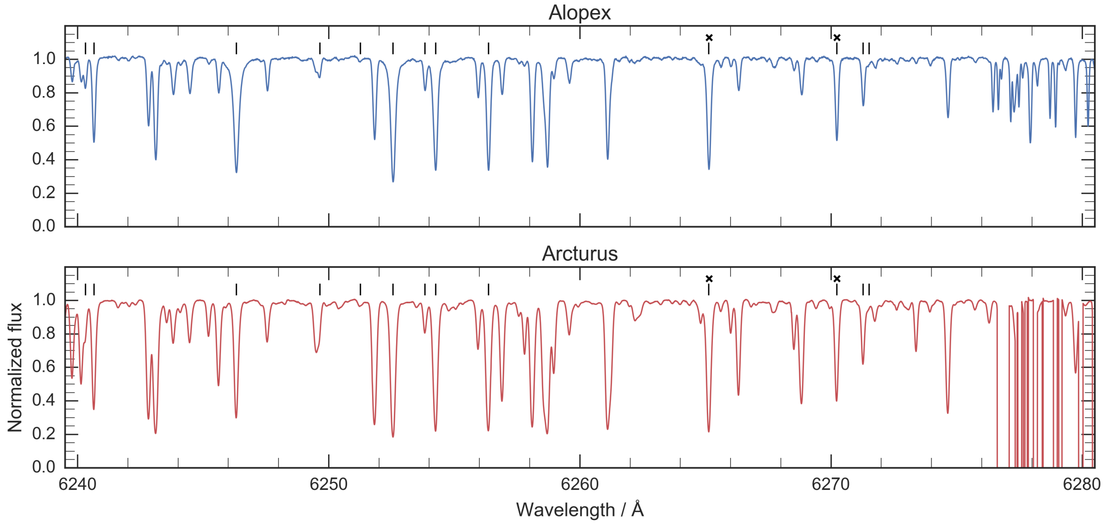
Alopex
Arcturus
Normalized flux
0.0
0.2
0.4
0.6
0.8
1.0
6240
6250
6260
6270
6280
Wavelength / Å

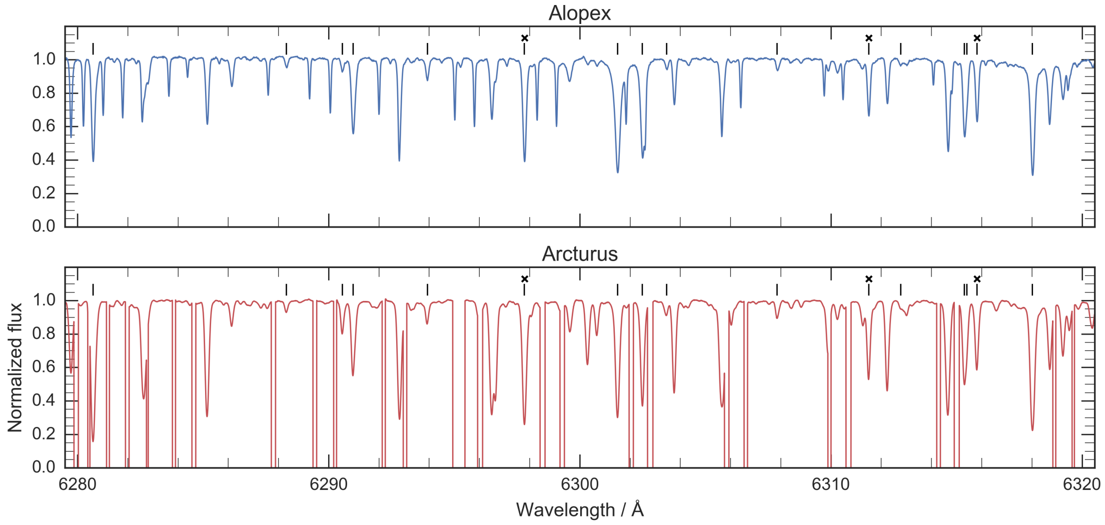
Alopex
Arcturus
Normalized flux
0.0
0.2
0.4
0.6
0.8
1.0
6280
6290
6300
6310
6320
Wavelength / Å

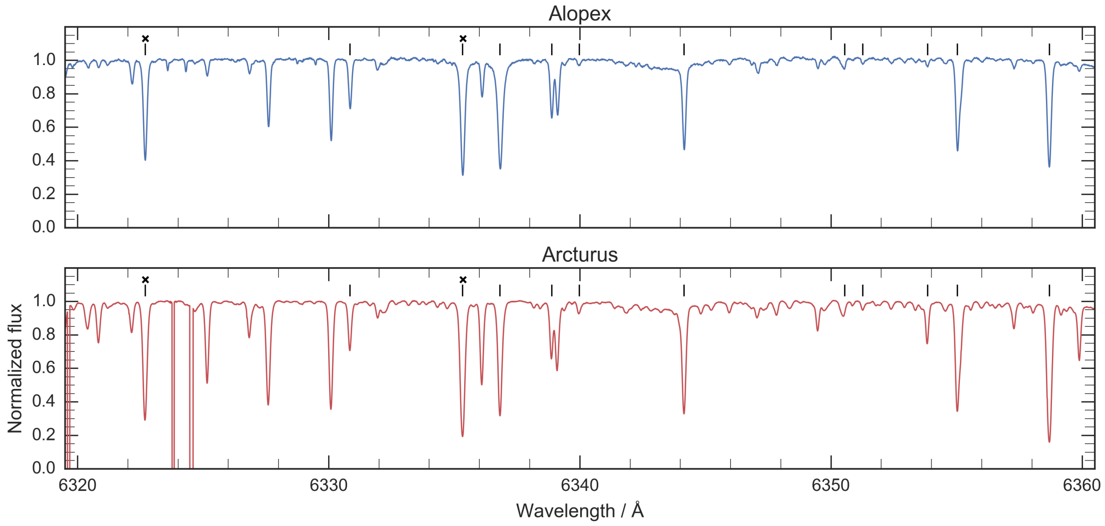
Alopex
Arcturus
Normalized flux
0.0
0.2
0.4
0.6
0.8
1.0
6320
6330
6340
6350
6360
Wavelength / Å

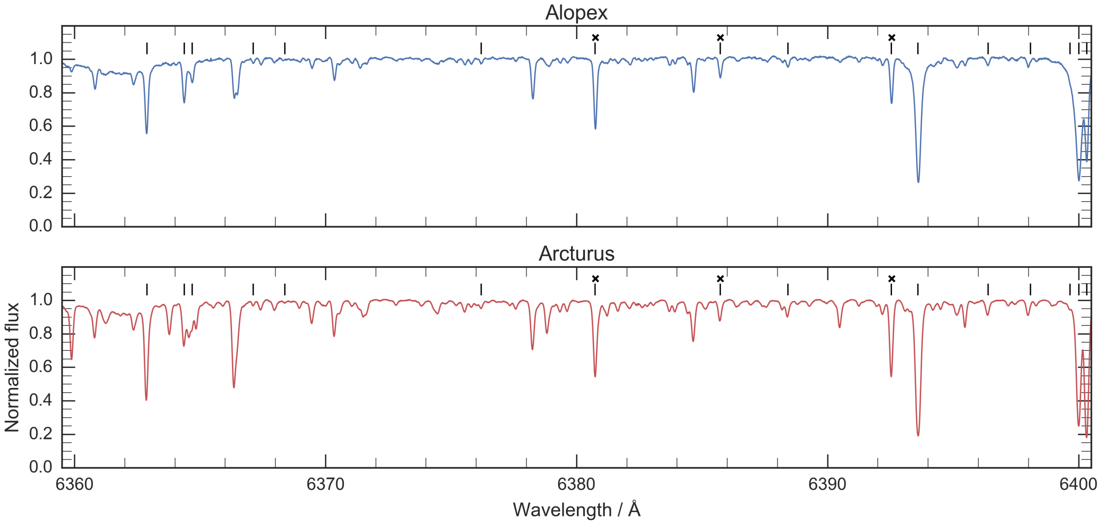
Alopex
Arcturus
Normalized flux
0.0
0.2
0.4
0.6
0.8
1.0
6360
6370
6380
6390
6400
Wavelength / Å

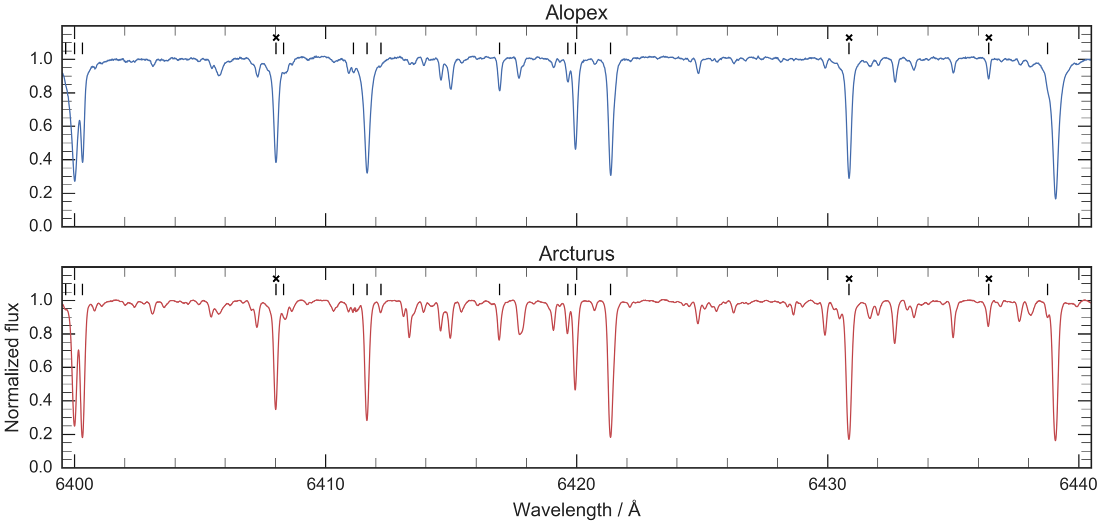
Alopex
Arcturus
Normalized flux
0.0
0.2
0.4
0.6
0.8
1.0
6400
6410
6420
6430
6440
Wavelength / Å

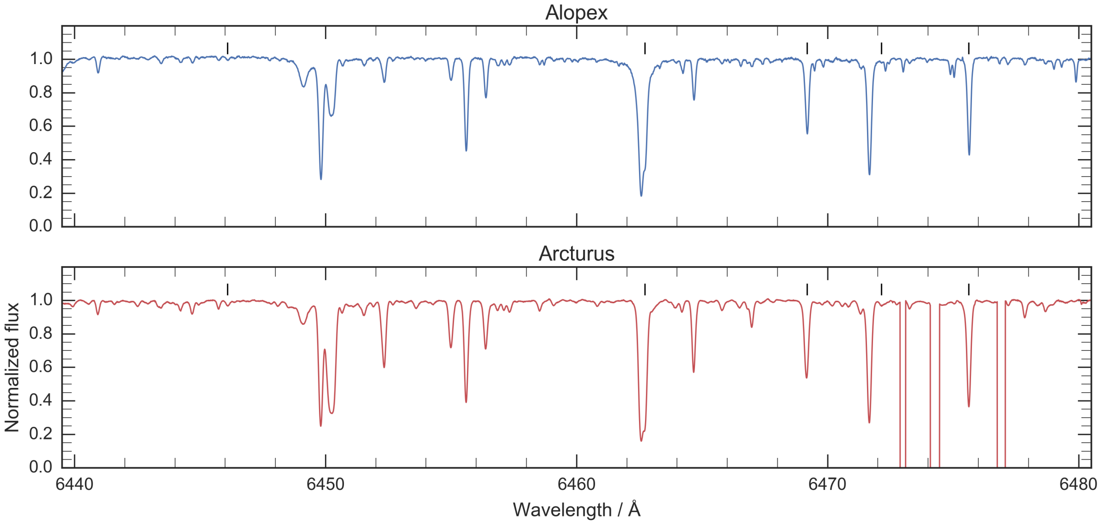
Alopex
Arcturus
Normalized flux
0.0
0.2
0.4
0.6
0.8
1.0
6440
6450
6460
6470
6480
Wavelength / Å

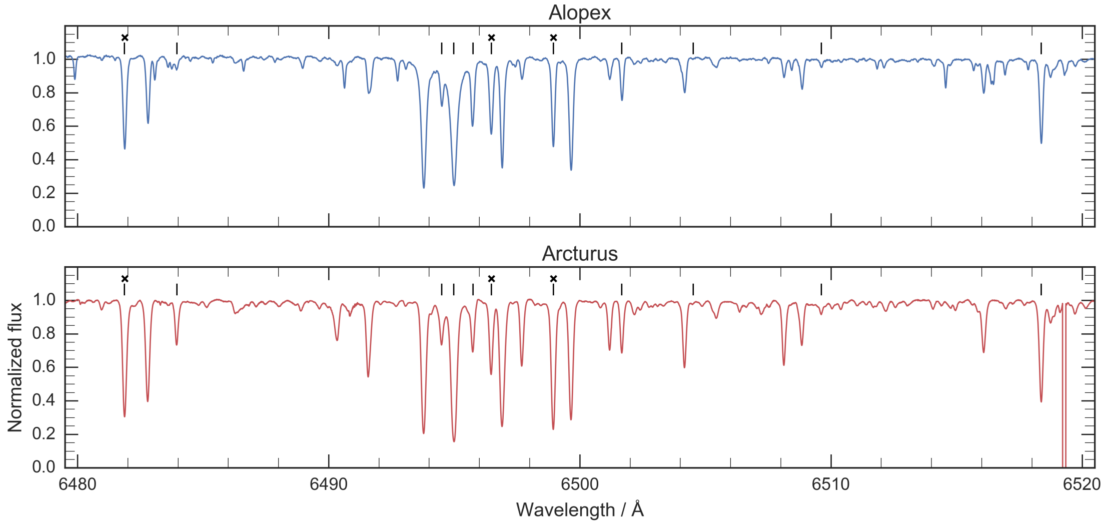
Alopex
Arcturus
Normalized flux
0.0
0.2
0.4
0.6
0.8
1.0
6480
6490
6500
6510
6520
Wavelength / Å

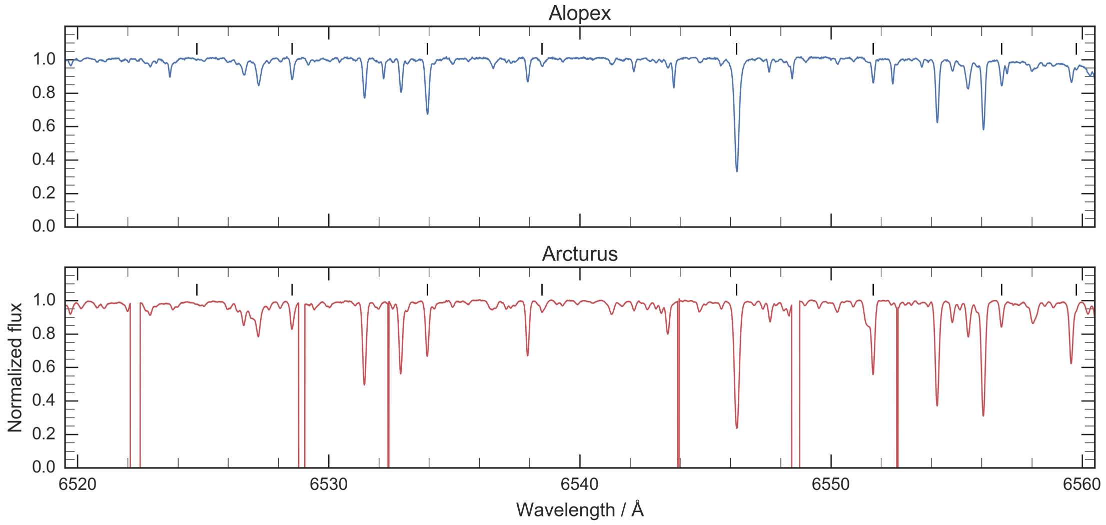
Alopex
Arcturus
Normalized flux
0.0
0.2
0.4
0.6
0.8
1.0
6520
6530
6540
6550
6560
Wavelength / Å

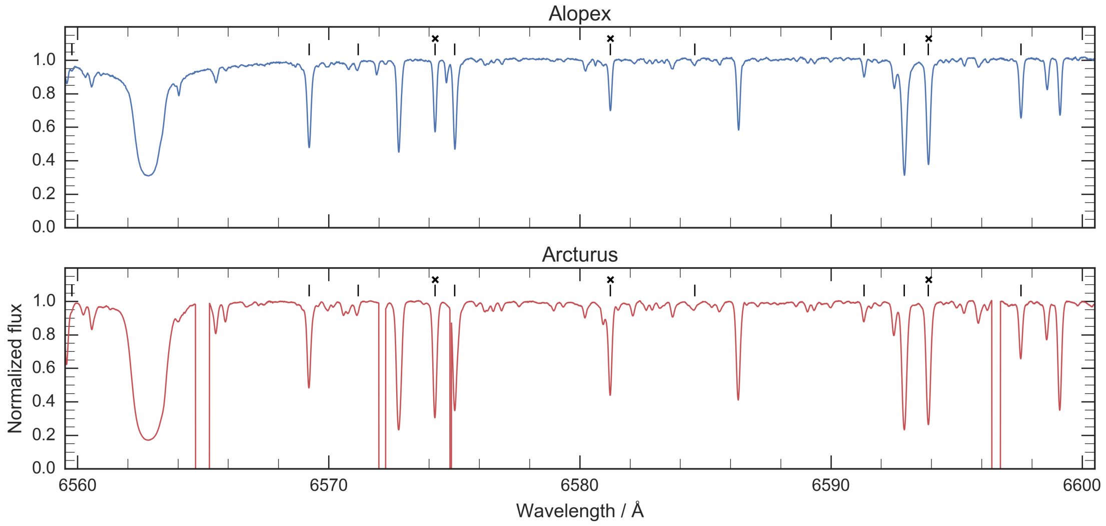
Alopex
Arcturus
Normalized flux
0.0
0.2
0.4
0.6
0.8
1.0
6560
6570
6580
6590
6600
Wavelength / Å

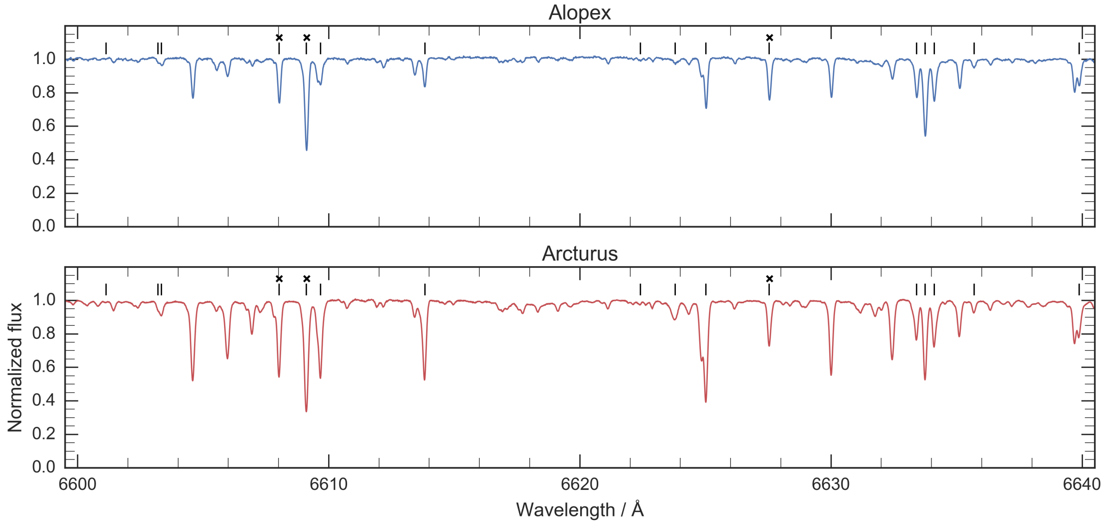
Alopex
Arcturus
Normalized flux
0.0
0.2
0.4
0.6
0.8
1.0
6600
6610
6620
6630
6640
Wavelength / Å

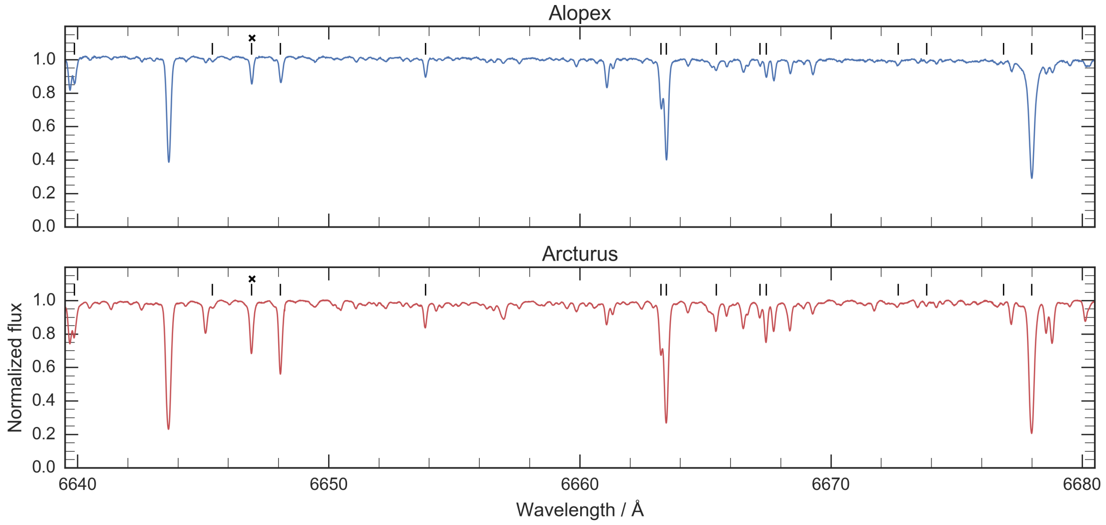
Alopex
Arcturus
Normalized flux
0.0
0.2
0.4
0.6
0.8
1.0
6640
6650
6660
6670
6680
Wavelength / Å

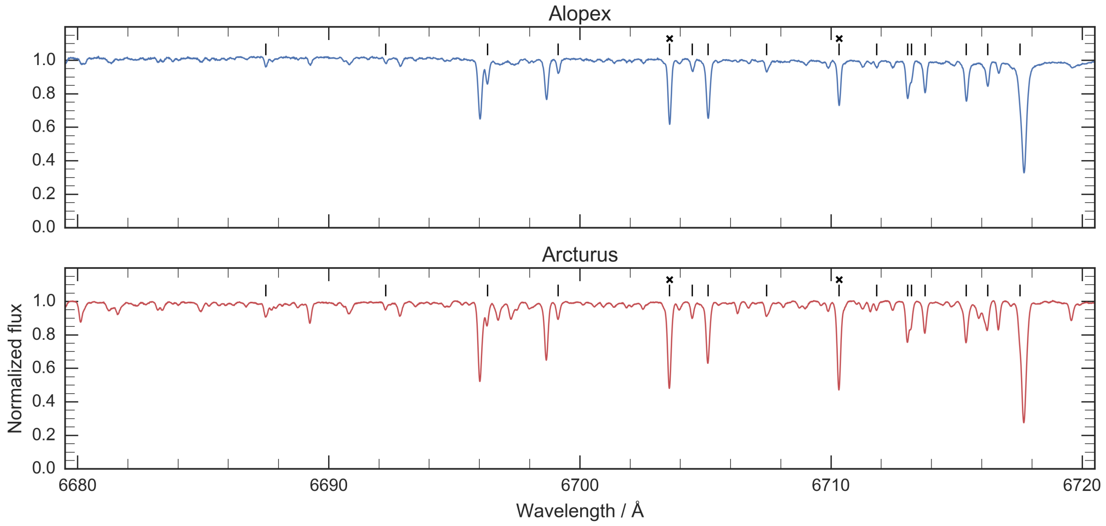
Alopex
Arcturus
Normalized flux
0.0
0.2
0.4
0.6
0.8
1.0
6680
6690
6700
6710
6720
Wavelength / Å

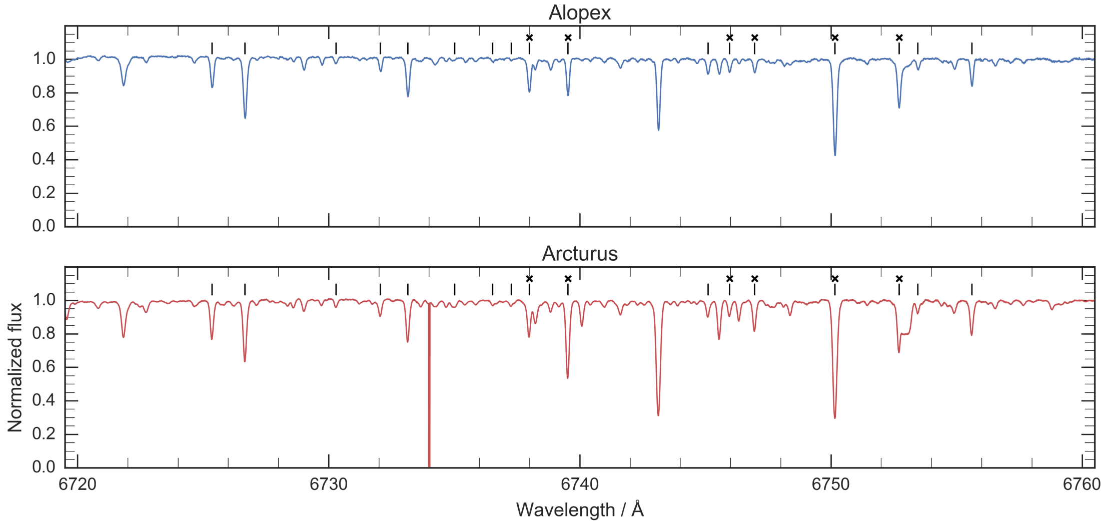
Alopex
Arcturus
Normalized flux
1.0
0.8
0.6
0.4
0.2
0.0
6720
6730
6740
6750
6760
Wavelength / Å

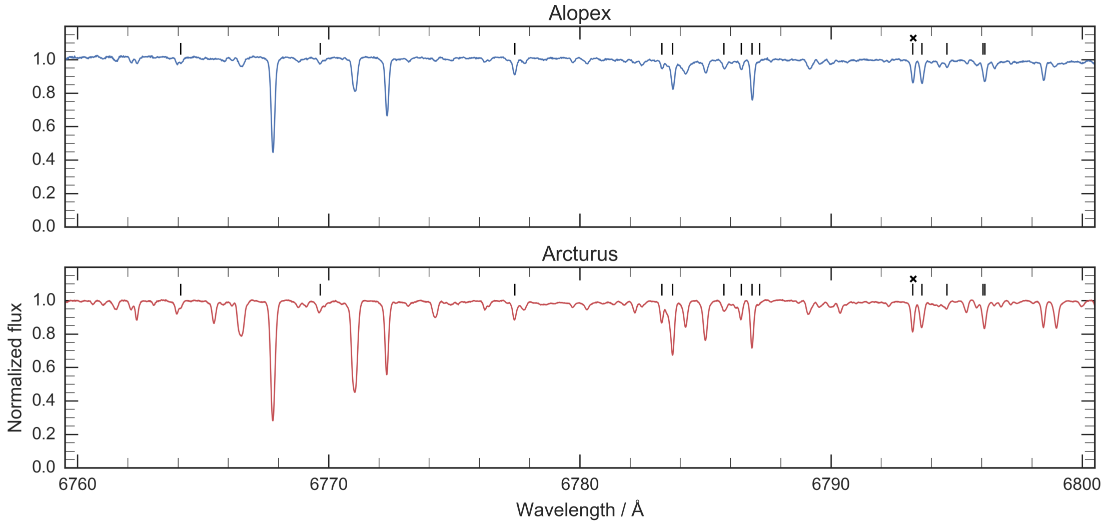
Alopex
Arcturus
Normalized flux
1.0
0.8
0.6
0.4
0.2
0.0
6760
6770
6780
6790
6800
Wavelength / Å

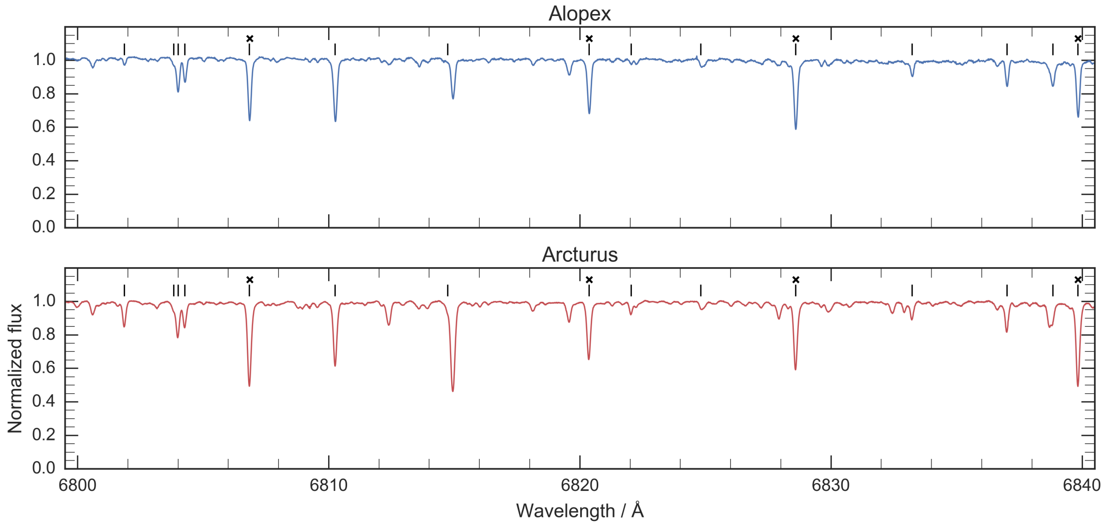
Alopex
Arcturus
Normalized flux
1.0
0.8
0.6
0.4
0.2
0.0
6800
6810
6820
6830
6840
Wavelength / Å

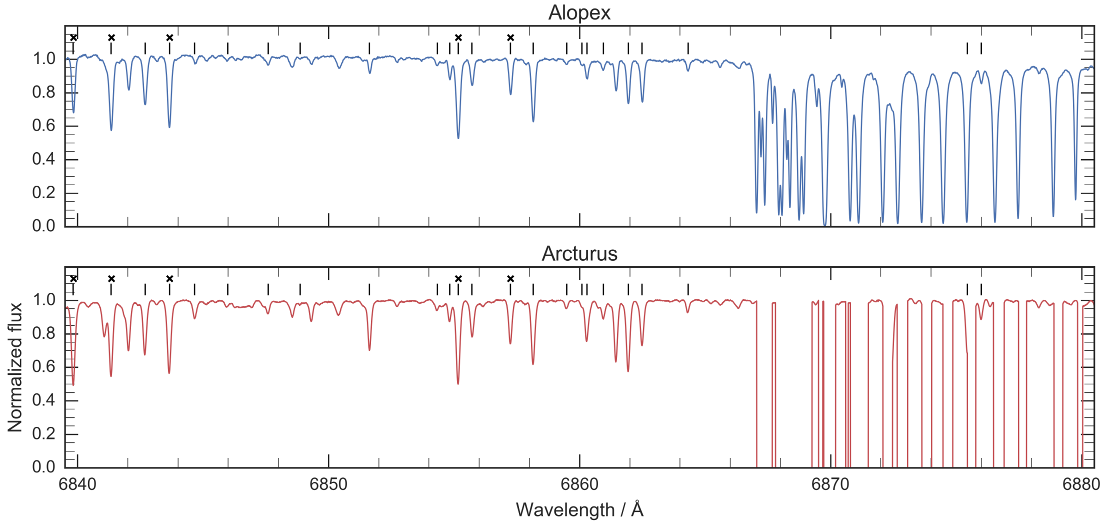
Alopex
Arcturus
Normalized flux
0.0
0.2
0.4
0.6
0.8
1.0
6840
6850
6860
6870
6880
Wavelength / Å

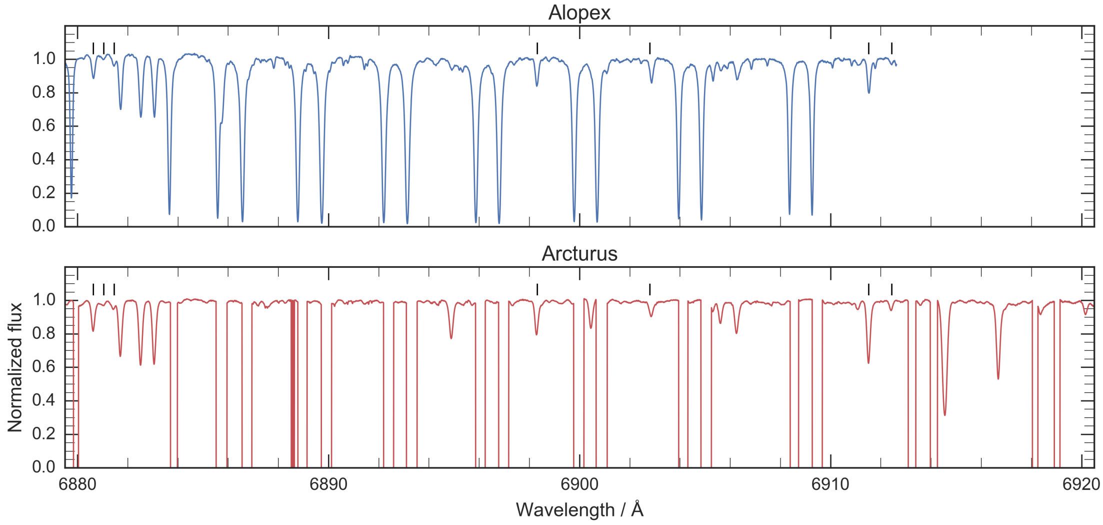
Alopex
Arcturus
Normalized flux
0.0
0.2
0.4
0.6
0.8
1.0
6880
6890
6900
6910
6920
Wavelength / Å

B

‘Cool Stars 19’ conference poster

Below is a poster contribution by Gustavsson et al. (2016) to the *The Cambridge Workshop on Cool Stars, Stellar Systems, and the Sun 19*, 6–10 June, 2016, in Uppsala, Sweden.

Solar surface granulation in Ca II H λ 396.37 nm wideband. Observations and image processing by Vasco Henriques; Swedish 1-meter solar telescope on La Palma; Royal Swedish Academy of Sciences

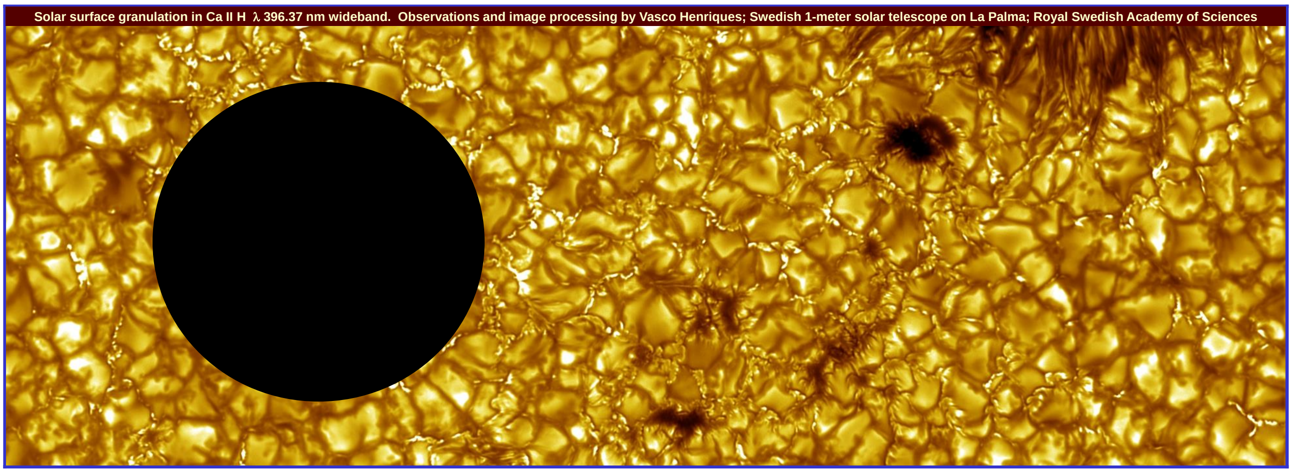

SPATIALLY RESOLVED SPECTROSCOPY ACROSS HD 189733 (K1 V) USING EXOPLANET TRANSITS

MARTIN GUSTAVSSON [1], DAINIS DRAVINS[1], HANS-GÜNTER LUDWIG [2]

[1] Lund Observatory, Box 43, SE-22100 LUND, Sweden
[2] Zentrum für Astronomie der Universität Heidelberg, Landessternwarte, Königstuhl 12, DE-69117 HEIDELBERG, Germany

Transiting exoplanets successively hide small segments of the stellar disk.

Differential spectroscopy between various transit phases provides spectra of those surface segments that were hidden behind the planet.

3-dimensional hydrodynamics can be studied in center-to-limb variations of line shapes, asymmetries and wavelength shifts.

Ongoing studies of the star HD189733 ('Alopex') aim at observing the center-to-limb variation of its photospheric line profiles.

How to verify 3-D model atmospheres?

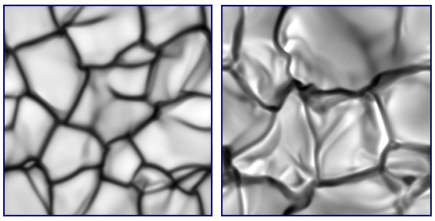

Simulations of 3-dimensional hydrodynamics: Granular structure on a 12,000 K white dwarf (left) and a 3,800 K red giant, computed with CO⁵BOLD. The areas differ greatly: 7×7 km^2 vs. 23×23 $R_\odot^2$. It has become possible to model widely different stars, but the observational means for verifying such simulations remain limited, except for the Sun.

3-D simulations predict line profiles across stellar disks

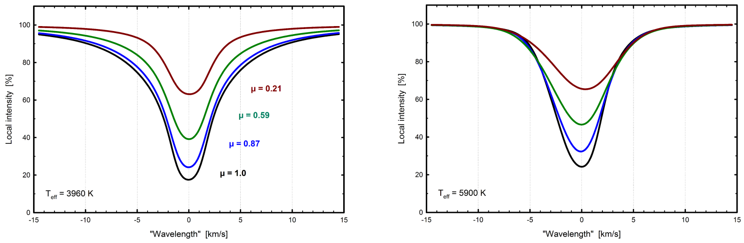

Synthetic line profiles are computed as spatial and temporal averages over the 3-D simulation. The changing line strengths, widths, asymmetries and convective wavelength shifts across the stellar disk reflect details of the atmospheric structure. These profiles from CO⁵BOLD models of main-sequence stars exemplify center-to-limb differences in line asymmetries. Synthetic profiles for one Fe I line at λ= 620 nm, χ = 3 eV, at the successive center-to-limb positions μ = cos θ = 1.0, 0.87, 0.59 and 0.21 were normalized to the local limb darkening. The star HD 189733 ('*Alopex*'*) currently under study has a temperature in between these models, T_{eff} ~ 4900 K.

Spatially resolved spectroscopy?

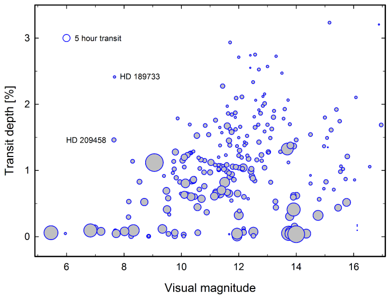

Spatially resolved stellar spectroscopy from exoplanet transits is observationally challenging since planets cover only ~ 1% of its host star. Thus, to achieve a signal-to-noise ratio of e.g. ~ 100 requires an original signal-to-noise of ~ 10,000. HD 189733b is selected since it exhibits the deepest transit among the brighter systems.

Example of observed Fe I line profiles in HD 189733 (Alopex, K1 V)*

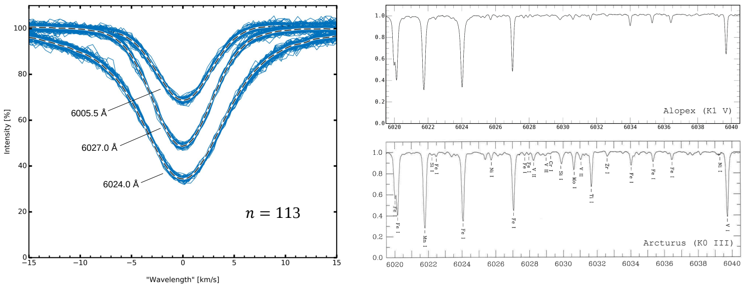

The signal-to-noise is increased by averaging many exposures of many similar line profiles. The left panel shows 113 exposures and their averages of three different Fe I lines in HD 189733 ('*Alopex*'*) formed using archive data from the ESO HARPS spectrometer. At upper right is an averaged spectrum of *Alopex* (K1 V, T_{eff} ~ 4900 K); lower right a reference spectrum of Arcturus (K0 III, T_{eff} ~ 4300 K; Hinkle et al., 2000). The similarity in spectral type of these two stars enables straightforward line identifications.

* *We refer to HD 189733 as 'Alopex' (from the Greek 'αλεπού'), denoting a fox related to the one that gave name to its constellation of Vulpecula.*